# Magma Storage and Extraction Associated with Plinian and Interplinian Activity at Santorini Caldera (Greece)

T. H. Druitt, M. Mercier, L. Florentin, E. Deloule, N. Cluzel, T. Flaherty, E. Médard, Anita Cadoux

# Magma Storage and Extraction Associated with Plinian and Interplinian Activity at Santorini Caldera (Greece)

**T. H. Druitt[1]*, M. Mercier[1], L. Florentin[2], E. Deloule[2], N. Cluzel[1], T. Flaherty[1], E. Médard[1] and A. Cadoux[3,4,5]**

[1]Laboratoire Magmas et Volcans, Université Blaise Pascal-CNRS-IRD, OPGC, 6 Avenue Blaise Pascal, 63178 AUBIERE Cedex; [2]CRPG–CNRS, BP 20, 54501 Vandoeuvre les Nancy, France; [3]Université d'Orléans, ISTO, UMR 7327, 45071 Orléans, France; [4]CNRS, ISTO, UMR 7327, 45071 Orléans, France and [5]BRGM, ISTO, UMR 7327, BP 36009, 45060 Orléans, France

*Corresponding author. Telephone: +33 4 7334 6718. E-mail: T.Druitt@opgc.univ-bpclermont.fr

Received July 3, 2015; Accepted March 7, 2016

## ABSTRACT

Santorini caldera has had a long history of plinian eruptions and caldera collapses, separated by 20–40 kyr interplinian periods. We have carried out a study to constrain magma storage/extraction depths beneath the caldera. We analysed $H_2O$ in 138 olivine-, pyroxene- and plagioclase-hosted melt inclusions from plinian and interplinian products from the last 200 kyr, and $CO_2$, S, Cl, F and $\delta D$ in various subsets of these. The dataset includes 64 inclusions in products of the Minoan plinian eruption of the late 17th century BCE. All the melt inclusions were ellipsoidal and isolated, with no textural evidence for volatile leakage. Mafic melt inclusions contain 1–4 wt % $H_2O$ and up to 1200 ppm $CO_2$, 1200 ppm S, 2000 ppm Cl and 400 ppm F; silicic inclusions contain 2–7 wt % $H_2O$, up to 150 ppm $CO_2$, up to 400 ppm S, 2000–6000 ppm Cl and 600–1000 ppm F. The $\delta D$ values of 27 representative inclusions (–37 to –104‰) are intermediate between mantle and slab values and rule out significant $H_2O$ loss by hydrogen diffusion from olivine-hosted inclusions. $H_2O$, S and Cl behave compatibly in melt inclusion suites varying from mafic to silicic in composition, showing that entrapment of many melt inclusions took place under volatile-saturated conditions. Most Santorini melts are saturated in a free COHSCl vapour phase at depths of less than $\sim$10 km; the only exceptions are basaltic melts from a single interplinian eruption, which were volatile-undersaturated up to $K_2O$ contents of $\sim$1 wt %. The rhyolitic melt of the Minoan eruption probably contained a free hypersaline liquid phase. $H_2O + CO_2$ saturation pressures were calculated using suitably calibrated solubility models to estimate pre-eruptive magma storage depths. Magmas feeding plinian eruptions were stored at $>$4 km ($>$100 MPa) and extracted over depth intervals of several kilometres. Plagioclase phenocrysts in rhyodacitic pumice from the Minoan eruption have cores containing melt inclusions trapped at depths up to 10–12 km (320 MPa), and rims (also orthopyroxene and clinopyroxene) containing inclusions trapped at 4–6 km (100–160 MPa). This records late-stage silicic replenishment of a $<$2 km thick shallow magma chamber, rather than extraction of melts syneruptively over the entire depth range. The plagioclase cores were carried from depth in the ascending melt, then overgrown by the rims in the shallow chamber. Exsolution of volatiles during ascent may have caused the replenishment melt to inject as a bubbly plume, causing mixing prior to eruption. This would explain (1) the homogeneity of the Minoan rhyodacitic magma, and (2) extraction of melt inclusions from the entire pressure spectrum during the first eruptive phase. Most silicic magmas feeding eruptions of the interplinian periods were stored in reservoirs at shallow depths (2–3 km) compared with those feeding the plinian eruptions ($>$4 km). Melt inclusions from the AD 726 eruption of Kameni Volcano yield a pre-eruptive storage depth of $\sim$4 km, which is similar to that estimated from geodetic data for the inflation source during the 2011–2012 period of caldera

unrest; this supports a magmatic origin of the unrest. The level of pre-AD 726 magma storage beneath Kameni was deeper than that of earlier silicic interplinian eruptions, perhaps owing to changes in crustal stress caused by the Minoan eruption. Combined with previously published results, the melt inclusion data provide a time-integrated image of the crustal plumbing system. Mantle-derived basalts are injected into the lower crust, where they fractionate to produce evolved melts in bodies of hot crystal mush. Evolved residual melts separate from their parent mushes in the 8 to >15 km depth interval, then ascend rapidly into the upper crust, where they either crystallize or accumulate as bodies of eruptible, crystal-poor magma.

**Key words**: magma storage; melt inclusions; plinian; Santorini; volatiles

## INTRODUCTION

The crustal magma plumbing system beneath a volcano exerts a strong control on eruptive behaviour and hazards (see reviews by Cashman & Sparks, 2013; Cashman & Giordano, 2014). Pre-eruptive storage conditions determine initial magma properties such as pressure, temperature, volatile content and volatile composition, which in turn influence eruption dynamics (Colucci *et al.*, 2014). Magma ascending from deep to shallow crustal levels can inject to form high-level lenses of eruptible magma, or replenish and remobilize extant bodies of crystal mush, resulting in rapid build-up to eruption (Annen *et al.*, 2006; Bachmann & Berganz, 2008; Druitt *et al.*, 2012; Menand *et al.*, 2015). Knowledge of past plumbing system architectures is useful for the interpretation of geodetic and seismic data during periods of unrest (e.g. Blundy *et al.*, 2008; Arienzo *et al.*, 2010; Muir *et al.*, 2014). Volatile contents of phenocryst-hosted melt inclusions (MIs) can be used to petrologically image the magma storage system if the degree of multi-species volatile saturation is known, and if accurate, appropriately calibrated, solubility laws exist (Wallace, 2005; Moore, 2008). Melt inclusions have been used to probe magma storage levels beneath silicic caldera volcanoes prior to individual eruptions, such as Bishop, Oruanui and Kos Plateau (Wallace *et al.*, 1995; Lui *et al.*, 2005; Bachmann *et al.*, 2009). Temporal variations of pre-eruptive magma storage depth with time within tight chrono-stratigraphic contexts have, however, been documented at only a few caldera volcanoes such as Toba (Chesner & Luhr, 2010) and Mount Mazama (Wright *et al.*, 2012).

Santorini is a multi-cyclic caldera complex with an eruptive history spanning half a million years (Druitt *et al.*, 1999). Activity over the last ~360 kyr has consisted of multiple caldera-forming plinian eruptions, alternating with interplinian periods characterized by effusive activity and weak (mostly subplinian or less) explosive eruptions. Detailed knowledge of the eruptive, structural and chemical history of the complex makes Santorini a good target for using MIs to understand the factors that control magma storage and extraction beneath calderas. We address the following questions. First, over what range of depths were magmas extracted immediately prior to, and during, each plinian eruption? Studies of ignimbrites such as Bishop and Oruanui (Wallace *et al.*, 1995; Liu *et al.*, 2005) have shown that magma can be extracted from a surprisingly large range of depths, raising questions concerning the geometry of large silicic magma reservoirs (Cashman & Giordano, 2014). Second, are there differences between the pre-plinian storage levels and those during interplinian periods? The 15 month period of caldera unrest at Santorini between January 2011 and March 2012 involved inflation of the caldera floor and greatly increased levels of microseismicity, and has been attributed to the shallow injection of 10–25 million $m^3$ of magma (Newman *et al.*, 2012; Parks *et al.*, 2012, 2015). Is this hypothesis consistent with magma storage levels prior to historical eruptions of the volcano?

We report the $H_2O$ contents of 138 phenocryst-hosted melt inclusions from Santorini, most of which were also analysed for $CO_2$, S, Cl and F. We also analysed a subset of inclusions for their D/H isotopic ratio to test for $H_2O$ loss from olivine-hosted MIs by hydrogen diffusion (Hauri, 2002; Bucholz *et al.*, 2013). By showing that MIs in nearly all Santorini magmas were trapped under volatile-saturated conditions, we invert the data via published solubility models to provide a time-integrated petrological snapshot of the crustal plumbing system over the last 200 kyr. Based on a set of 64 new volatile analyses of MIs from the Minoan plinian eruption of the late 17th century BCE, we place tight constraints on the thickness of the upper crustal magma reservoir that fed that eruption, as well as on the nature of an event of recharge by silicic melt that took place within about a decade prior to it.

## VOLCANOLOGICAL BACKGROUND AND PREVIOUS STUDIES

### Santorini volcanism

Santorini is the southernmost volcanic centre of the Aegean island arc (Fig. 1). It lies on continental crust about 25 km thick (Tirel *et al.*, 2004), which is partitioned into upper and lower sections, with the boundary lying at about 15 km depth (Sachpazi *et al.*, 1997; Konstaninou, 2010). The volcano is situated within a 40 km wide NE–SW rift zone of normal to right-lateral transtensional faults (Dimitriadis *et al.*, 2009; Nomikou *et al.*, 2012; Feuillet, 2013). The caldera is

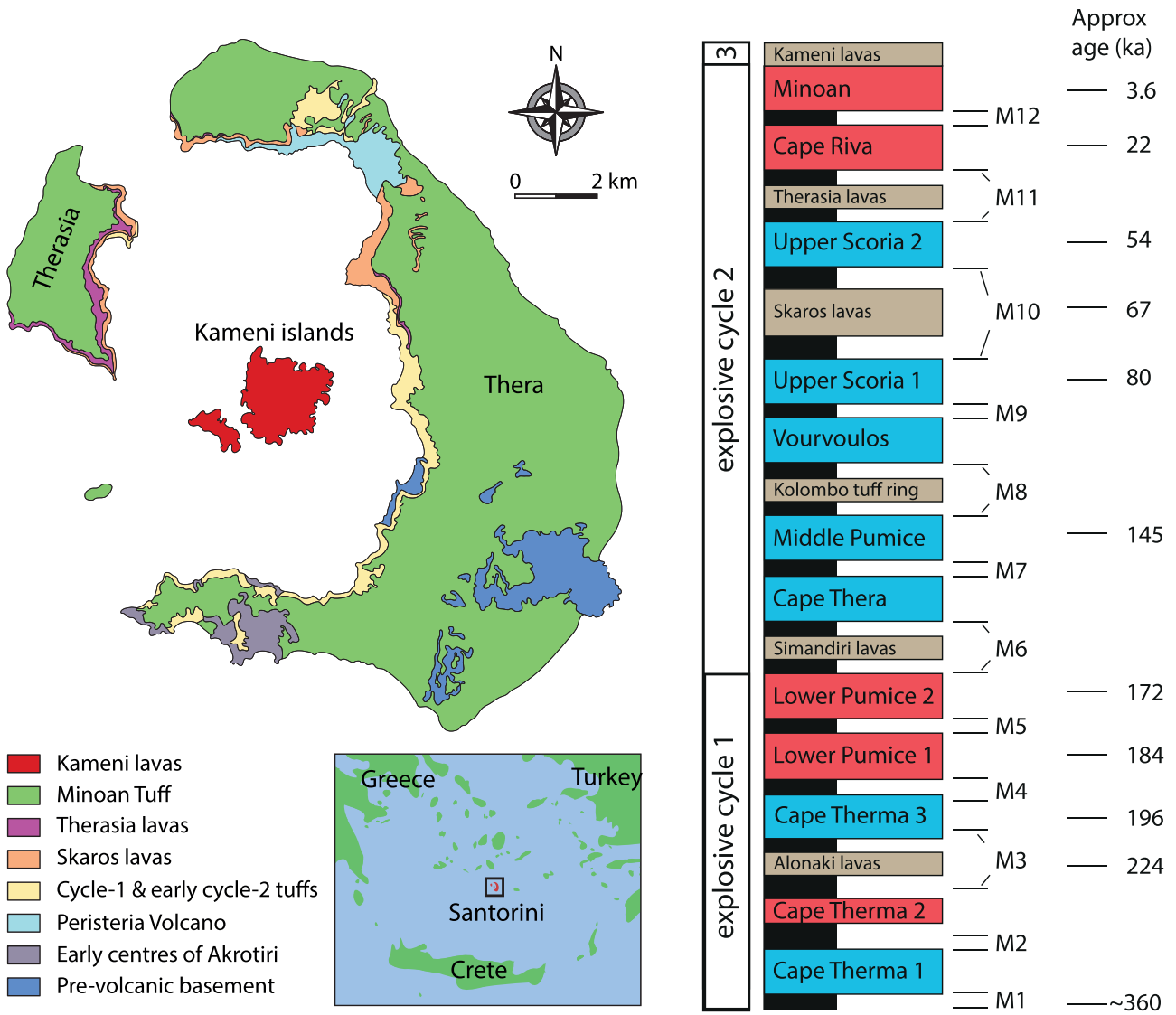


**Fig. 1.** Simplified geological map of Santorini, with inset showing the regional location. The schematic stratigraphic column shows the main eruptive units since the onset of major explosive volcanism, about 360 kyr ago. The activity since that time can be divided into three explosive cycles, cycles 1 and 2 each ending in a pair of major caldera-forming silicic eruptions, and cycle 3 inferred to have begun with the modern-day Kameni activity. Eruptions of mainly intermediate composition are shown as blue boxes, and those of mainly silicic composition are shown as red boxes. The silicic Cape Therma 3 unit is of much smaller magnitude than the other silicic units depicted. Black boxes are sequences of interplinian tephra (named M1 to M12, after Vespa *et al.*, 2006), and brown boxes are prominent lava or tuff successions within the interplinian sequences (after Druitt *et al.*, 1999). The ages derive from K–Ar and $^{40}Ar/^{39}Ar$ dating of onland products (Druitt *et al.*, 1999), as well as from O-isotope wiggle matching dating of deep-sea tephra [unpublished data cited by Vespa *et al.* (2006) and Gertisser *et al.* (2009)].

10 km north–south, 6 km west–east, and is an ~45 $km^2$ multiple collapse structure that last subsided during the Minoan eruption of the late 17th century BCE (Druitt, 2014). Repeated eruptions have subsequently built up a largely submarine 3 $km^3$ intracaldera edifice, the subaerial summits of which form the Kameni Islands (Pyle & Elliot, 2006).

The evolution of the volcanic field has been described by Druitt *et al.* (1999). It is founded on a pre-volcanic island of Mesozoic limestones and Tertiary metapelites, draped and plastered by the volcanic products. The earliest dated volcanism (650–550 ka) discharged amphibole-bearing silicic tuffs and lava flows. Between 530 and 430 ka, a stratocone complex (Peristeria Volcano) was constructed in the northern half of the volcanic field. Major explosive activity began at ~360 ka, and since then about 12 large-magnitude (1–100 $km^3$ range) plinian eruptions have occurred. The plinian eruptions all had fallout phases, most discharged ignimbrite, and most were probably accompanied by caldera collapse. Direct field evidence exists for large collapses following the Lower Pumice 2, Cape Riva and Minoan eruptions (Druitt & Francaviglia, 1992). Plinian eruptions were separated by interplinian periods during which

prolonged effusive (and weakly explosive) activity built up intracaldera edifices, which then collapsed during the next plinian eruption. This alternation of plinian and interplinian activity has been repeated on average every 20–40 kyr. Sequences of interplinian pyroclastic products record many small-magnitude eruptions in the subplinian to violent strombolian (or less) range (some may be small-magnitude plinian). The interplinian sequences are termed M1–M12 (Fig. 1), and they range from basaltic to rhyodacitic in composition. They have been described by Druitt *et al.* (1999) and Vespa *et al.* (2006); Vaggelli *et al.* (2009) described a scoria fall deposit from unit M12.

The volcanic products since 360 ka can be divided into two ~180 kyr magmatic cycles, each commencing with eruptions of mainly mafic to intermediate composition, and terminating with a pair of large silicic plinian eruptions: Lower Pumice 1 and Lower Pumice 2 at the end of cycle 1, and Cape Riva and Minoan at the end of cycle 2 (Fig. 1). The present-day Kameni interplinian activity (last eruption 1950) may constitute the start of a third volcanic cycle.

Santorini magmas range from basaltic (up to ~7 wt % MgO) to rhyodacitic in composition, and are transitional tholeiitic to calc-alkaline in character (Druitt *et al.*, 1999). Typical phase assemblages (in all but the oldest, >550 ka, products) are olivine ± augite ± plagioclase in basalts (<53 wt % $SiO_2$), plagioclase + augite + magnetite ± olivine ± orthopyroxene in andesites (53–63 wt % $SiO_2$), and plagioclase + augite + orthopyroxene + magnetite + ilmenite + apatite ± pyrrhotite ± (rare) hornblende in dacites (63–68 wt % $SiO_2$) and rhyodacites (68–72 wt % $SiO_2$). Interstitial glasses in some rhyodacites are rhyolitic (>72 wt % $SiO_2$). The primary melt at Santorini has been estimated by back-calculation to have 9–12 wt % MgO (Nichols, 1978). This would fractionate 6–13 wt % of olivine and small amounts of Cr-spinel and clinopyroxene to generate the most primitive basalt erupted (~7 wt % MgO). Incompatible trace element contents (e.g. K, Rb, Th, La) in the intermediate and silicic magmas decrease with time, probably as a result of changing proportions of different mantle-derived mafic magma batches entering the crust (Huijsmans *et al.*, 1988; Druitt *et al.*, 1999; Francalanci *et al.*, 2005; Bailey *et al.*, 2009; Vaggelli *et al.*, 2009; Fabbro *et al.*, 2013). However, if a single time slice is considered, then Santorini magmas can be modelled well by fractional crystallization accompanied by ~10% of crustal assimilation (Barton *et al.*, 1983; Mann, 1983; Barton & Huijsmans, 1986; Huijsmans *et al.*, 1988; Huijsmans & Barton, 1989; Druitt *et al.*, 1999; Zellmer *et al.*, 2000).

Understanding of Santorini magmatism has been advanced by a recent series of phase equilibria studies on a parental basalt (~340 ka Balos basalt; Andújar *et al.*, 2015), a silicic andesite Andújar *et al.* (in preparation), and silicic magmas of four plinian eruptions (Lower Pumice 1, Lower Pumice 2, Cape Riva and Minoan; Cadoux *et al.*, 2014). The experiments were carried out at 100–400 MPa, 850–1040°C, redox conditions of QFM (quartz–fayalite–magnetite) to NNO (nickel–nickel oxide) + 3·5, and melt $H_2O$ contents of 2–10 wt %. Some of the main conclusions were as follows: (1) parental basalt containing 4–6 wt % $H_2O$ fractionates via 60–80 wt % crystallization to silicic andesite at about 400 MPa, 1000°C and QFM; (2) silicic melts are generated by fractional crystallization at 200-400 MPa; (3) silicic melts feeding plinian eruptions are saturated with respect to $H_2O + Cl \pm CO_2$, and in some cases a hypersaline liquid (brine) phase.

Abundant nodules of cumulate gabbro and diorite have been erupted on Santorini. Cumulate gabbros contain primocrysts of plagioclase, clinopyroxene, orthopyroxene, Fe–Ti oxides and rare olivine with intercumulus quartz, alkali feldspar, hornblende and biotite. Major element modelling reproduces the observed phase assemblages and proportions of the gabbros if they are assumed to be cumulates from andesites with 56–66% $SiO_2$ (Druitt *et al.*, 1999).

Measurements of $H_2O$, S and halogens in Santorini MIs have been reported by several researchers (Sigurdsson *et al.*, 1990; Gardner *et al.*, 1996; Cottrell *et al.*, 1999; Michaud *et al.*, 2000; Gertisser *et al.*, 2009; Vaggelli *et al.*, 2009; Cadoux *et al.*, 2014). However, there are no published data for $H_2O$ in basaltic melts, no volatile data for interplinian products, and no measurements of $CO_2$ at all.

### Previous estimates of pre-eruptive magma storage pressures

Previous estimates of storage pressures of <550 ka Santorini magmas have been made using mineral equilibria, phase equilibria experimentation, and geodetic modelling of deformation during the 2011–2012 period of unrest; they range from <100 to ~400 MPa (Table 1). Phase equilibria studies of the natural products have constrained pre-eruptive storage pressures for silicic pumices from the four main plinian eruptions (≥200 MPa; Cadoux *et al.* 2014), for a basalt from the ~340 ka Balos cinder cone (~400 MPa; Andújar *et al.*, 2015), and for an andesite from a plinian eruption (~200 MPa; Andújar *et al.*, in preparation). Gertisser *et al.* (2009) estimated a pressure of 430 ± 10 MPa for the silicic Lower Pumice 2 magma body using the Al-in-hornblende barometer; however, the barometer as used is probably outside its conditions of application (Johnson & Rutherford, 1989; Anderson & Smith, 1995), and the amphibole in LP2 may be antecrystic (Cadoux *et al.*, 2014).

## METHODS

### Field sampling

Our samples were collected mostly from pyroclastic products of the second explosive cycle, but we also included the two rhyodacitic eruptions terminating cycle 1 (Lower Pumices 1 and 2), as well as one sample from the (cycle 3) Kameni edifice (Fig. 1). The samples (described in Table 2) are representative of plinian

**Table 1:** Previous estimates of pre-eruptive storage depths of Santorini magmas

| Unit | Composition | Pressure (MPa) | Depth (km) | Method | Ref. |
|---|---|---|---|---|---|
| Kameni | s | 80–150 | 3·1–5·8* | cpx–plag equilibria | 1 |
| Skaros, Peristeria | m, i | 170–340 | 6·6–13·1* | cpx–plag and ol–cpx equilibria | 2 |
| Lower Pumice 2 | s | 430 ± 10 | 16·6 ± 0·4* | Al in hb; equilibrium with qz | 4 |
| Minoan | s | ≥200 to 50 | >7·7 to ~1·9* | phase equilibria; melt inclusions | 3, 5 |
| Min, CR, LP2, LP1 | s | ≥200 | >7·7* | phase equilibria | 5 |
| Minoan | s | 190 ± 50 | 7·3 ± 1·9* | hb composition (mph-rich pumice) | 5 |
| Balos basalt | m | ~400 | ~15·4* | phase equilibria | 6 |
| Unrest 2011–2012 | ? | | 3·3–6·3 | geodesy | 7–9 |
| Silicic melt generation | s | 200–400 | 7·7–15·4* | phase equilibria Fe/Mg ratios | 10 |

References: 1, Barton & Huijsmans (1986); 2, Huijsmans & Barton (1989); 3, Cottrell *et al.* (1999); 4, Gertisser *et al.* (2009); 5, Cadoux *et al.* (2014); 6, Andújar *et al.* (2015); 7, Newman *et al.* (2012); 8, Parks *et al.* (2015); 9, Papoutsis *et al.* (2013); 10, Andújar *et al.* (in preparation). m, mafic; i, intermediate; s, silicic; mph, microphenocryst. Min, Minoan; CR, Cape Riva; LP2, Lower Pumice 2, LP1, Lower Pumice 1. ol, olivine; cpx, clinopyroxene; plag, plagioclase; hb, hornblende; qz, quartz
*Recalculated using a mean upper crustal density of 2640 kg $m^{-3}$ (Konstantinou, 2010).

**Table 2:** Sample details

| Unit | Eruptive phase | Sample | $SiO_2$ (wt %) | Phenocryst phases | Description |
|---|---|---|---|---|---|
| Kameni* | AD 726 | PKB3 | 67 | pl, px, ox | Dacitic pumice from AD 726 eruption |
| Minoan* | 4 | S12-10 | 70 | pl, px, ox | Rhyodacitic pumice; ignimbrite |
| | 4 | S82-11 | 70 | pl, px, ox | Rhyodacitic pumice; ignimbrite |
| | 4 | S82-2 | 70 | pl, px, ox | Rhyodacitic pumice; ignimbrite |
| | 3 | R2 | 70 | pl, px, ox | Rhyodacitic pumice; low-grade ignimbrite |
| | 2 | S82-34b | 70 | pl, px, ox | Rhyodacitic pumice; pyroclastic surge |
| | 1 | S82-30 | 70 | pl, px, ox | Rhyodacitic pumice; fallout |
| | 1 | S82-28 | 70 | pl, px, ox | Rhyodacitic pumice; fallout |
| | 1 | S82-34a | 61 | pl, px, ox, hb (tr) | Mph-rich andesitic pumice, fallout |
| M12† | | G1 | 54 | ol, pl, px, ox | Andesitic scoria; fallout |
| Cape Riva* | 1 | S09-39 | 67 | pl, px, ox | Dacitic pumice; fallout |
| M10a-FS3‡ | | S12-43 | 52 | ol, pl, px, ox | Basaltic scoria; fallout |
| M10a-BP‡ | | S12-41 | 58 | pl, px, ox | Andesitic scoria; fallout |
| M10a-Y/B6‡ | | S12-37 | 51 | ol, pl, px, ox | Basaltic scoria; 5 cm fallout |
| Vourvoulos* | 1 | S12-67 | 66 | pl, px, ox | Dacitic pumice; fallout |
| M8-MSF‡ | | S12-68 | 56 | ol, pl, px, ox | Andesitic scoria; fallout |
| Middle Pumice* | 1 | S12-59 | 65 | pl, px, ox, ol (tr) | Dacitic pumice; fallout |
| M7a§ | | S12-46 | 64 | pl, px, ox | White dacitic pumice; 25 cm fallout |
| M7c§ | | S12-44 | 53 | ol, pl, px, ox | Black basaltic scoria; 40 cm fallout |
| M6a§ | | S12-48 | 65 | pl, px, ox | White dacitic pumice; 20 cm fallout |
| M6e§ | | S12-52 | 54 | ol, pl, px, ox | Black andesitic scoria; 20 cm fallout |
| Lower Pumice 2* | 1 | S09-23 | 70 | pl, px, ox | Rhyodacitic pumice; fallout |
| Lower Pumice 1* | 1 | S09-17 | 69 | pl, px, ox | Rhyodacitic pumice; fallout |

*Unit name and $SiO_2$ content from Druitt *et al.* (1999).
†Unit name and $SiO_2$ content from Vaggelli *et al.* (2009); sampled at the location in that paper.
‡Unit name, eruptive phase, and $SiO_2$ content from Vespa *et al.* (2006); sampled at the photograph locations in that paper.
§Details of M6 and M7 given by Druitt *et al.* (1999).
ol, olivine; px, pyroxene; ox, oxides; hb, hornblende; tr, trace quantities; mph, microphenocryst.

(Lower Pumice 1, Lower Pumice 2, Middle Pumice, Vourvoulos, Cape Riva and Minoan) and interplinian (M6, M7, M8, M10, M12, Kameni) eruptions; Vourvoulos is the smallest of the plinian units. The mafic interplinian units were laid down by violent strombolian to subplinian eruptions.

The samples consist of one or more fresh, glassy pyroclasts ranging from basaltic to rhyodacitic in composition, as analysed by previous researchers (Druitt *et al.*, 1999; Vespa *et al.*, 2006; Vaggelli *et al.*, 2012). In the case of olivine-bearing samples, we chose fallout lapilli one to a few centimetres in diameter that would have cooled rapidly during emplacement, and hence would contain olivine-hosted MIs less likely to be affected by post-eruptive diffusive loss of $H_2O$ (Lloyd *et al.*, 2013).

## Sample preparation and selection

One or more clasts from each level were crushed and sieved, retaining the fractions between 0·5 and 1·0 mm and between 1·0 and 2·0 mm. Olivine, pyroxene and plagioclase crystals were handpicked under a binocular microscope, giving priority where possible to euhedral, glass-coated crystals. The MIs selected for study were vitreous (without daughter minerals or heavy oxide dusting), ellipsoidal, isolated (not connected to the crystal surface) and fracture-free (Fig. 2). Partially crystallized

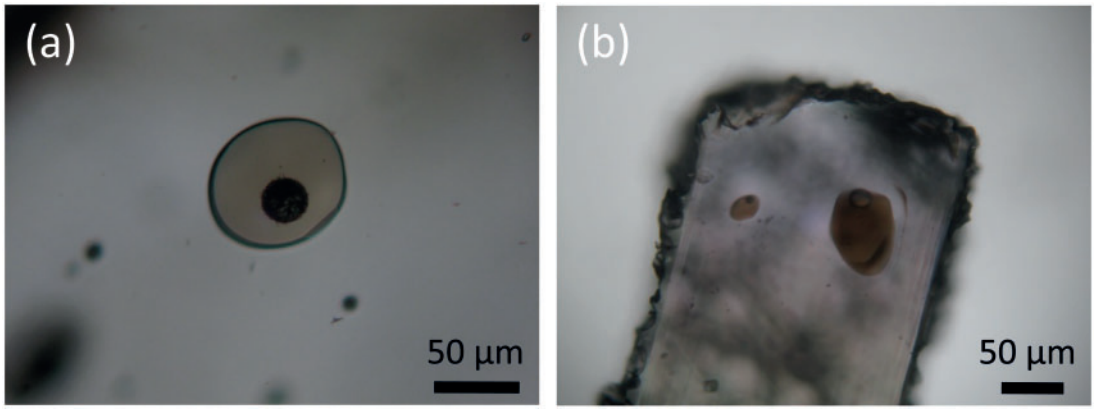


**Fig. 2.** Photomicrographs of representative melt inclusions hosted by (a) olivine (M8-MSF, S12-68, crystal 6, MI 1), and (b) plagioclase (Kameni AD 726, PKB3, crystal 4, MI 1).

MIs were observed, but not studied. Each crystal was mounted in resin, then polished on one face to expose the chosen MI. The crystal was then extracted, washed in acetone and pressed into indium and coated with gold for secondary ion mass spectrometry (SIMS) analysis. All polishing was done using corundum disks to avoid carbon contamination from diamond powder. Following SIMS analysis, the indium crystal mount was repolished and coated with carbon for major element, sulphur and halogen analysis by electron microprobe.

We also analysed the composition of the host mineral phase immediately in contact with each MI. In olivine or pyroxene, the crystal was spot analysed as close as possible to the MI. In plagioclase, we used back-scattered electron (BSE) imagery to recognize the plagioclase in equilibrium with the MI. Melt inclusions in plagioclase commonly occupy resorption re-entrants that were then sealed up by precipitation of further plagioclase. By analysing the plagioclase shell around the MI, we obtained a true equilibrium plagioclase–melt pair.

## Analytical techniques

Major element compositions of MIs were analyzed by wavelength-dispersive spectrometry (WDS) on a CAMECA SX 100 electron microprobe at the Laboratoire Magmas et Volcans, Clermont-Ferrand using a 15 keV, 4–8 nA electron beam with a 10–20 μm spot size and calibrated using international glass standard A99. These conditions avoided significant Na diffusion under the electron beam, as confirmed by test analyses on a single, large $H_2O$-rich MI. The host olivine, pyroxene or plagioclase was analysed using a 15 keV, 15 nA focused beam, and calibrated on natural and synthetic minerals.

Volatile contents of the MIs were analysed by SIMS using the IMS 1280 system at the French national SIMS facility (Centre de Recherches Pétrographiques et Géochimiques, Nancy) during five analytical sessions: (1) M12 and Minoan; (2) Lower Pumice 1, Lower Pumice 2, M6, M7, Middle Pumice, M8, Vourvoulos and Kameni; (3) M10a and Cape Riva; (4) δD and some Minoan MIs; (5) additional Minoan MIs. A 4–6 nA primary beam of $Cs^+$ ions was focused on a 10 μm diameter area, and the electron gun was used to avoid electrostatic charging. Negative secondary ions $^{12}C$, $^{17}O$, $^{16}O^1H$, $^{18}O$, $^{19}F$, $^{27}Al$, $^{30}Si$, $^{32}S$ and $^{35}Cl$ were measured at a mass resolution of 7850, with an energy offset of 30 ± 10 eV, by ion counting on EM in monocollection mode. A 10 μm × 10 μm raster was used for 80 s prior to analysis on each spot to pre-sputter through the gold coat and remove surface contamination. The sample chamber vacuum was kept below $2 \times 10^{-9}$ torr using a liquid nitrogen trap. Each analysis consisted of between 15 and 20 scans, with counting times of 4 s per scan on each peak.

Concentrations of $H_2O$ and $CO_2$ were calculated using best-fit regressions to plots of $H_2O/SiO_2$ vs $^{16}O^1H/^{30}Si$ and of $CO_2/SiO_2$ vs $^{12}C/^{30}Si$, respectively. We used three sets of experimental standard glasses to calibrate the $H_2O$ analyses (Fig. 3): (1) 13 basaltic glasses with 0–5·7 wt % $H_2O$; (2) four dacitic glasses with 0–6·4 wt % $H_2O$; (3) seven rhyolitic glasses with 0–6·6 wt % $H_2O$ (Appendix A). These define three distinct calibration curves with slopes increasing as a function of melt polymerization (Fig. 3a) (Hauri, 2002). Each calibration curve was fitted by a quadratic polynomial

$$\left(\frac{H_2O}{SiO_2}\right) = A\left(\frac{^{16}O^1H}{^{30}Si}\right) + B\left(\frac{^{16}O^1H}{^{30}Si}\right)^2$$

where $A$ and $B$ are functions of $SiO_2$ content. The $H_2O$ content of each MI was determined by calculating its value from the two calibration curves with $SiO_2$ contents (renormalized to 100 wt % dry) below and above that of the MI, then by linear interpolation between these two values as a function of $SiO_2$ content. Although the rhyolite calibration curve is not well constrained at $H_2O/SiO_2 < 0{\cdot}03$, our silicic MIs all lie at values above this.

We used three sets of standard glasses for $CO_2$: a basaltic set containing 0–3800 ppm $CO_2$, an andesitic set containing 2600–4300 ppm, and a rhyolitic set containing

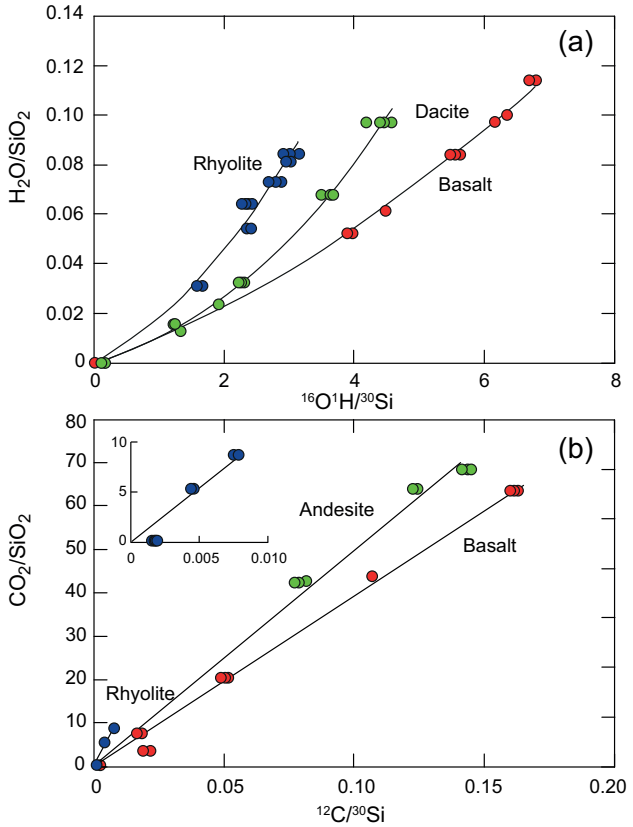


**Fig. 3.** Examples of SIMS standard calibration curves for (a) $H_2O$ and (b) $CO_2$. The standards are listed in Appendix A. Sample $H_2O$ and $CO_2$ values were determined by extrapolating between the standard curves, using renormalized silica contents, as described in the text.

15–680 ppm. The andesitic set was synthesized especially for this study in Clermont-Ferrand using a Santorini andesite (Appendix B). These glasses defined three calibration lines with slopes increasing as a function of melt polymerization (Fig. 3b). The best-fit calibration curves were linear,

$$\left(\frac{CO_2}{SiO_2}\right) = C\left(\frac{^{12}C}{^{30}Si}\right)$$

where the slope $C$ is a function of $SiO_2$ content. The matrix effect for $CO_2$ was then corrected by linear extrapolation between neighbouring curves, as for $H_2O$.

The $H_2O$ and $CO_2$ contents of all analysed MIs fall within the calibration range of the standards. Uncertainties (relative percentage on the mean) on $H_2O$ and $CO_2$ abundances owing to SIMS counting statistics are $<3\%$ and $<5\%$ (rarely up to 10%) respectively, and the detection limits are 0·01 wt % and 50 ppm, respectively (Supplementary Data Appendix 1; supplementary data are available for downloading at http://www.petrology.oxfordjournals.org). Uncertainties on the $H_2O$ and $CO_2$ calibration curves are about $\pm 5\%$.

For S, Cl and F, the SIMS data were calibrated using electron microprobe analyses of a subset of MIs ranging from basaltic to rhyolitic in composition (Fig. 4).

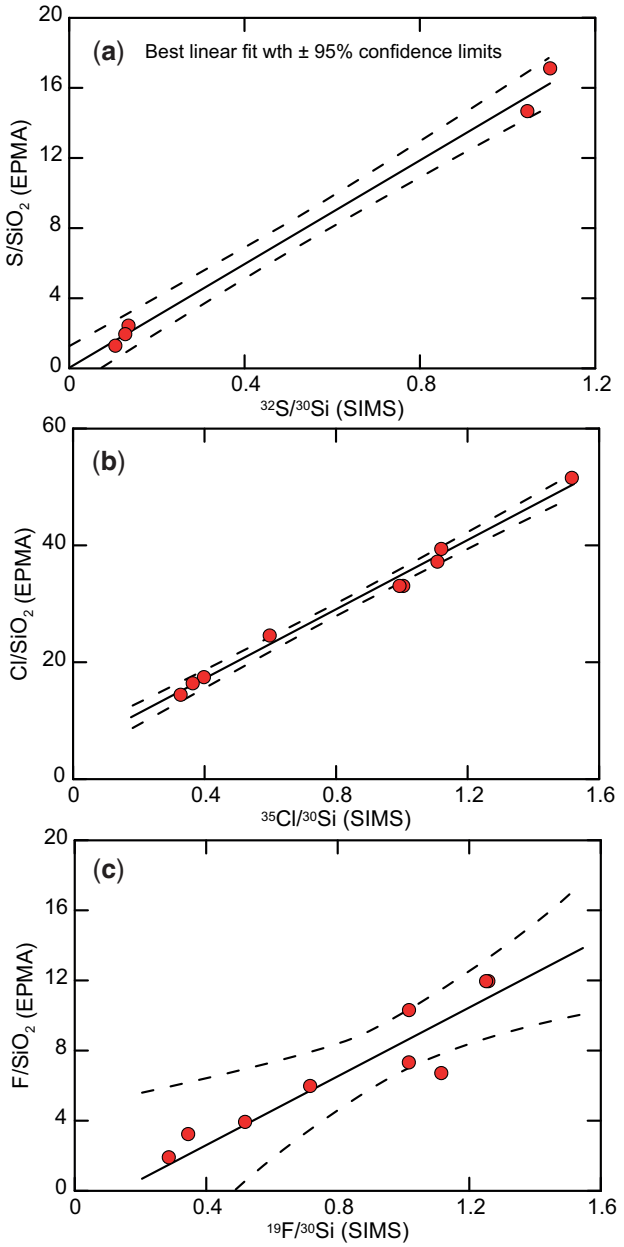


**Fig. 4.** Examples of calibration curves for SIMS analyses of S, Cl and F using electron microprobe analysis (EPMA) of the same melt inclusions. The continuous lines are linear best fits to the data, and the dashed lines are the 95% confidence limits on the fits.

A separate calibration was used for each SIMS sample batch. The electron microprobe analyses of S, Cl and F were carried out following the technique of Moune *et al.* (2007), with a 40 nA sample current, 10 μm beam diameter, and counting times of 200–400 s. To minimize volatile loss during analysis, the beam was blanked regularly with the Faraday cup and counts were collected at 20 s intervals by 10 iterations for Cl and S, and 20 iterations for F. As S speciation can be significantly affected by oxidation state (Moretti & Ottonello, 2005; Métrich *et al.*, 2008), the S peak position was checked

before each analysis to improve measurement accuracy. The electron microprobe analyses were calibrated on three international standards: Vg2 (S, 1400 ppm), Alvin (S, 993 ppm) and KE12 (Cl, 3300 ppm; F, 4500 ppm). Uncertainties (relative percentage on the mean) on S, Cl and F abundances owing to SIMS counting statistics are <5%, and most are 1–2% (Supplementary Data Appendix 1). Uncertainties on calibration curves for S, Cl and F are about ±5%, ±8% and ±12%, respectively.

The D/H ratios of 27 representative MIs were analyzed in sample batch 4 by SIMS using the IMS 1280 system with the same primary beam as for $H_2O$ and $CO_2$. Negative secondary ions H and D were measured at a mass resolution of 1500, without energy offset and a 30 eV energy slit, in monocollection mode by ion counting for D and on FC for H. A 10 μm × 10 μm raster was used for 80 s to pre-sputter through the gold coat. Each analysis consisted of between 15 and 20 scans, with counting times per scan of 4 s and 30 s for H and D respectively. The D/H ratio calibrations were done using two sets of standard glasses of basaltic and andesitic composition (Metrich & Deloule, 2014). No systematic matrix effect was observed as a function of either $SiO_2$ or $H_2O$ content, so the same correction was applied to all of the measured compositions, with a calibration error of <8%.

Shrinkage bubbles in six representative MIs in doubly polished crystal wafers were analysed using a Renishaw InVia Raman spectrometer at the Laboratoire Magmas et Volcans, Clermont-Ferrand, to determine whether $CO_2$ was present at levels above the detection limit. If $CO_2$ partly partitioned into bubbles during cooling, then the amount present must be 'added back' into the MIs for estimation of the original melt value (e.g. Neave *et al.*, 2014). The spectrometer was equipped with a Peltier cooled charge-coupled device (CCD) detector and a microscope in confocal setting. The samples were excited by a 532 nm wavelength laser source. The source output power was 1 W for all analyses, and the power on the samples was 30 mW. The counting time was 30 s (three cycles of 10 s). A grating of 2400 grooves per mm was used.

## RESULTS

The results are summarized in Table 3, and are given in full in Supplementary Data Appendix 1.

### Melt inclusion textures

The 138 glassy MIs selected for study have maximum diameters of 30–270 μm and minimum diameters of 20–170 μm (Fig. 2); 93 are hosted by plagioclase, 32 by olivine, and 13 by pyroxene. A sixth of the MIs contain no shrinkage bubble; most of the others contain a single bubble of diameter 1–55 μm, but some contain multiple bubbles nucleated on the inclusion margins. The majority of bubbles account for <5 vol. % of the MIs, with a few up to 12 vol. %, as typical of shrinkage bubbles. Only two MIs from plinian units have bubble fractions in excess of that expected from shrinkage (Middle Pumice, 16 vol. %; Minoan, 28 vol. %; Supplementary Data Appendix 1); however, these could in part be artefacts of underestimation of MI volume.

### Major elements of melt inclusions and minerals

The olivine crystals containing MIs are weakly zoned, and range in composition from $Fo_{73}$ to $Fo_{86}$; the weak zoning implies relatively simple MI entrapment histories in the olivines. A range of olivine composition is observed in each olivine-bearing sample, except in M12, where the Fo content is uniformly high ($Fo_{85–86}$). All compositions of olivine-hosted MIs were corrected for post-entrapment crystallization using a melt–olivine equilibrium constant $K_D = (FeO/MgO)_{ol}/(FeO/MgO)_{melt}$ of 0·31 (Toplis, 2005); the extent of post-entrapment crystallization is less than 10% in all cases. Clinopyroxene and orthopyroxene hosts have compositions of $Wo_{43–46}$ $En_{37–39}$ $Fs_{16–19}$ and $Wo_3$ $En_{55–57}$ $Fs_{39–42}$, respectively. Plagioclase hosts have compositions from $An_{37}$ to $An_{94}$; most are zoned, apart from those from the Vourvoulos eruption ($An_{47–49}$). Because $K_D$ values in the pyroxene–melt and plagioclase–melt systems are not well constrained, we did not correct the compositions of MIs trapped in pyroxenes and plagioclase.

Major element compositions of the MIs are plotted in Fig. 5. The melts range from basaltic to rhyolitic, with a gap at intermediate compositions ($SiO_2$ from 57 to 63 wt %). The gap is a sampling artefact of our dataset, not a real feature of Santorini melts. For example, MIs in mafic components of Lower Pumice 2 [analysed by Gertisser *et al.* (2009), but not us] have compositions lying within the gap. Overall, our analysed MIs from 46 to 57 wt % $SiO_2$ are hosted by olivine ($Fo_{73–86}$), cpx or calcic plagioclase ($An_{79–95}$), and those from 63 to 75 wt % $SiO_2$ are hosted by plagioclase ($An_{33–60}$), cpx or opx.

The MIs from each of the mafic interplinian units (M6e, M7c, M8-MSF, M10-FS3, M10-Y/B6, M12) exhibit significant ranges of composition; in M6e and M10-FS3 the plagioclase-hosted MIs are slightly more evolved than those hosted by olivines in the same sample, but in M7c and M8-MSF, there is no difference. The silicic MIs are, on the other hand, compositionally more uniform in terms of major elements. Taken together, the MIs define a trend in which MgO, FeO, CaO and $TiO_2$ decrease, and $K_2O$ and $Na_2O$ increase, with increasing $SiO_2$ (Table 3). This is similar to the trends of Santorini whole-rock data (Fig. 5), which have been successfully modelled by fractional crystallization with minor crustal assimilation (Mann, 1983; Huijsmans & Barton, 1989; Druitt *et al.*, 1999). Vectors of fractional crystallization, based on phase equilibria experiments performed on Santorini basalt at 400 MPa pressure (Andújar *et al.*, 2015), reproduce the MI trends (Fig. 5). Superimposition of MI and whole-rock data in Fig. 5 shows that the MI compositions are representative of typical Santorini magmas.

**Table 3:** Melt inclusion analyses and calculated parameters

| Sample | Crystal | MI | Host crystal (wt %) | | | Melt inclusion (recalculated dry) (wt %) | | | | | | | | | MI volatiles and H isotopes | | | | | | Pressure (MPa)* | | | Temperature (°C)† | | |
|---|---|---|---|---|---|---|---|---|---|---|---|---|---|---|---|---|---|---|---|---|---|---|---|---|---|---|
| | | | Phase | Mg# | An | $SiO_2$ | $TiO_2$ | $Al_2O_3$ | FeO | MnO | MgO | CaO | $Na_2O$ | $K_2O$ | $H_2O$ (wt %) | $CO_2$ (ppm) | S (ppm) | Cl (ppm) | F (ppm) | δD (‰) | VolCalc | Papale | SolEx | Ol–melt Putirka | Pl–melt Putirka | Pl–melt Lange |
| *Kameni, AD 726* | | | | | | | | | | | | | | | | | | | | | | | | | | |
| PKB3 | 1 | 1 | plag | | 50 | 70·6 | 0·42 | 15·29 | 3·63 | 0·11 | 0·72 | 2·47 | 4·37 | 2·36 | 4·69 | 139 | | 3243 | 697 | | | 148 | | | 903 | 895 |
| PKB3 | 2 | 1 | plag | | 52 | 69·2 | 0·96 | 15·13 | 4·05 | 0·13 | 0·79 | 2·62 | 4·85 | 2·30 | 5·20 | 41 | | 3467 | 709 | | | 159 | | | 900 | 873 |
| PKB3 | 3 | 1 | plag | | 49 | 69·8 | 0·55 | 15·23 | 3·50 | 0·17 | 0·80 | 2·74 | 4·84 | 2·38 | 4·18 | 72 | | 3031 | 615 | | | 113 | | | 922 | 920 |
| PKB3 | 4 | 1 | plag | | 49 | 70·1 | 0·43 | 15·19 | 3·59 | 0·13 | 0·71 | 2·55 | 4·90 | 2·39 | 4·06 | | | 3263 | 635 | | | | | | | |
| PKB3 | 5 | 1 | plag | | 51 | 70·0 | 0·56 | 14·81 | 3·58 | 0·15 | 0·75 | 2·58 | 5·25 | 2·35 | 4·23 | 75 | | 3031 | 718 | –88 | | 113 | | | 919 | 928 |
| *Minoan, Phase 1* | | | | | | | | | | | | | | | | | | | | | | | | | | |
| S82-28 | 1-0 | a | cpx | 69 | | 73·0 | 0·35 | 15·15 | 1·97 | 0·00 | 0·12 | 1·10 | 4·10 | 4·26 | 4·26 | 130 | 59 | 4019 | 764 | | 139 | 138 | | | | |
| S82-28 | 1-3 | a | cpx | 69 | | 72·6 | 0·39 | 15·00 | 2·28 | 0·00 | 0·16 | 1·44 | 4·89 | 3·29 | 4·50 | 118 | 86 | 3688 | 807 | | 149 | 142 | | | | |
| S82-28 | 1-18 | a | cpx | 71 | | 73·5 | 0·35 | 14·76 | 1·97 | 0·00 | 0·18 | 1·20 | 4·69 | 3·35 | 4·35 | 114 | 79 | 3956 | 794 | | 141 | 134 | | | | |
| S82-28 | 1-18 | b | cpx | 70 | | 74·6 | 0·29 | 14·37 | 1·31 | 0·00 | 0·09 | 1·01 | 4·37 | 3·98 | 4·31 | 139 | 75 | 3830 | 746 | | 143 | 141 | | | | |
| S82-30 | 5-54 | a | cpx | 69 | | 73·8 | 0·36 | 14·73 | 1·55 | 0·00 | 0·17 | 1·28 | 4·72 | 3·38 | 4·23 | 69 | 62 | 3921 | 733 | | 128 | 124 | | | | |
| S82-30 | 5-54 | b | cpx | 70 | | 73·5 | 0·39 | 14·84 | 1·48 | 0·00 | 0·13 | 1·51 | 4·84 | 3·28 | 4·18 | 107 | 73 | 3806 | 746 | | 132 | 129 | | | | |
| S82-30 | 2-20 | a | cpx | 67 | | 74·8 | 0·36 | 14·25 | 1·30 | 0·00 | 0·11 | 1·13 | 4·61 | 3·48 | 4·73 | 100‡ | | | | | 157 | 156 | | | | |
| S82-30 | 4-20 | a | cpx | 68 | | 73·0 | 0·30 | 14·72 | 2·20 | 0·00 | 0·24 | 1·37 | 4·72 | 3·50 | 4·52 | 152 | 74 | 3641 | 802 | | 155 | 149 | | | | |
| S82-30 | 5-43 | a | cpx | 66 | | 74·0 | 0·32 | 14·35 | 2·06 | 0·00 | 0·20 | 1·23 | 4·52 | 3·34 | 4·39 | 135 | 69 | 3986 | 743 | | 146 | 138 | | | | |
| S82-30 | 1-30 | a | opx | 59 | | 73·0 | 0·32 | 14·50 | 2·52 | 0·00 | 0·15 | 1·27 | 4·79 | 3·43 | 4·38 | 122 | 82 | 3820 | 760 | | 143 | 132 | | | | |
| S82-30 | 1-39 | a | opx | 57 | | 74·0 | 0·31 | 14·21 | 2·35 | 0·00 | 0·08 | 1·48 | 4·52 | 3·08 | 4·13 | 98 | 64 | 3568 | 725 | | 128 | 115 | | | | |
| S82-30 | 3-3 | a | opx | 58 | | 74·3 | 0·32 | 13·67 | 2·41 | 0·00 | 0·12 | 1·27 | 4·53 | 3·37 | 4·38 | 99 | 84 | 3962 | 771 | | 140 | 126 | | | | |
| S82-30 | 3-46 | a | opx | 59 | | 73·1 | 0·32 | 14·18 | 2·79 | 0·00 | 0·25 | 1·35 | 4·53 | 3·51 | 4·14 | 106 | 78 | 3545 | 764 | | 130 | 116 | | | | |
| S82-30 | 1-16 | b | plag | | 42 | 73·1 | 0·41 | 14·58 | 2·32 | 0·00 | 0·30 | 1·43 | 4·17 | 3·64 | 5·02 | 126 | 100 | 4573 | 765 | | 173 | 176 | | | 844 | 894 |
| S82-30 | 1-38 | a | plag | | 44 | 73·2 | 0·38 | 14·19 | 2·44 | 0·00 | 0·36 | 1·51 | 4·44 | 3·44 | 4·61 | 136 | 94 | 3653 | 771 | | 157 | 149 | | | 857 | 919 |
| S82-30 | 1-41 | a | plag | | 40 | 74·6 | 0·30 | 13·82 | 2·05 | 0·00 | 0·30 | 1·28 | 4·23 | 3·44 | 4·69 | 152 | 78 | 3429 | 743 | | 160 | 158 | | | 838 | 910 |
| S82-30 | 1-49 | a | plag | | 42 | 74·3 | 0·32 | 13·76 | 1·86 | 0·00 | 0·20 | 1·41 | 4·66 | 3·52 | 4·71 | 132 | 79 | 3604 | 736 | | 159 | 154 | | | 844 | 915 |
| S82-30 | 1-64 | a | plag | | 42 | 73·8 | 0·30 | 14·31 | 1·88 | 0·00 | 0·28 | 1·34 | 4·50 | 3·56 | 4·38 | 149 | 90 | 3164 | 708 | | 147 | 143 | | | 853 | 938 |
| S82-30 | 2-8 | a | plag | | 37 | 73·7 | 0·30 | 13·93 | 2·26 | 0·00 | 0·36 | 1·24 | 4·40 | 3·81 | 4·45 | 198 | 83 | 3535 | 722 | | 156 | 153 | | | 839 | 920 |
| S82-30 | 2-10 | a | plag | | 41 | 73·5 | 0·35 | 14·16 | 2·33 | 0·00 | 0·31 | 1·39 | 4·23 | 3·77 | 4·33 | 130 | 58 | 4320 | 823 | | 142 | 135 | | | 854 | 931 |
| S82-30 | 4-2 | a | plag | | 42 | 74·3 | 0·32 | 13·97 | 1·81 | 0·00 | 0·33 | 1·31 | 4·49 | 3·43 | 4·56 | 151 | 64 | 3059 | 684 | | 155 | 152 | | | 846 | 926 |
| S82-30 | 4-2 | b | plag | | 38 | 74·4 | 0·25 | 14·06 | 1·73 | 0·00 | 0·28 | 1·27 | 4·62 | 3·39 | 4·67 | 98 | 56 | 3322 | 714 | | 151 | 148 | | | 838 | 913 |
| S82-30 | 4-13 | a | plag | | 41 | 73·7 | 0·27 | 14·23 | 1·88 | 0·00 | 0·29 | 1·46 | 4·66 | 3·50 | 4·68 | 116 | 43 | 3514 | 710 | | 156 | 152 | | | 850 | 913 |
| S82-30 | 4-22 | a | plag | | 34 | 75·4 | 0·22 | 13·43 | 1·70 | 0·00 | 0·23 | 1·31 | 4·25 | 3·45 | 4·68 | 84 | 85 | 3747 | 752 | | 147 | 145 | | | 827 | 889 |
| S82-30 | 3-9 | a | plag | | 41 | 73·7 | 0·28 | 14·04 | 1·92 | 0·00 | 0·32 | 1·50 | 4·87 | 3·37 | 4·25 | 109 | 77 | 3252 | 666 | | 136 | 126 | | | 861 | 936 |
| S82-30 | 1 | 1 | plag | | 49 | 73·6 | 0·37 | 14·28 | 2·14 | 0·07 | 0·32 | 1·49 | 4·39 | 3·32 | 6·85 | 80 | 86 | 3879 | 826 | | 253 | 324 | | | 812 | 819 |
| S82-30 | 2 | 1 | plag | | 43 | 73·8 | 0·30 | 14·13 | 2·08 | 0·16 | 0·29 | 1·45 | 4·27 | 3·54 | 5·17 | 73 | 58 | 3604 | 799 | | 171 | 174 | | | 838 | 886 |
| S82-30 | 2a | 1 | plag | | | 74§ | | | | | | | | | 4·33 | 100‡ | | | | –52 | 147 | 142 | | | | |
| S82-30 | 3a | 1 | plag | | | 74§ | | | | | | | | | 4·53 | 100‡ | | | | –49 | 156 | 152 | | | | |
| S82-30 | 5a | 1 | plag | | | 74§ | | | | | | | | | 4·34 | 100‡ | | | | –51 | 147 | 141 | | | | |
| S82-30 | 6a | 1 | plag | | | 74§ | | | | | | | | | 4·45 | 100‡ | | | | –37 | 152 | 147 | | | | |
| S82-30 | 7a | 1 | plag | | | 74§ | | | | | | | | | 4·34 | 100‡ | | | | –49 | 148 | 143 | | | | |
| S82-30 | 8a | 1 | plag | | | 74§ | | | | | | | | | 6·71 | 100‡ | | | | –38 | 238 | 273 | | | | |
| S82-30 | 9a | 1 | plag | | | 74§ | | | | | | | | | 6·16 | 100‡ | | | | –41 | 219 | 242 | | | | |
| S8234a¶ | 2 | 1 | plag | | 45 | 72·5 | 0·86 | 14·12 | 2·85 | 0·08 | 0·43 | 1·68 | 3·97 | 3·55 | 5·38 | 26 | 129 | 4773 | 806 | | 176 | 181 | | | 845 | 865 |
| S8234a¶ | 4 | 1 | plag | | 37 | 75·1 | 0·25 | 13·60 | 1·87 | 0·07 | 0·27 | 1·26 | 4·02 | 3·57 | 6·55 | 56 | 48 | 3479 | 756 | | 231 | 303 | | | 790 | 808 |
| *Minoan, Phase 2* | | | | | | | | | | | | | | | | | | | | | | | | | | |
| S82-34b | 1 | 1 | plag | | 46 | 73·5 | 0·32 | 14·19 | 2·05 | 0·11 | 0·29 | 1·46 | 4·58 | 3·50 | 6·06 | 21 | 61 | 3519 | 787 | | 206 | 236 | | | 824 | 853 |
| S82-34b | 3 | 1 | plag | | 42 | 73·9 | 0·29 | 14·08 | 1·94 | 0·02 | 0·28 | 1·41 | 4·60 | 3·48 | 4·33 | 24 | 56 | 3332 | 753 | | 125 | 115 | | | 855 | 935 |

(continued)

**Table 3:** (Continued)

| Sample | Crystal | MI | Host crystal (wt %) | | | Melt inclusion (recalculated dry) (wt %) | | | | | | | | | MI volatiles and H isotopes | | | | | | Pressure (MPa)* | | | Temperature (°C)† | | |
|---|---|---|---|---|---|---|---|---|---|---|---|---|---|---|---|---|---|---|---|---|---|---|---|---|---|---|
| | | | Phase | Mg# | An | $SiO_2$ | $TiO_2$ | $Al_2O_3$ | FeO | MnO | MgO | CaO | $Na_2O$ | $K_2O$ | $H_2O$ (wt %) | $CO_2$ (ppm) | S (ppm) | Cl (ppm) | F (ppm) | δD (‰) | VolCalc | Papale | SolEx | Ol–melt Putirka | Pl–melt Putirka | Pl–melt Lange |
| S82-34b | 4 | 1 | plag | | 42 | 74·4 | 0·32 | 13·92 | 1·97 | 0·01 | 0·27 | 1·30 | 4·43 | 3·38 | 4·52 | 19 | 43 | 3002 | 752 | | 132 | 124 | | | 846 | 929 |
| S82-34b | 6 | 1 | plag | | 43 | 73·9 | 0·31 | 14·16 | 2·04 | 0·08 | 0·30 | 1·38 | 4·37 | 3·49 | 4·67 | 30 | 59 | 3467 | 789 | | 141 | 136 | | | 848 | 917 |
| *Minoan, Phase 3* | | | | | | | | | | | | | | | | | | | | | | | | | | |
| R2 | 1 | 2 | plag | | 43 | 73·4 | 0·28 | 14·25 | 2·25 | 0·02 | 0·33 | 1·47 | 4·57 | 3·42 | 4·22 | 17 | 41 | 3495 | 702 | | 120 | 108 | | | 864 | 945 |
| R2 | 3 | 1 | plag | | 42 | 73·7 | 0·34 | 14·30 | 2·08 | 0·10 | 0·31 | 1·39 | 4·36 | 3·44 | 4·17 | 28 | 60 | 3575 | 759 | | 119 | 109 | | | 860 | 945 |
| *Minoan, Phase 4* | | | | | | | | | | | | | | | | | | | | | | | | | | |
| S82-2 | 1-1 | a | plag | | 42 | 73·4 | 0·35 | 14·48 | 2·23 | 0·00 | 0·35 | 1·45 | 4·37 | 3·35 | 4·82 | 100‡ | 70 | 3803 | 708 | | 160 | 157 | | | 850 | 905 |
| S82-2 | 1-49 | a | plag | | 39 | 73·8 | 0·27 | 13·90 | 2·24 | 0·00 | 0·27 | 1·33 | 4·80 | 3·42 | 4·41 | 129 | 56 | 3329 | 694 | | 145 | 135 | | | 848 | 929 |
| S82-2 | 1-49 | b | plag | | 33 | 74·6 | 0·27 | 13·88 | 1·82 | 0·00 | 0·25 | 1·36 | 4·33 | 3·46 | 4·49 | 100‡ | 47 | 3304 | 696 | | 142 | 138 | | | 837 | 899 |
| S82-2 | 1-75 | a | plag | | 42 | 74·4 | 0·25 | 14·00 | 1·97 | 0·00 | 0·29 | 1·29 | 4·45 | 3·35 | 4·46 | 113 | 64 | 3286 | 682 | | 145 | 137 | | | 848 | 933 |
| S82-2 | 1-75 | b | plag | | 42 | 74·7 | 0·30 | 13·92 | 1·81 | 0·00 | 0·26 | 1·40 | 4·14 | 3·46 | 4·38 | 64 | 64 | 3392 | 697 | | 133 | 127 | | | 850 | 925 |
| S82-2 | 1-66 | a | plag | | 43 | 73·7 | 0·32 | 13·98 | 2·24 | 0·00 | 0·36 | 1·46 | 4·43 | 3·49 | 5·81 | 127 | 64 | 3635 | 707 | | 209 | 230 | | | 824 | 854 |
| S82-2 | 1-24 | a | plag | | 42 | 73·6 | 0·37 | 13·99 | 2·34 | 0·00 | 0·35 | 1·41 | 4·38 | 3·58 | 4·46 | 96 | 65 | 3671 | 728 | | 143 | 134 | | | 852 | 924 |
| S82-11 | 2-63 | a | plag | | 42 | 73·6 | 0·36 | 14·01 | 2·11 | 0·00 | 0·30 | 1·40 | 4·83 | 3·36 | 4·18 | 118 | 71 | 3478 | 600 | | 134 | 123 | | | 861 | 949 |
| S82-11 | 3-10 | a | plag | | 42 | 73·4 | 0·29 | 14·63 | 1·98 | 0·00 | 0·28 | 1·47 | 4·50 | 3·49 | 4·33 | 140 | 70 | 3515 | 661 | | 145 | 139 | | | 862 | 937 |
| S82-11 | 3-10 | b | plag | | 40 | 73·5 | 0·33 | 14·36 | 1·82 | 0·00 | 0·35 | 1·53 | 4·69 | 3·45 | 4·77 | 87 | 67 | 3331 | 643 | | 156 | 154 | | | 850 | 902 |
| S82-11 | 3-16 | a | plag | | 41 | 73·6 | 0·33 | 14·21 | 2·20 | 0·00 | 0·24 | 1·36 | 4·59 | 3·52 | 4·12 | 147 | 65 | 3220 | 632 | | 136 | 127 | | | 859 | 950 |
| S82-11 | 3-16 | b | plag | | 42 | 73·3 | 0·30 | 14·53 | 2·23 | 0·00 | 0·35 | 1·40 | 4·32 | 3·51 | 4·21 | 65 | 65 | 3211 | 626 | | 127 | 118 | | | 862 | 942 |
| S82-11 | 3-19 | a | plag | | 38 | 74·1 | 0·35 | 14·31 | 1·86 | 0·00 | 0·25 | 1·32 | 4·25 | 3·54 | 4·09 | 123 | 67 | 3099 | 612 | | 130 | 124 | | | 854 | 942 |
| S82-11 | 3-50 | a | plag | | 42 | 73·7 | 0·29 | 14·04 | 1·82 | 0·00 | 0·27 | 1·43 | 4·90 | 3·51 | 4·40 | 163 | 72 | 3280 | 668 | | 151 | 144 | | | 856 | 936 |
| S82-11 | 3-61 | a | plag | | 41 | 73·5 | 0·37 | 14·05 | 1·89 | 0·00 | 0·35 | 1·52 | 4·85 | 3·48 | 4·15 | 152 | 90 | 3266 | 636 | | 139 | 131 | | | 864 | 942 |
| S82-11 | 1-23 | a | plag | | 39 | 74·0 | 0·30 | 13·89 | 2·16 | 0·00 | 0·29 | 1·30 | 4·70 | 3·41 | 4·14 | 161 | 71 | 3043 | 634 | | 138 | 129 | | | 853 | 942 |
| S82-11 | 2-34 | a | plag | | 40 | 73·9 | 0·31 | 13·90 | 2·02 | 0·00 | 0·29 | 1·41 | 4·57 | 3·57 | 4·03 | 156 | 77 | 3180 | 600 | | 133 | 124 | | | 858 | 945 |
| S82-11 | 2-34 | b | plag | | 38 | 74·7 | 0·30 | 14·01 | 1·79 | 0·00 | 0·26 | 1·40 | 4·10 | 3·43 | 4·74 | 135 | 72 | 3528 | 732 | | 160 | 161 | | | 839 | 894 |
| S82-11 | 3-7 | a | plag | | 39 | 74·5 | 0·26 | 13·66 | 1·88 | 0·00 | 0·27 | 1·23 | 4·70 | 3·46 | 4·57 | 126 | 72 | 3232 | 713 | | 150 | 144 | | | 837 | 921 |
| S82-11 | 2-30 | a | plag | | 41 | 73·4 | 0·36 | 14·31 | 2·00 | 0·00 | 0·30 | 1·48 | 4·68 | 3·43 | 4·84 | 164 | 99 | 3906 | 610 | | 171 | 170 | | | 849 | 903 |
| S82-11 | 3-57 | a | plag | | 42 | 73·6 | 0·31 | 14·12 | 2·25 | 0·00 | 0·30 | 1·43 | 4·41 | 3·57 | 4·75 | 165 | 87 | 3597 | 740 | | 167 | 162 | | | 847 | 909 |
| S12-10 | 2 | 1 | plag | | 40 | 74·6 | 0·23 | 14·00 | 1·80 | 0·03 | 0·24 | 1·32 | 4·40 | 3·38 | 4·90 | 100 | 45 | 3039 | 752 | | 162 | 162 | | | 835 | 900 |
| *M 12* | | | | | | | | | | | | | | | | | | | | | | | | | | |
| Vaggeli | 2 | 1 | oliv | 85 | | 57·3 | 0·88 | 18·27 | 5·61 | 0·15 | 4·71 | 8·31 | 3·40 | 1·32 | 3·30 | 253 | 656 | 770 | 303 | | | 101 | | 1065 | | |
| Vaggeli | 3 | 1 | oliv | 85 | | 50·7 | 0·68 | 19·81 | 7·28 | 0·13 | 6·16 | 12·76 | 2·19 | 0·26 | 3·10 | 193 | 1273 | 573 | 159 | | | 71 | 135 | 1087 | | |
| Vaggeli | 4 | 1 | oliv | 85 | | 51·6 | 0·83 | 19·61 | 6·91 | 0·03 | 5·80 | 12·16 | 2·46 | 0·61 | 3·20 | 190 | 1138 | 586 | 105 | | | 75 | 140 | 1080 | | |
| Vaggeli | 6 | 1 | oliv | 86 | | 53·8 | 0·67 | 18·80 | 6·56 | 0·13 | 5·82 | 10·98 | 2·23 | 0·98 | 3·30 | 232 | 1157 | 496 | 116 | | | 89 | | 1082 | | |
| *Cape Riva, Phase 1* | | | | | | | | | | | | | | | | | | | | | | | | | | |
| S09-39 | 1 | 1 | plag | | 40 | 71·2 | 0·50 | 14·90 | 3·11 | 0·07 | 0·41 | 1·66 | 5·04 | 3·00 | 4·70 | 145 | 76 | 2466 | 747 | −101 | | 151 | | | 867 | 909 |
| S09-39 | 2 | 1 | plag | | | | | | | | | | | | 3·35 | 222 | 103 | 3303 | 961 | | | 106 | | | | |
| S09-39 | 3 | 1 | plag | | | | | | | | | | | | 5·15 | 130 | 105 | 3078 | 912 | | | 173 | | | | |
| S09-39 | 3 | 2 | plag | | | | | | | | | | | | 3·32 | 155 | 91 | 3295 | 958 | | | 99 | | | | |
| S09-39 | 4 | 1 | plag | | | 70·7 | 0·46 | 14·97 | 3·37 | 0·00 | 0·43 | 1·88 | 5·15 | 2·99 | 3·62 | 131 | 82 | 3166 | 935 | | | 99 | | | | |
| S09-39 | 5 | 1 | plag | | 52 | 68·1 | 0·86 | 14·39 | 4·79 | 0·29 | 1·17 | 2·83 | 4·68 | 2·66 | 3·69 | | 385 | 2646 | 1075 | −79 | | | | | 940 | 951 |
| *M10a-6Y/B* | | | | | | | | | | | | | | | | | | | | | | | | | | |
| S12-37 | 1 | 1 | oliv | 82 | | 52·0 | 0·99 | 17·81 | 8·76 | 0·45 | 6·03 | 10·61 | 2·70 | 0·54 | 2·66 | 800 | 733 | 668 | 155 | | | 104 | 230 | 1103 | | |
| S12-37 | 1 | 2 | oliv | 83 | | 52·7 | 1·04 | 17·56 | 8·60 | 0·20 | 6·30 | 9·92 | 2·90 | 0·64 | 3·10 | 645 | 1075 | 711 | 175 | | | 117 | 230 | 1108 | | |
| S12-37 | 1 | 3 | oliv | 82 | | 50·8 | 0·91 | 18·63 | 8·67 | 0·14 | 6·63 | 10·99 | 2·76 | 0·43 | 2·71 | 483 | 736 | 735 | 151 | −54 | | 76 | 175 | 1120 | | |
| S12-37 | 2 | 1 | oliv | 77 | | 52·8 | 0·98 | 17·79 | 9·79 | 0·15 | 5·40 | 9·39 | 3·00 | 0·63 | 2·46 | 950 | 99 | 149 | 41 | | | 119 | 255 | 1103 | | |
| S12-37 | 5 | 1 | oliv | 78 | | 54·5 | 1·35 | 16·53 | 9·41 | 0·12 | 5·08 | 8·43 | 3·54 | 0·88 | 2·91 | 480 | 556 | 957 | 222 | −45 | | 105 | | 1098 | | |

(continued)

**Table 3:** (Continued)

| Sample | Crystal | MI | Host crystal (wt %) | | | Melt inclusion (recalculated dry) (wt %) | | | | | | | | | MI volatiles and H isotopes | | | | | | Pressure (MPa)* | | | Temperature (°C)† | | |
|---|---|---|---|---|---|---|---|---|---|---|---|---|---|---|---|---|---|---|---|---|---|---|---|---|---|---|
| | | | Phase | Mg# | An | $SiO_2$ | $TiO_2$ | $Al_2O_3$ | FeO | MnO | MgO | CaO | $Na_2O$ | $K_2O$ | $H_2O$ (wt %) | $CO_2$ (ppm) | S (ppm) | Cl (ppm) | F (ppm) | δD (‰) | VolCalc | Papale | SolEx | Ol–melt Putirka | Pl–melt Putirka | Pl–melt Lange |
| S12-37 | 5 | 2 | oliv | 78 | | 51·9 | 0·99 | 16·95 | 10·73 | 0·21 | 5·82 | 9·77 | 2·94 | 0·57 | 2·49 | 80 | 379 | 903 | 202 | | | 41 | 80 | 1113 | | |
| S12-37 | 6 | 1 | oliv | 78 | | 53·6 | 1·23 | 16·11 | 10·52 | 0·22 | 5·47 | 8·71 | 3·26 | 0·73 | 2·71 | 123 | 426 | 922 | 251 | –51 | | 53 | | 1105 | | |
| S12-37 | 8 | 1 | oliv | 78 | | 54·0 | 1·18 | 16·17 | 9·80 | 0·18 | 5·22 | 9·48 | 2·97 | 0·78 | 2·57 | 1190 | 481 | 870 | 277 | | | 184 | | 1095 | | |
| M10a-FS3 | | | | | | | | | | | | | | | | | | | | | | | | | | |
| S12-43 | 1 | 1 | oliv | 78 | | 52·9 | 1·26 | 17·17 | 9·37 | 0·23 | 5·41 | 9·70 | 3·48 | 0·42 | 1·60 | 32 | 467 | 938 | 283 | –90 | | 23 | 33 | 1114 | | |
| S12-43 | 2 | 1 | oliv | 73 | | 55·7 | 1·36 | 16·05 | 9·73 | 0·17 | 3·94 | 7·87 | 4·06 | 1·02 | 3·28 | 161 | 863 | 1546 | 344 | –84 | | 78 | | 1056 | | |
| S12-43 | 3 | 1 | oliv | 79 | | 53·0 | 1·10 | 16·79 | 9·88 | 0·25 | 5·48 | 9·68 | 3·29 | 0·44 | 1·17 | 199 | 483 | 677 | 222 | | | 20 | 60 | 1125 | | |
| S12-43 | 4 | 1 | oliv | 79 | | 53·3 | 1·08 | 17·58 | 9·02 | 0·13 | 5·11 | 9·79 | 3·45 | 0·43 | 1·75 | 37 | 452 | 945 | 262 | –109 | | 26 | | 1101 | | |
| S12-43 | 5 | 1 | oliv | 73 | | 55·9 | 1·29 | 16·35 | 9·59 | 0·16 | 4·10 | 7·89 | 3·55 | 0·99 | 3·23 | 157 | 853 | 1527 | 345 | | | 74 | | 1060 | | |
| S12-43 | 6 | 1 | oliv | 77 | | 50·7 | 1·00 | 17·35 | 11·14 | 0·34 | 5·48 | 10·35 | 2·94 | 0·59 | 1·65 | 512 | 785 | 746 | 277 | –72 | | 45 | 135 | 1118 | | |
| S12-43 | 7 | 1 | oliv | 82 | | 48·2 | 0·82 | 18·75 | 10·33 | 0·28 | 6·80 | 11·89 | 2·53 | 0·29 | 1·48 | 801 | | 712 | 158 | –71 | | 42 | 190 | 1146 | | |
| S12-43 | 11 | 1 | plag | | 78 | 57·8 | 1·32 | 16·75 | 8·57 | 0·00 | 2·86 | 7·09 | 4·12 | 1·36 | 3·21 | 267 | 793 | 1570 | 307 | –62 | | 91 | | | 1064 | 1060 |
| S12-43 | 12 | 1 | plag | | 83 | 57·2 | 1·11 | 17·11 | 8·75 | 0·26 | 3·06 | 7·33 | 3·92 | 1·18 | 3·24 | 291 | 727 | 1562 | 322 | –38 | | 91 | | | 1071 | 1090 |
| S12-43 | 13 | 1 | plag | | 91 | 54·4 | 1·03 | 16·74 | 9·94 | 0·12 | 5·27 | 8·23 | 3·52 | 0·67 | 2·50 | 152 | 894 | 1910 | 431 | –61 | | 51 | | | 1103 | 1189 |
| M10a-BP | | | | | | | | | | | | | | | | | | | | | | | | | | |
| S12-41 | 3 | 1 | plag | | 53 | 64·5 | 0·78 | 16·18 | 6·02 | 0·08 | 0·98 | 3·8 | 5·02 | 2·27 | 2·71 | 79 | 247 | 3309 | 780 | | | 54 | | | 1005 | 1028 |
| Vourvoulos | | | | | | | | | | | | | | | | | | | | | | | | | | |
| S12-67 | 1 | 1 | plag | | 47 | 68·5 | 0·62 | 14·22 | 5·43 | 0·20 | 0·63 | 2·73 | 4·84 | 2·79 | 3·56 | 95 | 130 | 3595 | 594 | | | 82 | | | 931 | 956 |
| S12-67 | 2 | 1 | plag | | 48 | 69·3 | 0·51 | 14·81 | 5·16 | 0·16 | 0·61 | 2·65 | 4·07 | 2·78 | 3·59 | 69 | 117 | 3670 | 605 | | | 81 | | | 932 | 942 |
| S12-67 | 3 | 1 | plag | | 47 | 68·6 | 0·42 | 14·93 | 4·83 | 0·17 | 0·56 | 2·98 | 4·83 | 2·72 | 3·30 | 79 | 111 | 3383 | 578 | | | 73 | | | 947 | 961 |
| S12-67 | 5 | 1 | plag | | 47 | 69·0 | 0·64 | 14·57 | 4·85 | 0·19 | 0·51 | 2·44 | 4·98 | 2·84 | 3·47 | 50 | 106 | 3442 | 598 | | | 73 | | | 929 | 968 |
| S12-67 | 6 | 1 | plag | | 46 | 69·0 | 0·50 | 14·61 | 4·74 | 0·17 | 0·54 | 2·68 | 4·85 | 2·88 | 3·43 | 59 | 112 | 3501 | 576 | | | 74 | | | 933 | 956 |
| S12-67 | 7 | 1 | plag | | 47 | 69·4 | 0·59 | 14·45 | 4·92 | 0·16 | 0·53 | 2·43 | 4·70 | 2·82 | 3·31 | 71 | 110 | 3416 | 611 | | | 71 | | | 931 | 970 |
| S12-67 | 7 | 2 | plag | | 47 | 69·0 | 0·51 | 14·47 | 4·95 | 0·17 | 0·55 | 2·53 | 4·95 | 2·88 | 3·06 | 143 | 106 | 3352 | 594 | | | 76 | | | 941 | 993 |
| M8, Main Scoria Fall | | | | | | | | | | | | | | | | | | | | | | | | | | |
| S12-68 | 4 | 1 | plag | | 94 | 52·3 | 0·85 | 16·65 | 9·30 | 0·19 | 6·72 | 11·29 | 2·40 | 0·27 | 2·59 | 113 | 570 | 629 | 234 | | | 50 | 95 | | 1120 | 1167 |
| S12-68 | 5 | 1 | oliv | 74 | | 53·9 | 1·18 | 14·99 | 12·12 | 0·24 | 5·40 | 8·45 | 2·85 | 0·82 | 2·75 | 185 | 446 | 805 | 216 | | | 60 | | 1112 | | |
| S12-68 | 6 | 1 | oliv | 82 | | 50·0 | 0·75 | 18·01 | 9·59 | 0·12 | 6·87 | 11·92 | 2·47 | 0·24 | 2·78 | 63 | 783 | 618 | 113 | | | 49 | 90 | 1125 | | |
| S12-68 | 7 | 1 | oliv | 75 | | 53·2 | 1·32 | 15·83 | 11·45 | 0·25 | 5·74 | 8·49 | 3·20 | 0·52 | 2·78 | 71 | 733 | 859 | 294 | | | 49 | | 1120 | | |
| S12-68 | 8 | 1 | oliv | 77 | | 52·2 | 1·45 | 16·01 | 11·39 | 0·20 | 5·98 | 8·69 | 3·42 | 0·63 | 2·84 | 102 | 925 | 923 | 192 | | | 54 | 105 | 1123 | | |
| Middle Pumice, Phase 1 | | | | | | | | | | | | | | | | | | | | | | | | | | |
| S12-59 | 1 | 1 | oliv | 76 | | 52·9 | 1·31 | 18·04 | 8·86 | 0·11 | 4·41 | 10·57 | 3·13 | 0·72 | 4·25 | | 1017 | 958 | 210 | | | 108 | 200 | 1039 | | |
| S12-59 | 3 | 1 | oliv | 81 | | 51·3 | 0·94 | 18·31 | 8·46 | 0·09 | 5·92 | 12·12 | 2·60 | 0·28 | 3·95 | 150 | 1017 | 718 | 128 | –80 | | 98 | 180 | 1077 | | |
| S12-59 | 4 | 1 | plag | | 46 | 68·8 | 0·56 | 15·57 | 3·90 | 0·19 | 0·66 | 2·68 | 4·56 | 3·09 | 5·01 | 78 | 108 | 2647 | 654 | | | 155 | | | 897 | 875 |
| M7a | | | | | | | | | | | | | | | | | | | | | | | | | | |
| S12-46 | 1 | 1 | plag | | 47 | 67·6 | 0·61 | 15·65 | 4·52 | 0·07 | 0·59 | 2·93 | 4·93 | 3·07 | 2·31 | 197 | 120 | 2630 | 595 | –88 | | 65 | | | 978 | 1039 |
| S12-46 | 2 | 1 | plag | | 50 | 66·6 | 0·74 | 15·80 | 4·71 | 0·11 | 0·73 | 3·45 | 5·00 | 2·90 | 3·49 | 160 | 135 | 2503 | 559 | | | 97 | | | 961 | 960 |
| S12-46 | 4 | 1 | plag | | 50 | 66·9 | 0·85 | 15·39 | 4·82 | 0·10 | 0·72 | 3·41 | 4·93 | 2·86 | 2·32 | 172 | 135 | 2601 | 580 | | | 61 | | | 991 | 1036 |
| M7c | | | | | | | | | | | | | | | | | | | | | | | | | | |
| S12-44 | 1 | 1 | plag | | | 50·2 | 0·83 | 20·01 | 8·14 | 0·16 | 4·30 | 13·87 | 2·34 | 0·17 | 2·51 | 181 | 856 | 650 | 105 | –82 | | | | | | |
| S12-44 | 2 | 1 | plag | | 92 | 54·0 | 0·90 | 14·85 | 8·78 | 0·19 | 7·12 | 11·11 | 2·56 | 0·50 | 1·80 | 115 | 839 | 636 | 329 | | | 32 | | | 1133 | 1185 |
| S12-44 | 3 | 1 | oliv | 85 | | 49·9 | 0·77 | 17·57 | 8·73 | 0·16 | 7·72 | 12·37 | 2·33 | 0·45 | 1·87 | 227 | 827 | 661 | 122 | | | 35 | 85 | 1157 | | |
| S12-44 | 5 | 1 | oliv | 84 | | 50·1 | 0·82 | 18·58 | 8·59 | 0·16 | 7·01 | 11·69 | 2·69 | 0·35 | 1·81 | 355 | 831 | 644 | 125 | –63 | | 37 | 115 | 1143 | | |
| S12-44 | 6 | 1 | oliv | 86 | | 49·0 | 0·71 | 19·49 | 7·59 | 0·16 | 7·41 | 12·94 | 2·52 | 0·21 | 1·94 | 196 | 765 | 662 | 116 | | | 34 | 80 | 1142 | | |
| S12-44 | 7 | 1 | oliv | 81 | | 56·2 | 1·25 | 15·84 | 8·38 | 0·11 | 5·45 | 8·08 | 3·35 | 1·29 | 2·12 | 211 | 283 | 834 | 266 | –79 | | 53 | | 1117 | | |

(continued)

**Table 3:** (Continued)

| Sample | Crystal | MI | Host crystal (wt %) | | | Melt inclusion (recalculated dry) (wt %) | | | | | | | | | MI volatiles and H isotopes | | | | | | Pressure (MPa)* | | | Temperature (°C)† | | |
|---|---|---|---|---|---|---|---|---|---|---|---|---|---|---|---|---|---|---|---|---|---|---|---|---|---|---|
| | | | Phase | Mg# | An | $SiO_2$ | $TiO_2$ | $Al_2O_3$ | FeO | MnO | MgO | CaO | $Na_2O$ | $K_2O$ | $H_2O$ (wt %) | $CO_2$ (ppm) | S (ppm) | Cl (ppm) | F (ppm) | δD (‰) | VolCalc | Papale | SolEx | Ol–melt Putirka | Pl–melt Putirka | Pl–melt Lange |
| M6a | | | | | | | | | | | | | | | | | | | | | | | | | | |
| S12-48 | 1 | 1 | plag | | 53 | 68·0 | 0·92 | 15·31 | 3·89 | 0·10 | 0·99 | 2·83 | 4·84 | 3·13 | 3·02 | | | 2479 | 729 | | | | | | 960 | 1006 |
| S12-48 | 2 | 1 | plag | | 54 | 68·8 | 0·78 | 14·92 | 4·07 | 0·11 | 0·96 | 2·66 | 4·05 | 3·61 | | 133 | | 2404 | 739 | | | | | | | |
| S12-48 | 3 | 1 | plag | | 51 | 69·0 | 0·69 | 15·12 | 3·55 | 0·15 | 0·87 | 2·51 | 4·79 | 3·35 | 3·06 | 153 | | 2451 | 713 | | | 84 | | | 945 | 1004 |
| S12-48 | 4 | 1 | plag | | 54 | 68·5 | 0·89 | 14·98 | 4·21 | 0·11 | 1·06 | 2·77 | 4·39 | 3·12 | 3·24 | 122 | | 2546 | 745 | | | 85 | | | 951 | 985 |
| S12-48 | 5 | 1 | plag | | 51 | 69·0 | 0·67 | 14·87 | 3·84 | 0·13 | 0·92 | 2·52 | 4·78 | 3·29 | 3·18 | 165 | | 2446 | 731 | | | 91 | | | 940 | 988 |
| S12-48 | 7 | 1 | plag | | 52 | 69·3 | 0·67 | 15·04 | 3·76 | 0·07 | 0·97 | 2·40 | 4·52 | 3·3 | 3·20 | | | 2743 | 761 | | | | | | 939 | 992 |
| S12-48 | 9 | 1 | plag | | 50 | 69·5 | 0·80 | 14·91 | 3·44 | 0·14 | 0·82 | 2·49 | 4·57 | 3·33 | 3·01 | 133 | | 2315 | 680 | | | 81 | | | 941 | 995 |
| M6e | | | | | | | | | | | | | | | | | | | | | | | | | | |
| S12-52 | 3 | 1 | oliv | 83 | | 51·6 | 0·95 | 17·03 | 8·77 | 0·12 | 6·51 | 11·76 | 2·72 | 0·52 | 2·64 | 34 | 838 | 737 | 151 | | | 47 | 80 | 1118 | | |
| S12-52 | 4 | 1 | oliv | 84 | | 51·5 | 0·93 | 16·49 | 8·96 | 0·12 | 7·39 | 11·50 | 2·61 | 0·52 | 3·02 | 162 | 841 | 769 | 151 | | | 68 | 125 | 1134 | | |
| S12-52 | 5 | 1 | oliv | 79 | | 55·2 | 1·10 | 16·37 | 8·71 | 0·22 | 5·31 | 8·63 | 3·54 | 0·95 | 2·94 | 51 | 876 | 1161 | 243 | | | 58 | | 1100 | | |
| S12-52 | 7 | 1 | plag | | 90 | 53·4 | 1·11 | 15·65 | 9·18 | 0·26 | 7·00 | 10·03 | 2·67 | 0·68 | 2·64 | 55 | 824 | 791 | 427 | | | 49 | | | 1101 | 1096 |
| Lower Pumice 2, Phase 1 | | | | | | | | | | | | | | | | | | | | | | | | | | |
| S09-23 | 1 | 1 | plag | | 39 | 68·7 | 0·50 | 15·49 | 4·07 | 0·17 | 0·76 | 1·97 | 5·22 | 3·14 | 5·17 | 70 | 77 | 4683 | 917 | −104 | | 157 | | | 871 | 876 |
| S09-23 | 2 | 1 | plag | | 37 | 71·4 | 0·38 | 14·99 | 2·76 | 0·05 | 0·37 | 1·60 | 5·15 | 3·33 | 4·71 | 225 | 62 | 3557 | 798 | | | 164 | | | 863 | 906 |
| S09-23 | 3 | 1 | plag | | 49 | 67·1 | 0·70 | 15·51 | 5·32 | 0·09 | 0·72 | 2·33 | 4·91 | 3·31 | 5·20 | 51 | 72 | 6024 | 967 | | | 172 | | | 891 | 887 |
| Lower Pumice 1, Phase 1 | | | | | | | | | | | | | | | | | | | | | | | | | | |
| S09-17 | 1 | 1 | plag | | 43 | 70·9 | 0·68 | 14·82 | 3·12 | 0·16 | 0·50 | 1·76 | 4·58 | 3·51 | 3·79 | 223 | 76 | 2812 | 793 | | | 126 | | | 892 | 961 |
| S09-17 | 2 | 1 | plag | | 41 | 70·9 | 0·38 | 14·54 | 3·01 | 0·07 | 0·40 | 1·62 | 5·19 | 3·89 | 5·57 | 91 | 62 | 2847 | 854 | | | 193 | | | 841 | 869 |

*Barometers VolatileCalc (Newman & Lowenstern, 2002), Papale (Papale *et al.*, 2006) and SolEx (Witham *et al.*, 2012). The Papale algorithm is at http://ctserver.ofm-research.org/Papale/Papale.php.
†Thermometers of Putirka [2008; equations (22) and (24 a)] and Lange *et al.* (2009).
‡$CO_2$ concentration assumed in pressure estimation.
§The samples containing these melt inclusions were lost by a commercial transport company following SIMS analysis and before the inclusions and their host plagioclase could be analysed by electron probe. The $H_2O$ analyses were corrected using this assumed $SiO_2$ content.
¶Microphenocryst-rich andesitic pumice, which is a minor component in the Minoan products (Druitt, 2014).

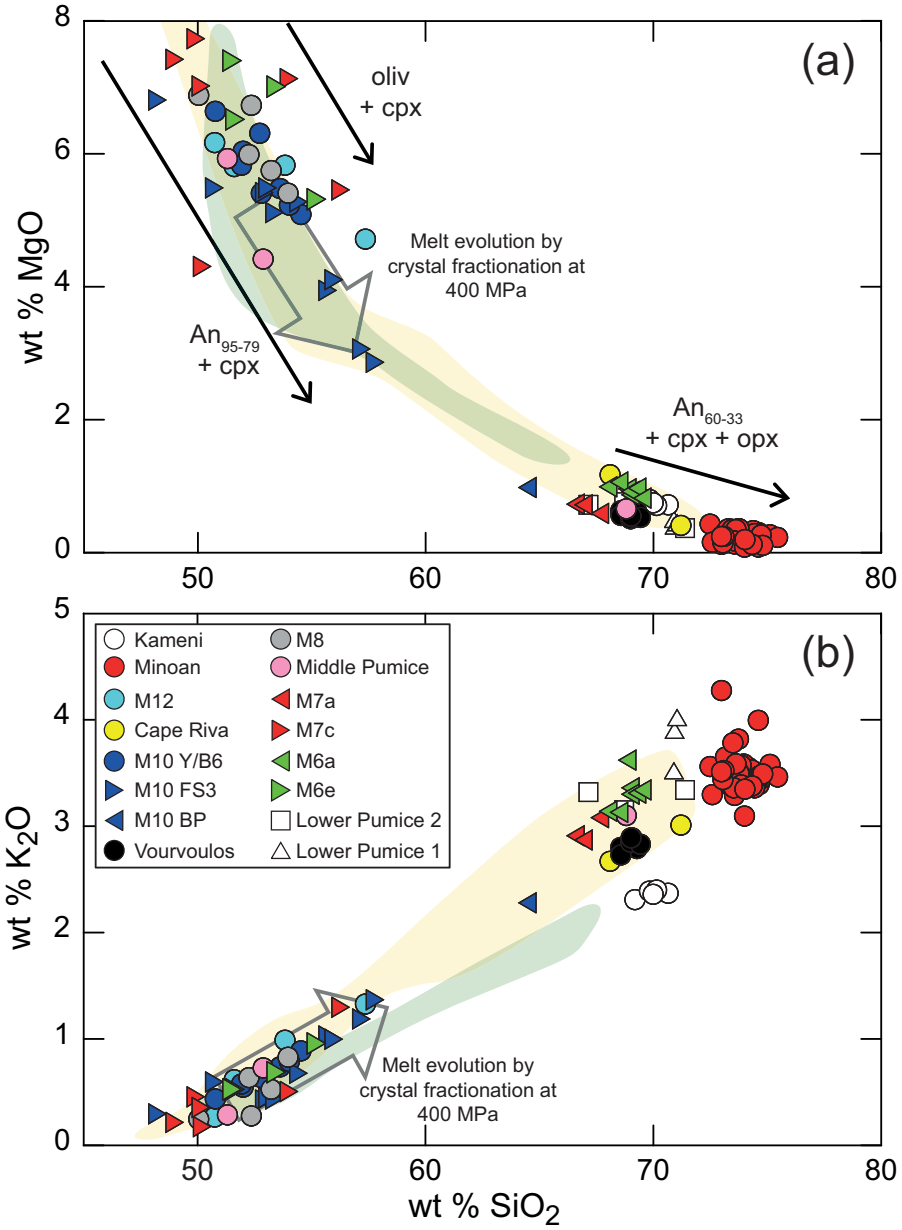


**Fig. 5.** Silica variation diagrams for (a) MgO and (b) $K_2O$ of the MIs analysed in this study. Compositional fields of whole-rocks from cycle 2 (yellow) and cycle 3-Kameni (green) are shown for comparison. The large arrows show the melt evolution vectors of fractional crystallization of Santorini basaltic melt in experiments at 400 MPa from Andújar *et al.* (2015).

$K_2O$ increases approximately linearly with increasing $SiO_2$ (Fig. 5b). Potassium behaves incompatibly in almost all but the oldest (>550 ka) Santorini magmas (Mann, 1983; Huijsmans *et al.*, 1988; Huijsmans & Barton, 1989; Druitt *et al.*, 1999; Gertisser *et al.*, 2009). This is because K feldspar is absent as a phenocryst phase. We therefore use $K_2O$ as a proxy for degree of fractional crystallization, but caution that this is approximate because modelling of Santorini magmas requires ~10% of crustal contamination to explain the contents of incompatible elements such as K in more evolved compositions (Barton *et al.*, 1983; Druitt *et al.*, 1999). Another complication is that the content of K (and other incompatible elements such as Th, Rb, Nb and Zr) decreases with time at Santorini (Huijsmans *et al.*, 1988; Fabbro *et al.*, 2013). Hence in Fig. 5b Lower Pumice 1, Lower Pumice 2, M6a, M7a and Middle Pumice have higher $K_2O$ than Vourvoulos, M10BP and Cape Riva, whereas Kameni melts have the lowest $K_2O$ of all at a given $SiO_2$ content. The different liquid lines of descent are in detail only approximately cogenetic.

## Sulphur and halogens

The S, Cl and F contents of the MI suites are shown in Fig. 6 as functions of $K_2O$. Sulphur contents are up to 1200 ppm in basaltic compositions; they decrease rapidly in a nonlinear fashion to ~100 ppm in silicic compositions (Fig. 6a). This range is typical of arc magmas

(Wallace, 2005). The different MI lineages also show decreasing S with increasing $K_2O$; M10 Y/B6 shows the steepest depletion trend, and M12 the shallowest. The overall trend for S resembles those published previously by Michaud *et al.* (2000), Gertisser *et al.* (2009) and Vaggelli *et al.* (2009).

Chlorine contents range from ~500 ppm in basaltic MIs to 2500–6000 ppm in silicic ones, with an overall trend that is almost flat at the mafic end, but that steepens with increasing $K_2O$ (Fig. 6b). At the mafic end of the spectrum, MIs from interplinian units M6e, M8-MSF, M7c and M12 form gently sloping arrays parallel to the overall trend. The highest Cl values are from the silicic plinian units (Lower Pumice and Minoan).

The F contents of the MIs range from <100 to 400 ppm in the mafic part of the spectrum, and from 600 to 1000 ppm in the silicic part (Fig. 6c). Overall the analyses form a linear trend with considerable scatter, in part owing to the large analytical error on this element. Arrays of MIs from single units scatter too much for distinct trends to be recognized. Indeed, MIs from single units plot with a range of F/K ratios. The highest F contents are found in MIs from the silicic plinian units.

## $H_2O$ contents

The variation of $H_2O$ contents is plotted in Fig. 7a versus $K_2O$; the data scatter considerably. That this scatter is real is shown by MIs from the Vouvourlos plinian eruption, which are large and very homogeneous. Seven of these inclusions give $H_2O$ of $3{\cdot}39 \pm 0{\cdot}17$ ($1\sigma$) wt %, which agrees with the uncertainty (±5%) on the $H_2O$ values based on SIMS data calibration.

Water contents in the mafic MIs range from 1·1 to 4·3 wt %, and those in silicic MIs from 2·2 to 6·9 wt % (Table 3). In the five units that yield both bubble-bearing and bubble-free MIs, the range of $H_2O$ content is essentially independent of whether a bubble is present or not (Table 3), showing that little $H_2O$ was partitioned into the shrinkage bubble upon quench. Moreover, in four units in which both olivine-hosted and plagioclase-hosted MIs were analysed, there is no obvious difference in MI $H_2O$ contents between the two hosts (Fig. 8a). Only in interplinian unit M10 FS3 are there olivine-hosted MIs with $H_2O$ significantly lower than the plagioclase-hosted MIs, but this is because the $H_2O$ content of MIs in this unit is positively correlated with $K_2O$ content, and those olivine-hosted inclusions with the lowest $H_2O$ are particularly poor in $K_2O$. When MIs with the same $K_2O$ are compared in unit M10 FS3, $H_2O$ content is independent of mineral host (Table 3).

MIs from single units form subhorizontal arrays in Fig. 7a, with $H_2O$ content increasing only very slightly with increasing $K_2O$. This is particularly clear for MIs from units M7c, Middle Pumice, M8-MSF and M12. It is also evident from vectors linking closely related pairs of mafic and silicic units such as M6e to M6a and M7c to M7a. MIs of M10-FS3 with <1 wt % $K_2O$ fall on a steeper positive trend that passes through the origin of the $H_2O$–$K_2O$ plot, whereas those with >1 wt % $K_2O$ define a horizontal trend (Fig. 7a).

MIs from the plinian units exhibit a broad range of $H_2O$ contents over a small range of $K_2O$. $H_2O$ in the 62 MIs analysed from Minoan rhyodacitic pumice ranges from 4·0 to 6·9 wt % (Table 3). MIs in the cores ($An_{50 \pm 7}$; Druitt *et al.*, 2012) of plagioclase crystals in these pumices contain 4·6–6·9 wt % $H_2O$, whereas those in the rims ($An_{43 \pm 3}$) contain 4·0–5·0 wt % $H_2O$. MIs in pyroxenes in the same pumices contain 4·1–4·7 wt % $H_2O$. The total range of $H_2O$ contents in Minoan MIs agrees well with the data of Cottrell *et al.* (1999) (3·5–6·5 wt %) and Cadoux *et al.* (2014) (4·0–5·8 wt %). Two MIs in a volumetrically minor andesitic component in the Minoan (microphenocryst-rich andesitic pumice; Druitt, 2014) contain 5·4 and 6·6 wt % $H_2O$.

In general, MIs from the plinian units contain more (>3·5 wt %) $H_2O$ than the interplinian ones (<3·5 wt %). This is true of mafic as well as silicic compositions; the two mafic MIs from the Middle Pumice plinian unit are richer in $H_2O$ than those from all the mafic interplinian MIs. However, there are two exceptions. First, MIs of the Vourvoulos plinian eruption plot at the limit, and slightly on the interplinian side, and this is consistent with Vourvoulos being the thinnest (and probably least voluminous) of the plinian units recognized by Druitt *et al.* (1999). Second, MIs from the AD 726 explosive eruption of Kameni Volcano have $H_2O$ contents more typical of plinian MIs. The ratio $Cl/H_2O$ in all the MIs is <0·15 and increases with $SiO_2$ content (Fig. 9).

## $CO_2$ contents

The data for $CO_2$ are plotted against $H_2O$ in Fig. 7b. Concentrations of $CO_2$ in the MIs range from <50 ppm (the detection limit) to 1200 ppm. Contents in most of the mafic MIs are <230 ppm; only olivines of unit M10 FS3 and M10 Y/B6 contain MIs with higher $CO_2$. The M10 FS3 and M10 Y/B6 data form parallel, vertical, trends at different $H_2O$ contents. All silicic MIs contain < 150 ppm $CO_2$. No relationship is observed in MIs from Minoan pumice between $CO_2$ content and position in the crystal or in different mineral phases.

As for $H_2O$, there is no significant difference between the $CO_2$ contents of bubble-bearing and bubble-free MIs (Fig. 8b). Bubbles in the MIs are empty and lack any $CO_2$ liquid phase visible under high magnification. The $CO_2$ contents of shrinkage bubbles from two olivine-hosted mafic MIs (sample M12) and four plagioclase-hosted silicic MIs (samples S12-67 and PKB) were found to lie below the detection limit of our micro-Raman spectrometer; the Fermi couplet typical of molecular $CO_2$ (~1285 and ~1385 $cm^{-1}$) was absent in all six bubbles studied.

## D/H isotopic ratios

Hydrogen isotopic ratios of 27 representative MIs (12 olivine-hosted; 15 plagioclase-hosted) with compositions ranging from basaltic to silicic, range from

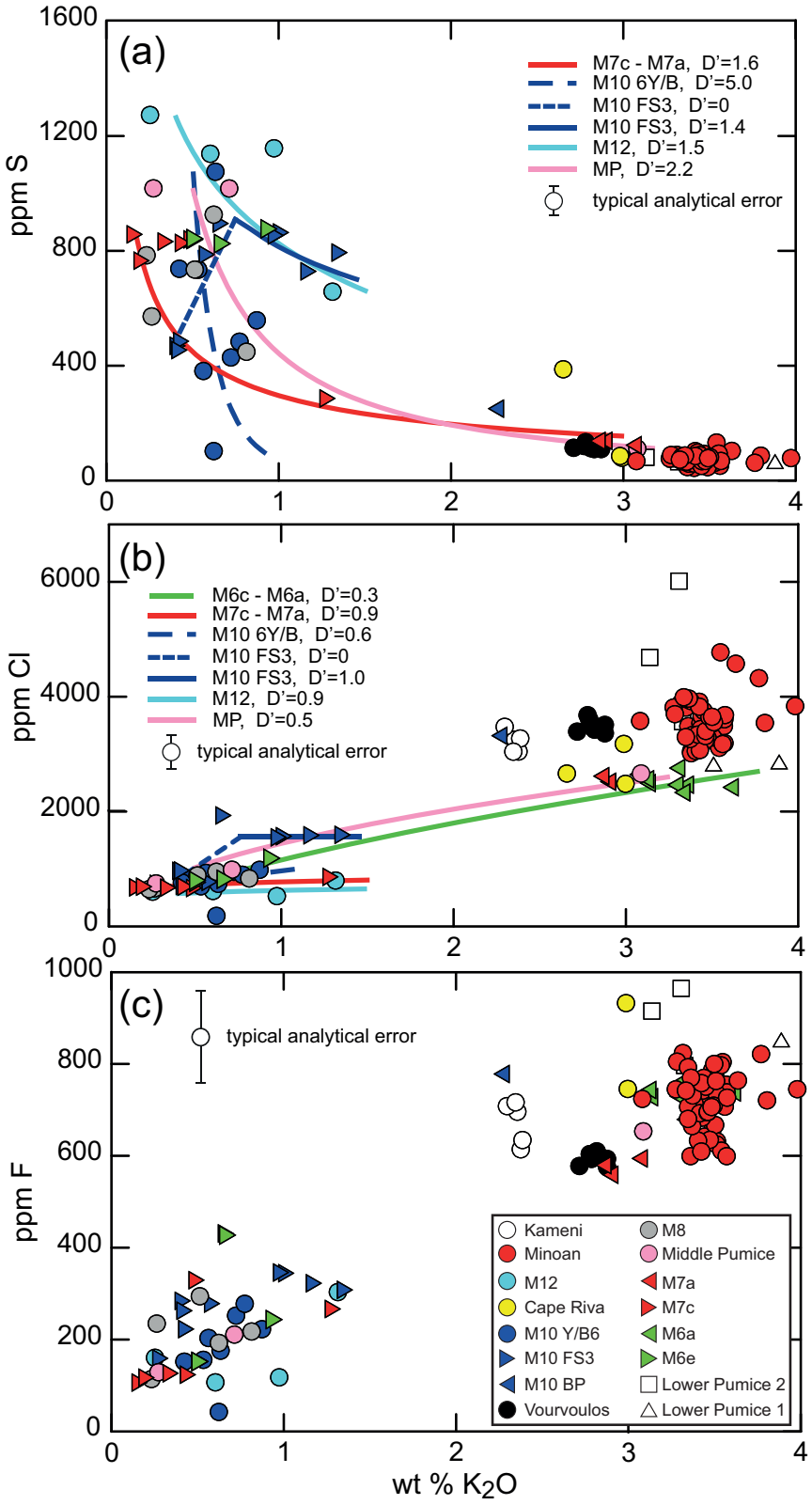


**Fig. 6.** Variations of (a) S, (b) Cl and (c) F contents with $K_2O$. Lines show models of crystallization-modified Rayleigh distillation of several of the different melt inclusion series, as explained in the text and in Table 4.

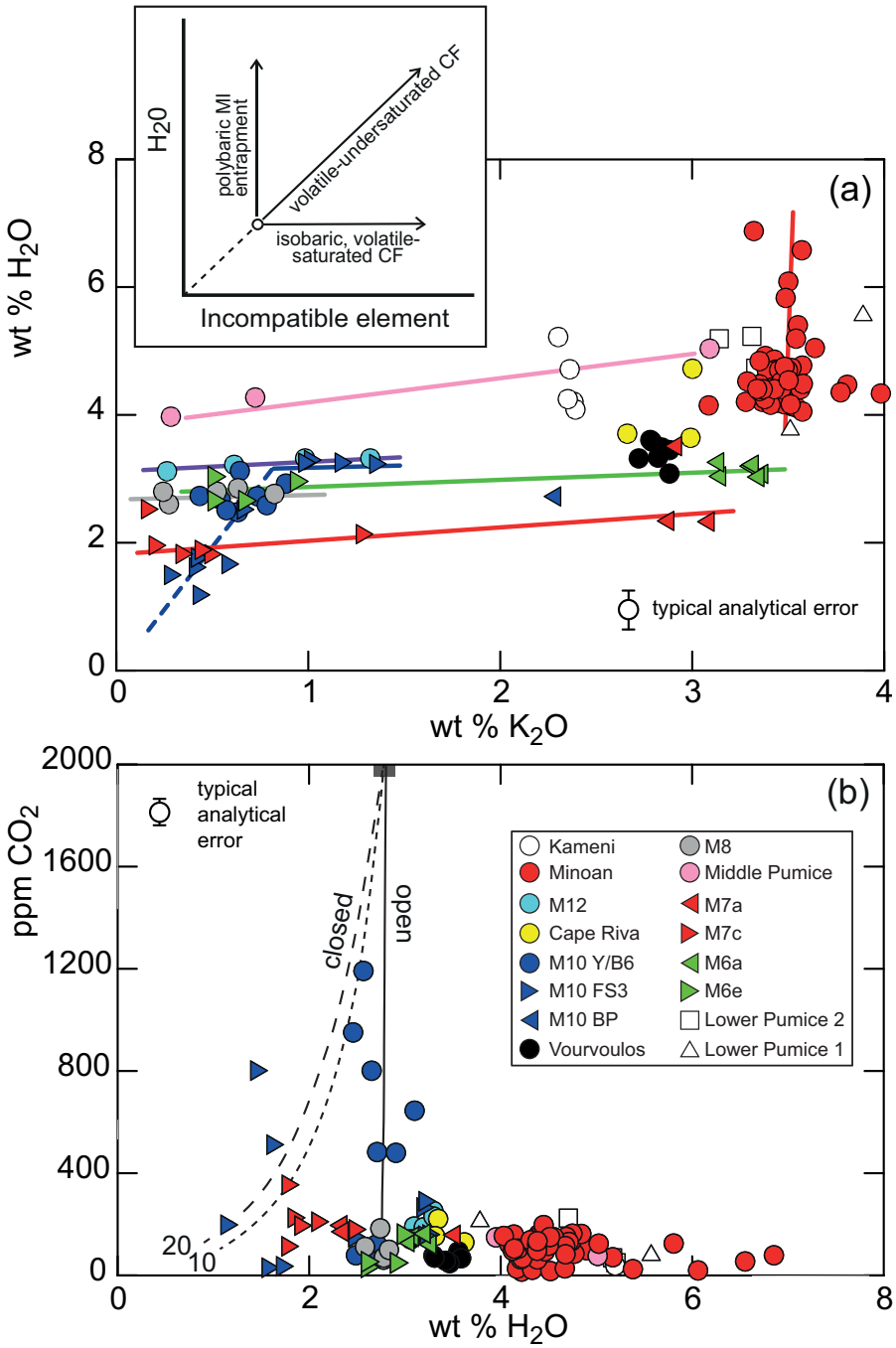


**Fig. 7.** (a) Variation of melt $H_2O$ vs $K_2O$. $K_2O$ is an incompatible component in Santorini magmas. The coloured lines show the trends (fitted by eye) of each of the following related samples: mafic to silicic MIs from the Middle Pumice, M6e to M6a, and M7c to M7a series; compositionally diverse mafic MIs from M10, M8-MSF and M12; compositionally uniform MI from the Minoan. Different theoretical trends on such a plot are shown in the inset (CF, crystal fractionation). Most of the trends are essentially flat, showing that $H_2O$ behaves compatibly (volatile-saturation) during differentiation (in fact, the trends are gently inclined because wt % $H_2O$ solubility increases with increasing $SiO_2$ content). There is one exception: MIs from unit M10 FS3 with $<1$ wt % $K_2O$ lie on a trend of volatile-undersaturation for $H_2O$, whereas those with $>1$ wt % $K_2O$ lie on a trend of volatile-saturation. MIs from the Minoan eruption exhibit a range of $H_2O$ contents at approximately constant $K_2O$, and this is interpreted as due to polybaric entrapment. (b) $CO_2$ vs $H_2O$ for the MIs. The black lines show model degassing trends under open and closed (10% gas and 20% gas) conditions, calculated using VolatileCalc (Newman & Lowenstern, 2002) for a 1050°C basaltic melt with 2·8 wt % $H_2O$ and 2000 ppm $CO_2$.

$\delta D = -37$ to $-104$‰, with no evident correlation with either $SiO_2$ or $H_2O$ contents (Fig. 10). MIs from sample M10 FS3, which contain a range of $H_2O$ contents in both olivine and plagiclase hosts, show no significant variation of $\delta D$ with $H_2O$. Overall the $\delta D$ values are similar to those of eight Santorini whole-rocks analysed by Druitt *et al.* (1999) (–54 to –81‰); they also lie between the value of mid-ocean ridge basalt (MORB; $-80 \pm 10$‰) and the estimated value of slab fluids (–34‰) (Shaw *et al.*, 2008).

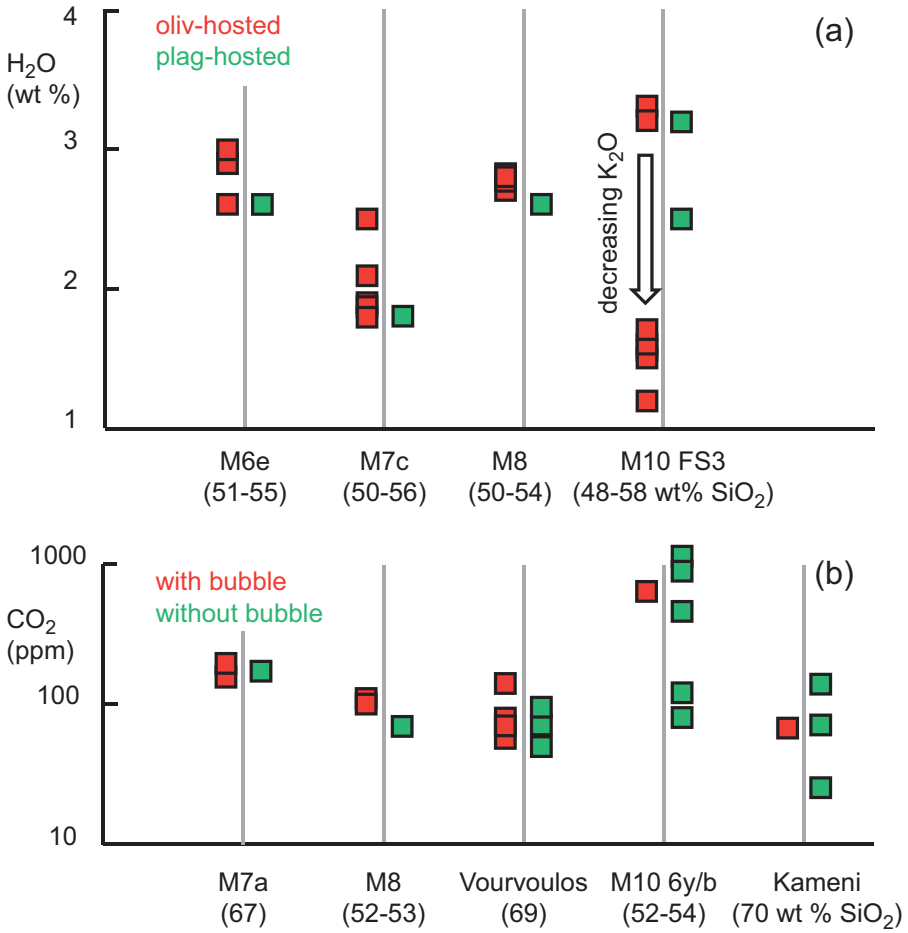


**Fig. 8.** (a) $H_2O$ contents of melt inclusions (MIs) from four samples, showing that there are no systematic differences in $H_2O$ between MIs hosted by olivine and those hosted by plagioclase. Indeed, the contents in olivine-hosted MIs are if anything a little higher than those in plagioclase. This suggests that the olivine-hosted MIs retain most of their original magmatic $H_2O$. The large spread of $H_2O$ contents in sample M10 FS3 is related to increasing degree of melt evolution. (b) $CO_2$ contents of MIs in five samples, showing that there are no systematic differences in $CO_2$ between those MIs that contain shrinkage bubbles and those that do not. This strongly suggests that $CO_2$ has not been sequestered from the melt into the bubble during quench. The numbers in parentheses are the silica contents of the MIs.

## CALCULATED INTENSIVE PARAMETERS

### Entrapment temperatures

Entrapment temperatures for the MIs were calculated using three thermometers: the Putirka (2008) formulation for olivine–melt [his equation (22)] and the Putirka [2008; equation (24a)] and Lange *et al.* (2009) formulations for plagioclase–melt. In each case, we computed the temperatures from major element compositions of the MIs and their host mineral phases, along with SIMS-derived $H_2O$ contents. When plotted as a function of $K_2O$ (Fig. 11), the olivine–melt and Putirka plagioclase–melt temperatures form a coherent trend, showing that they are mutually consistent. Almost all the temperatures from Lange *et al.* (2009) are higher (average + 20°C, and as high as + 85°C) than those from Putirka (2008) (inset, Fig. 11).

The calculated temperatures for interplinian MIs decrease from ~1150°C to ~950°C with decreasing $K_2O$ content. Silicic MIs from the plinian units yield systematically lower temperatures (down to 800°C) than the interplinian silicic MIs, owing to their higher $H_2O$ contents. Our only two mafic MIs from a plinian unit (Middle Pumice) give lower temperatures than most mafic interplinians, again owing to their higher $H_2O$ contents. Overall the temperatures agree with those obtained previously for Santorini from coexisting Fe–Ti oxides, MI rehomogenization, and phase equilibrium experiments (Cottrell *et al.*, 1999; Druitt *et al.*, 1999; Michaud *et al.*, 2000; Cadoux *et al.*, 2014; Druitt, 2014), although values for intermediate compositions are 50–100°C higher than previous estimates (Fig. 11). The plagioclase–melt temperatures of Lange *et al.* (2009), being slightly higher than those of Putirka (2008), are less consistent with the temperatures from other methods. We therefore use the Putirka temperatures in calculating volatile saturation pressures.

### Volatile saturation pressures

Calculation of $H_2O + CO_2$ saturation pressures requires use of solubility models calibrated within the range of our

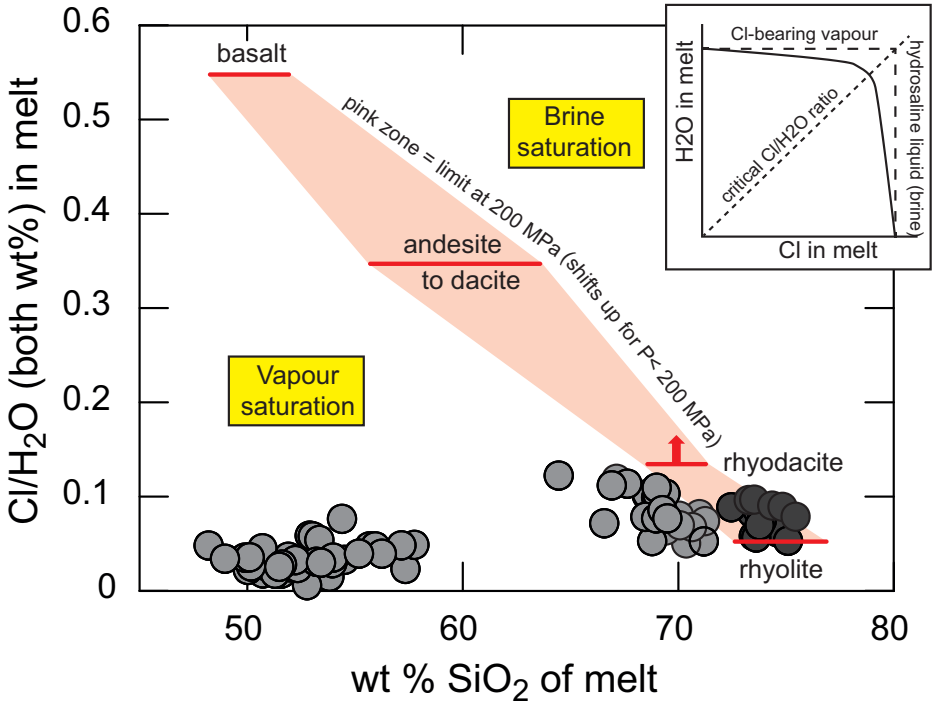


**Fig. 9.** $Cl/H_2O$ ratios for the melt inclusions as a function of $SiO_2$ content. The red bars (within the pink field) are experimentally determined values separating vapour-saturated from brine-saturated fields at 200 MPa; from Webster (2004). Lowering the pressure shifts these values upwards. Melt inclusions from the Minoan eruption are shown in dark grey.

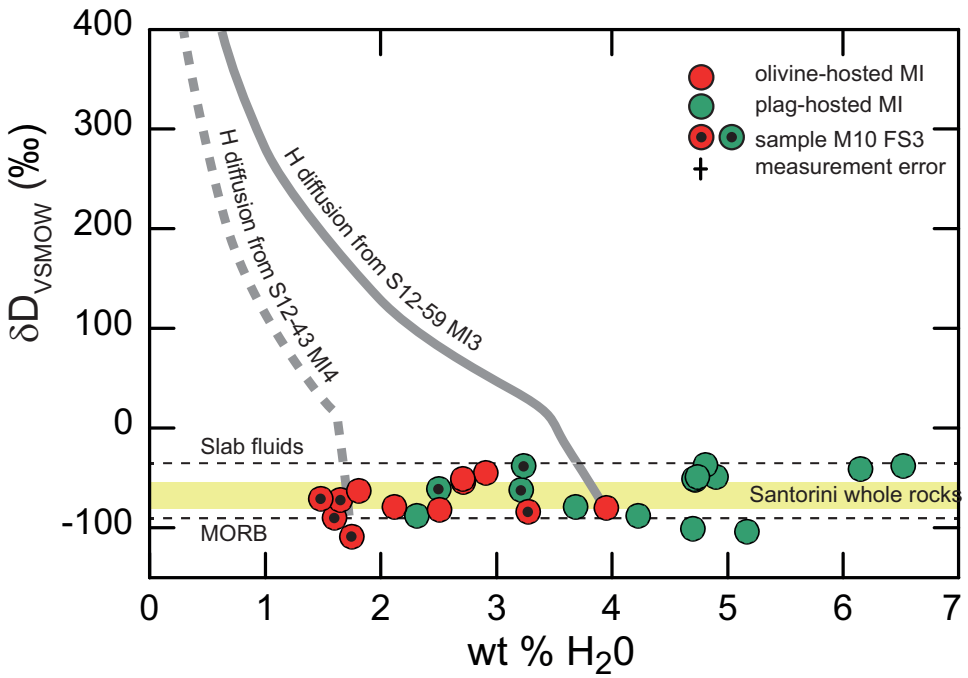


**Fig. 10.** Variation of δD vs $H_2O$ content for 27 melt inclusions (MIs). The δD values agree with those of Santorini whole-rocks (yellow field; Druitt *et al.*, 1999), and lie within a narrow range of values between those of MORB and slab fluids (Shaw *et al.*, 2008). The grey lines are models of δD–$H_2O$ evolution owing to hydrogen diffusion for two representative inclusions (continuous line: S12-59 MI 3, 3·95 wt ‰ $H_2O$, –80‰ δD, 1077°C, 48 μm MI radius, 300 μm host olivine radius; dotted line: S12-43 MI 4, 1·75 wt ‰ $H_2O$, –109‰ δD, 1101°C, 32 μm MI radius, 300 μm host olivine radius). The model used was that of Bucholz *et al.* (2013); this shows that none of the olivine-hosted MIs have lost significant $H_2O$ by this mechanism. Symbols with dots are MIs from unit M10 FS3; all MIs from this unit (either olivine-hosted or plagioclase-hosted) lie in the same δD range, showing that none of the olivine-hosted MIs, which have particularly low $H_2O$ contents, have lost significant amounts of $H_2O$ by hydrogen diffusion; the low $H_2O$ contents are therefore interpreted to be original.

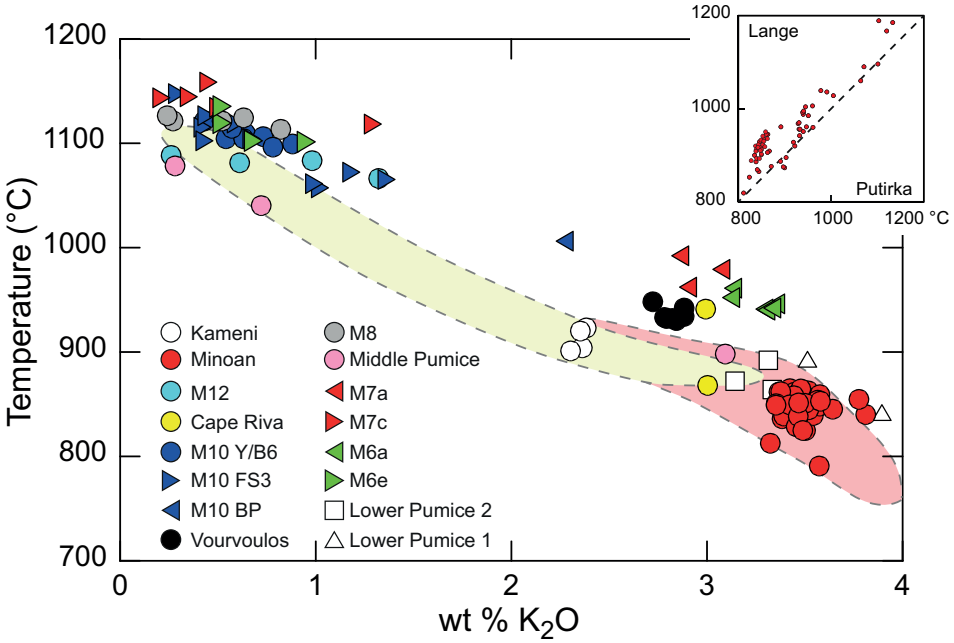


**Fig. 11.** Variation of melt inclusion equilibration temperature, derived from olivine–melt and plagioclase–melt equilibria. For olivine–melt we used equation (22) of Putirka (2008). For plagioclase–melt we used equation (24a) of Putirka (2008). The plagioclase–melt model of Lange *et al.* (2009) gives slightly higher temperatures than that of Putirka (see inset). The results are compared with previously published temperature estimates: melt inclusion rehomogenization temperatures of Michaud *et al.* (2000) (yellow field), and Fe–Ti oxide temperatures of Cadoux *et al.* (2014) and Druitt (2014) (pink field).

MI data. Four main appropriate models exist, as reviewed by Moore (2008). Dixon *et al.* (1995) and Dixon (1997) developed a regular solution model for the solubility of $H_2O$ and $CO_2$ in basaltic melts, ranging from tholeiite to nephelinite in composition. The melt composition was accounted for by a compositional parameter $\Pi$, which in the melts used for the $CO_2$ calibration in their model ranges from 0·5 (tholeiitic) to 2·2 (highly alkaline). The model VolatileCalc (Newman & Lowenstern, 2002) is based on pure species solubility data and linear mixing of $H_2O$ and $CO_2$. The program has a model for rhyolite and a model for basalt that is based on the Dixon (1997) formulation, valid for melts with $<52$ wt % $SiO_2$. The basaltic model assumes a linear correlation between $SiO_2$ content and parameter $\Pi$ of Dixon (1997). The SolEx program of Witham *et al.* (2012) for basaltic melts also uses the Dixon (1997) formulation, but with the full parameter $\Pi$, and it also incorporates partition laws for S and Cl. SolEx is applicable only to basalts ($\leq$53 wt % $SiO_2$). The most complete model is that of Papale (1999), modified by Papale *et al.* (2006), which uses a multivariate regression of a large dataset of published $H_2O$, $CO_2$ and $H_2O + CO_2$ solubility data in melts ranging from basalt to rhyolite in composition.

Moore (2008) compared the results of the VolatileCalc and Papale models against recent experimental data and reached the following conclusions: (1) VolatileCalc (basalt) overestimates saturation pressure $P_{sat}$ in some calcic and calc-alkaline basalts, whereas these can be underestimated by Papale; (2) Papale satisfactorily recovers $P_{sat}$ for a calc-alkaline andesite (57 wt % $SiO_2$) and a dacite (66 wt % $SiO_2$) at 200–400 MPa, whereas VolatileCalc does not; (3) both VolatileCalc (rhyolite) and Papale recover $P_{sat}$ for metaluminous rhyolite to $\pm$10% relative. Witham *et al.* (2012) showed that the Dixon model can overestimate $P_{sat}$, particularly at $>$300 MPa, and that Papale can underestimate it, in agreement with Moore (2008).

Basaltic ($<$53 wt % $SiO_2$) MIs in our dataset have $\Pi$ values of –0·8 to +0·6, which lie outside the Dixon (1997) $CO_2$ calibration used by both VolatileCalc and SolEx, and this is in accord with the calc-alkaline nature of Santorini melts. On the other hand, the andesite and dacite modelled well by the Papale model (Moore, 2008) are both very similar compositionally to Santorini melts. Similarly, Santorini rhyolitic melts are metaluminous to very slightly peraluminous, and hence lie within the calibration of VolatileCalc (rhyolite). The total compositional range of our MIs overlaps completely the spread of melt data used by Papale *et al.* (2006) to calibrate their model.

We apply the following approach to our MI data: (1) $P_{sat}$ for basaltic MIs are estimated using the SolEx formulation of the Dixon model (maximum $P_{sat}$ estimate) and using the Papale model (minimum $P_{sat}$ estimate); (2) $P_{sat}$ values for mafic andesitic MIs are estimated using the Papale model (minimum $P_{sat}$ estimate); (3) $P_{sat}$ for silicic andesitic, dacitic and rhyodacitic MIs are estimated using the Papale model; (4) $P_{sat}$ for rhyolitic MIs are estimated using VolatileCalc (rhyolite) and the Papale model. The resulting $H_2O + CO_2$ pressures are shown in Fig. 12. Precisions on the pressures, owing to analytical errors in $H_2O$ and $CO_2$ and to uncertainties in the temperatures, are about $\pm$10 MPa.

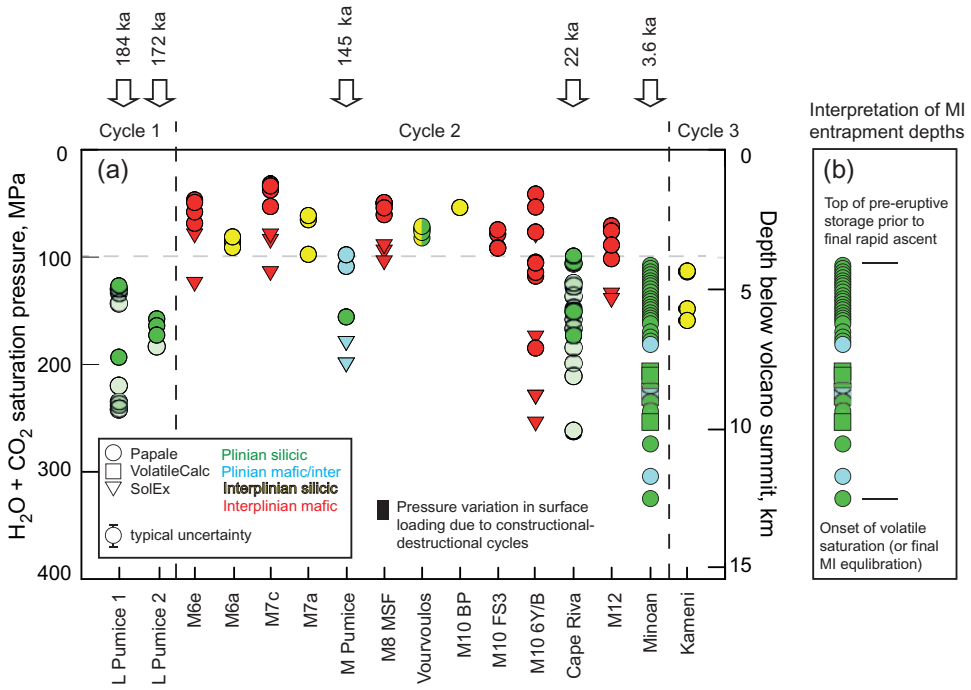


**Fig. 12.** (a) $H_2O + CO_2$ saturation pressures for the melt inclusion suites as a function of time. (See the text for justification of the different solubility models used.) Given the evidence for volatile saturation presented here, the pressures are interpreted as total pressures and are converted into depths using the mean density of the upper crust beneath Santorini (2640 kg $m^{-3}$; Konstantinou, 2010). The depth is that below the summit of the volcano at that time, and the surface edifice load has varied by ~750 m (18 MPa) between pre-plinian and interplinian states. Volatile-undersaturated MIs from unit M10 FS3 are not shown. Filled symbols are from this study; pale green symbols are data from Cadoux *et al.* (2014), as described in the text. The effect of high Cl contents in silicic melts could be to increase the saturation pressures based on $H_2O + CO_2$ by a factor of as much as ~1·2. (b) Our interpretation of the MI entrapment depth ranges, using the Minoan data as an example.

We include in Fig. 12 a series of 27 MIs analysed by Cadoux *et al.* (2014) for $H_2O$, but not $CO_2$. By reanalysing three of their MIs using our standards and calibration technique, we confirmed that the two $H_2O$ datasets are comparable; the $H_2O$ contents obtained by us are close to those obtained by Cadoux *et al.* (2014), despite slightly different calibration procedures (S09-62f-10 MI 1 5·27 and 5·40, S09-62f-10 MI 2 4·74 and 4·96, and S09-17 c-1 MI 1 2·45 and 2·00, the first value being Cadoux *et al.*'s wt % $H_2O$, and the second being ours). However, because Cadoux *et al.* selected their MIs prior to analysis in two dimensions, not three dimensions, $H_2O$ leakage through fractures or surface-connected melt tubes cannot be excluded. We therefore include only their MIs with $H_2O$ contents higher than our minimum value, on the reasoning that their higher $H_2O$ values are likely to be original.

The pressures plotted in Fig. 12 assume that total pressure equals the sum of the partial pressures of $H_2O$ and $CO_2$. However, the presence of dissolved S and halogens could increase the actual $p_{sat}$ for given values of $p_{H2O}$ and $p_{CO2}$, through $p_{sat} = p_{H2O} + p_{CO2} + p_S + p_{Cl} + p_F$. Another way of looking at this is that the presence of S, Cl and F decreases the solubilities of $H_2O$ and $CO_2$, for a given value of $p_{sat}$. The effect of dissolved S on estimation of $p_{sat}$ in basaltic melts has been discussed by Lesne *et al.* (2014). They showed that S contents typical of our MIs (<1300 ppm) will increase the estimated $p_{sat}$ by no more than ~20 MPa at redox conditions typical of Santorini magmas (QFM–NNO; Gertisser *et al.*, 2009; Cadoux *et al.*, 2014; Druitt, 2014; Andújar *et al.*, 2015). This effect can therefore be neglected. The effect of Cl on $H_2O$ solubility has been studied extensively at 200 MPa (Webster, 2004). Experiments show that $H_2O$ solubility is unaffected by <10,000 ppm Cl in basaltic, andesitic and latitic melts (Webster *et al.*, 1999; Botcharnikov *et al.*, 2007; Stelling *et al.*, 2008). Rhyolitic melts can, however, exhibit greater sensitivity within the range of pressures of interest. For example, $H_2O$ solubility in a haplogranite melt at 200 MPa can be reduced significantly by Cl contents of >2000 ppm. However, such Fe-free compositions may not be applicable to natural silicic melts (Cadoux *et al.*, 2014). Botcharnikov *et al.* (2004) have studied H–O–Cl–S solubility in a natural rhyodacitic melt, and the $H_2O$ melt contents listed in their Table 3, although imprecise, suggest a drop in $H_2O$ solubility of ~10% (relative) as melt Cl content increases from 0 to 6000 ppm (the highest content of our MIs). Indeed, this would be consistent with the conclusion of Cadoux *et al.* (2014), based on their phase equilibria study of magmas from the four largest plinian eruptions, that Santorini silicic melts are saturated in $H_2O$–Cl-rich fluid, but slightly undersaturated with respect to pure $H_2O$. The effect of high Cl in our silicic melts would therefore be equivalent

to increasing saturation pressure based solely on $H_2O + CO_2$ by an amount equivalent to ~10% (relative) of $H_2O$, that is to say by a factor of about 1·2. The solubility of $H_2O$ in rhyolitic melts is independent of F content up to 6 wt % of dissolved F (Webster, 1990); the effect of $\leq$1000 ppm in our MIs is therefore negligible in this respect.

## INTERPRETATION OF THE VOLATILE DATA

### Entrapment and post-entrapment modification of MI compositions

Use of MI volatile contents in estimating entrapment depths requires that the MIs record equilibrium melt compositions. Entrapment of the boundary layer at a crystal–melt interface can potentially result in concentrations of slower-diffusing elements in MIs that are higher than equilibrium far-field melt values (Faure & Schiano, 2005). However, most of our MIs are larger than 40 μm, suggesting minimal boundary layer effects (Lu *et al.*, 1995). Morever, experiments and modelling of MI entrapment and diffusive re-equilibration show that $H_2O$ (also $K_2O$) diffuses sufficiently fast that values in MIs should record equilibrium values. The measured concentrations of slower-diffusing S, Cl, F and $CO_2$ could, however, somewhat overestimate equilibrium values.

Volatiles can be lost from MIs following entrapment by leakage along crystal fractures or by diffusion through 3D melt networks connected to the crystal surface (Anderson *et al.*, 1989; Wallace, 2005; Liu *et al.*, 2007; Humphreys *et al.*, 2008). We exclude loss of significant $H_2O$ and $CO_2$ by these processes, because all of the MIs selected were ellipsoidal, isolated, and lacked textural evidence for crystal fracturing.

Melt inclusions within olivine can also lose $H_2O$ by hydrogen diffusion through the host crystal during syn-eruptive decompression and posteruptive cooling on timescales as short as a few hours (Hauri, 2002; Chen *et al.*, 2011, 2013; Gaetani *et al.*, 2012). MIs in bombs can lose more water than those in lapilli and ash from the same eruption, because the bombs take longer to cool (Lloyd *et al.*, 2013); however, even MIs in lapilli and ash can lose $H_2O$ on the timescale of an eruption (Le Voyer *et al.*, 2014). Loss of $H_2O$ from our olivine-hosted MIs by H diffusion during, or after, eruption is believed to be unimportant, for the following reasons. First, the olivine-hosted MIs were all extracted from lapilli-sized (0·5–1 cm radius) fallout tephra, which would have cooled within a few minutes in the atmosphere (Thomas & Sparks, 1992). Second, the olivine-hosted MIs have similar $H_2O$ contents to plagioclase-hosted MIs with the same $K_2O$ content from the same sample (Fig. 8a). Third, the MIs lack the heavy magnetite 'dusting' indicative of significant $H_2O$ loss (Danyushevsky *et al.*, 2002), and there is no correlation between MI $H_2O$ content and size (Chen *et al.*, 2011). Fourth, δD values of a representative subset of MIs lie within a narrow range of values that is similar to that of Santorini whole-rock samples (Druitt *et al.*, 1999), and that lies between the values of mantle and slab-derived fluids (Shaw *et al.*, 2008). δD is very sensitive to $H_2O$ loss by hydrogen diffusion, as H diffuses faster than D, thereby resulting in a large increase in δD (Hauri, 2002; Gaetani *et al.*, 2012; Bucholz *et al.*, 2013). In Fig. 10 we show two curves for δD increase as a function of $H_2O$ loss using the H diffusion model of Bucholz *et al.* (2013). The narrow range of observed MIs δD values rules out syn-eruptive loss of $H_2O$ by H diffusion in excess of about 0·2 wt %. Even the lowest MI $H_2O$ contents observed (<2 wt %; units M7c and M10 FS3) cannot be attributed to H diffusion, as their δD values are no higher (and if anything are a little lower) than those of MIs richer in $H_2O$ from the same units.

Pressure changes in MIs during ascent and cooling can cause partitioning of $CO_2$ from melt into bubbles (Anderson & Brown, 1993; Bucholz *et al.*, 2013; Hartley *et al.*, 2014). $CO_2$ contents of bubbles in six representative MIs of mafic to silicic composition are below the detection limit of our Raman spectrometer. Assuming a detection limit $CO_2$ density of ~0·04 g $cm^{-3}$ as used by Neave *et al.* (2014), and 'adding back' the bubble $CO_2$ in the same way as those researchers, the original $CO_2$ contents of our MIs could be underestimated by as much as 20–4500 (average 615) ppm. The lack of detection by Raman spectrometry therefore places only weak limits on any $CO_2$ sequestration into bubbles. More convincing evidence that $CO_2$ sequestration was minimal is the lack of any systematic differences in $CO_2$ contents between MIs containing bubbles and those lacking them in the same sample (Fig. 8b). This is consistent with most bubbles being shrinkage bubbles formed rapidly upon sample quench. Although we cannot exclude some $CO_2$ loss to bubbles, the effect appears not to have been large.

We conclude that our MIs (1) have near-equilibrium $H_2O$ contents, (2) have not (in olivine) been significantly modified syn- or post-eruptively by the H diffusion mechanism, and (3) have lost minimal $CO_2$ to retraction bubbles. They therefore provide meaningful information about MI entrapment conditions and pre-eruptive magma storage in the crust.

### Behaviour of volatiles in Santorini magmas

The data provide evidence for entrapment of many MIs under volatile-saturated conditions, as typical of arc magmas (Scaillet *et al.*, 2003; Wallace, 2005). $H_2O$ dissolved in the MIs increases only very slightly with increasing $K_2O$, and much less than expected from incompatibility (Fig. 7a). This is particularly clear in the case of some of the mafic MI series, which exhibit almost constant $H_2O$ over a range of $K_2O$ contents (Fig. 7a). There are very few occurrence of hydrous crystalline phases in <550 ka Santorini magmas, amphibole occurring only sparsely in some magmatic components of the Lower Pumice 2 and Minoan eruptions (Cottrell

*et al.*, 1999; Gertisser *et al.*, 2009; Druitt, 2014); so it follows that $H_2O$ must partition into an $H_2O$-rich fluid phase during melt crystallization and MI entrapment.

This conclusion holds even if Santorini magmas experience 'cryptic' amphibole fractionation. Many arc volcanic suites show differentiation trends that are consistent with amphibole fractionation, even if they lack modal amphibole at low pressures (Davidson *et al.*, 2007; Smith, 2014). Increasing La/Yb and decreasing Dy/Yb ratios (chondrite-normalized) with increasing $SiO_2$ at Santorini suggest that amphibole may indeed be a fractionating phase at depth (Gertisser *et al.*, 2009), it being stable in Santorini basalt at melt $H_2O$ contents of $>4$ wt % and temperatures of $<1000^{\circ}C$ (Andújar *et al.*, 2015). However, amphibole would have a minimal effect on melt $H_2O$ content during crystallization, because it contains only $\sim$2·5 wt % $H_2O$ (Cottrell *et al.*, 1999; Gertisser *et al.*, 2009). Let us suppose that a parental basalt with 2 wt % $H_2O$ fractionates by 80% crystallization to a silicic residual melt under $H_2O$-undersaturated conditions. Simple mass balance shows that the $H_2O$ content of the residual melt would be 10 wt % in the case of an entirely anhydrous crystal assemblage, and 8 wt % if amphibole made up a fifth of the crystals. Even if half the crystals were amphibole, the residual melt would still contain 5 wt % $H_2O$, so the $H_2O$ content of amphibole is too low to buffer melt $H_2O$ at an approximately constant value during crystallization. The $H_2O$ contents in Fig. 7a remain approximately constant because $H_2O$ was extracted by an exsolved fluid phase during crystallization under a limited range of pressures (see below). These observations support the previous findings of Cadoux *et al.* (2014) that plinian silicic melts at Santorini coexisted with an $H_2O$-rich fluid phase prior to eruption.

The only melts that may have been volatile-undersaturated are those of basaltic interplinian M10 FS3. MIs of this unit with $<1$ wt % $K_2O$ fall on a positive trend that passes through the origin on the $H_2O$–$K_2O$ plot, whereas MIs with $>1$ wt % $K_2O$ fall on a flat trend (Fig. 7a). The least evolved MIs of this sample cannot have lost $H_2O$ by intracrystalline H diffusion, as their $\delta D$ values are the same as those of all other MIs (Fig. 10). We infer that these melts were volatile-undersaturated up to about 1 wt % $K_2O$.

On the plot of $CO_2$ vs $H_2O$ (Fig. 7b), the subvertical trend defined by series M10 Y/B6 can be modelled by open-system degassing from a melt with 2–3 wt % $H_2O$ and $\geq$1200 ppm $CO_2$ (we have assumed $\sim$2000 ppm). Two MIs of series M10 FS3 also have elevated $CO_2$, and define a similarly steep trend. However, volatile undersaturation of M10 FS3 MIs with $<1$ wt % $K_2O$ would rule out degassing. One possibility is that these steep $CO_2$–$H_2O$ trends are due to mixing of shallow-derived, $CO_2$-poor melt and deeper-derived $CO_2$-rich melt, as observed in other violent strombolian eruptions such as Vesuvius 1944 (Marianelli *et al.*, 1999) and Parícutin 1943–1952 (Pioli *et al.*, 2008). A further possibility is that they are due to the fluxing of $CO_2$ from a deeper, non-degassed magma. Further work is required to understand the behaviour of $CO_2$ in our samples.

Volatile-saturated crystallization of Santorini melts will result in the exsolution of a free vapour phase. The amount of $H_2O$ and $CO_2$ exsolved as a function of residual melt fraction can be crudely estimated using measured $K_2O$, $H_2O$ and $CO_2$ contents of initial and derivative melts. The procedure is described fully in Table 4, in which we estimate the exsolved vapour contents of residual melts of several of the MI suites. It should be noted that, owing to concomitant crustal assimilation, $K_2O$ contents at Santorini underestimate F by 15–20% (Druitt *et al.*, 1999), so that the values of F are probably slightly too low. The results in Table 4 show that, were crystal fractionation and vapour exsolution to take place under perfectly closed conditions, the $H_2O + CO_2$ bubble fractions at 100–200 MPa storage pressures would be 50–90 vol. % in andesitic residual melt and $>$90 vol. % in dacitic–rhyodacitic residual melt. Of course, retention of such large volume fractions of gas would not be possible. Escape of vapour from residual melt would be inevitable above the bubble percolation threshold of $>$30 vol. % (Rust & Cashman, 2011), thereby limiting melt bubble contents to less than this value. Moreover, buoyancy-driven melt–vapour segregation would also take place, particularly in mafic, less viscous, melts. Crystallization in the shallow crust must take place under essentially open-system conditions, with the vapour leaving the melt and either reacting with surrounding rocks, segregating into subsurface gas pockets, and/or escaping to the surface. This is consistent with the data trend for MI series M10 Y/B6 in Fig. 7b.

The observed variations of S and Cl are also consistent with MI entrapment under open-system, volatile-saturated conditions. S decreases markedly with fractionation whereas Cl increases. Mafic to intermediate MIs from some units (e.g. M7c and M8-MSF) form flat-lying arrays on the Cl–$K_2O$ plot, in a manner similar to $H_2O$ (Fig. 6b). The only S-bearing crystalline phase in Santorini magmas is pyrrhotite, which occurs very sparingly in magmas of all compositions. However, although the S content of this phase is 37 wt % (Gertisser *et al.*, 2009), its abundance in the bulk crystal assemblage ($\ll$0·1 vol %, equivalent to $\ll$370 ppm bulk S) is far too low to drive down S along the observed liquid line of descent. Similarly, apatite, which contains 0·3–1 wt % Cl (Cadoux *et al.*, 2015), is far too sparse in the bulk mineral assemblage ($<$0·1 vol %, equivalent to $<$10 ppm bulk Cl) to explain the observed Cl liquid line of descent. The variations of S and Cl must therefore be largely controlled by extraction of S and Cl by a free vapour phase, and the removal of that vapour by bubble transfer. The possibility of a free S–Cl-bearing vapour phase has been raised in previous studies of Santorini MIs (Michaud *et al.*, 2000; Gertisser *et al.*, 2009).

Evolution of S and Cl during open-system, volatile-saturated crystallization can be modelled by a modified Rayleigh distillation law (Villemant *et al.*, 2008). In such a system there is competition between crystallization,

**Table 4:** Volatile-saturated crystallization of selected melt inclusion suites

| | $[SiO_2]_i$ (wt %) | $[K_2O]_i$ (wt %) | $[H_2O]_i$ (wt %) | $[CO_2]_i$ (ppm) | $[SiO_2]_f$ (wt %) | $[K_2O]_f$ (wt %) | $[H_2O]_f$ (wt %) | $[CO_2]_f$ (ppm) | $T$ (°C) | $1-F$ | $X$ (200 MPa) | $X$ (100 MPa) | $k$ | $D'$ S | $D$ S | $D'$ Cl | $D$ Cl |
|---|---|---|---|---|---|---|---|---|---|---|---|---|---|---|---|---|---|
| M6c-a | 51·6 | 0·5 | 2·6 | 162 | 68·4 | 3·1 | 3·2 | 122 | 951 | 0·84 | 90 | 95 | 39 | — | — | 0·3 | 12 |
| M7c-a | 50·2 | 0·2 | 2·5 | 180 | 66·6 | 2·9 | 3·5 | 135 | 978 | 0·94 | 97 | 98 | 41 | 1·6 | 66 | 0·9 | 37 |
| M10 6Y/B | 52·7 | 0·5 | 3·1 | 800 | 54·5 | 0·8 | 2·5 | 80 | 1095 | 0·38 | 67 | 80 | 23 | 5 | 120 | 0·6 | 14 |
| M10 FS3 (<1% $K_2O$) | 53·0 | 0·4 | 1·2 | 199 | 55·9 | 0·9 | 3·2 | 157 | 1103 | 0·51 | 0 | 0 | ∞ | 0 | 0 | 0 | 0 |
| M10 FS3 (>1% $K_2O$) | 55·9 | 0·9 | 3·2 | 157 | 57·5 | 1·3 | 3·2 | 270 | 1064 | 0·28 | 50 | 66 | 31 | 1·4 | 45 | 1 | 32 |
| M12 | 50·7 | 0·5 | 3·1 | 193 | 57·3 | 1·3 | 3·3 | 253 | 1065 | 0·62 | 79 | 89 | 33 | 1·5 | 52 | 0·9 | 31 |
| MP | 52·0 | 0·5 | 4·1 | 150 | 68·8 | 3·1 | 5·0 | 78 | 897 | 0·84 | 93 | 97 | 25 | 2·2 | 58 | 0·5 | 13 |

Volatile-saturated fractional crystallization transforms a unit mass of melt into a mixture of residual melt (mass fraction $n_m$), solid ($n_s$) and vapour ($n_v$), such that $n_m + n_s + n_v = 1$. The mass fraction of residual melt is $F = n_m$, and the ratio of solid to vapour is $k = n_s/n_v$. The table gives the initial (i) and final (f) dissolved concentrations of $SiO_2$, $K_2O$, $H_2O$ and $CO_2$ observed in several series of melt inclusions assumed to be related by fractional crystallization. Species concentrations are denoted in square brackets. In all cases, except those inclusions of the M10 FS3 series with < 1 wt % $K_2O$, fractional crystallization took place under vapour-saturated conditions, as described in the text. $F$ for each series is calculated using the initial and final $K_2O$ contents of the melt, $F = [K_2O]_i/[K_2O]_f$. The mass fraction of $H_2O + CO_2$ vapour exsolved between the initial and final states is $n_v = [H_2O + CO_2]_i - F[H_2O + CO_2]_f$. The ratio of solid to vapour is then given by $k = (1 - F - n_v)/n_v$. The volume fraction of exsolved vapour within the residual melt is given by $X_v = (n_{H2O}/\rho_{H2O} + n_{CO2}/\rho_{C02})/(n_m/\rho_m + n_{H2O}/\rho_{H2O} + n_{CO2}/\rho_{C02})$, where the vapour densities $\rho_{H2O}$ and $\rho_{CO2}$ are calculated using the ideal gas law. It should be noted that, owing to concomitant crustal assimilation, $K_2O$ contents at Santorini underestimate $F$ by 15–20% (Druitt *et al.*, 1999). $D'$ is an apparent (crystallization-modified) distribution coefficient for S and Cl and is modelled on Fig. 6; $D$ is the real distribution coefficient, given by $D = D'/(k+1)$ (Villemant *et al.*, 2008).

which causes enrichment in S and Cl, and degassing, which causes depletion. If $D_i = C_i^v/C_i^m$ is the vapour (v)–melt (m) distribution coefficient of volatile species $i$ of concentration $C_i$, then the Rayleigh equation for the system is $C_i^m = C_{i,0}^m F^{(D' - 1)}$, where $D'$ is an apparent distribution coefficient modified by concomitant crystallization. If $k$ is the ratio of mass of crystals to mass of exsolved vapour, then the apparent distribution coefficient $D'$ is given by $D' = D/(k+1)$ (Villemant *et al.*, 2008). In Fig. 6a and b we have modelled S and Cl for the different MIs lineages (see figure legend for details). Evolution from basaltic to andesitic compositions can be successfully modelled using $D'$ values of 1·4–5·0 for S and 0·3–1·0 for Cl. These can be converted to real $D$ values using estimates of $k$ from Table 4. The resulting values of $D$ (45–120 for S; 12–37 for Cl) are in the range of experimentally measured values for basaltic to andesitic melts (e.g. Scaillet & Pichavant, 2005; Witham *et al.*, 2012). The success of these models for the evolution of andesite to rhyodacite is less clear. For S, a constant value of $D'$ describes the observed variations across the entire compositional spectrum, from basalt to rhyolite. For Cl, however, dacitic to rhyodacitic melts may be too Cl-rich to be successfully modelled in such a simple manner. For example, whereas the models for Middle Pumice and for M6c–M6a reproduce the most silicic MIs, that for series M7c–M7a does not. More rigorous modelling of Cl variations from intermediate to silicic compositions may need to take into account (1) variations of $D_{Cl}$ with melt and/or vapour composition, and/or (2) enrichment of silicic melts in Cl by processes other than fractional crystallization (e.g. incorporation of seawater; Wallace, 2005).

S and Cl in melt inclusions of sample M10 FS3 containing <1 wt % $K_2O$ both behave incompatibly ($D' = D = 0$; Table 4), reinforcing the interpretation that these melts were volatile-undersaturated.

We conclude that most Santorini melts ranging from basaltic to rhyolitic in composition coexisted with a free COHSCl vapour phase at the time of MI entrapment. Typical basaltic melts at Santorini contained up to 2–4 wt % $H_2O$, at least 1200 ppm $CO_2$, 1200 ppm S, 500 ppm Cl and 100 ppm F (Figs 6 and 7); this is consistent with recent phase equilibria studies that inferred 3–5 wt % $H_2O$ for the ~340 ka Balos basalt (Andújar *et al.*, 2015). Some basaltic melts with lower $H_2O$ contents (1–2 wt %) appear to have been volatile-undersaturated.

## Presence of a hypersaline phase in silicic melts

By comparing the experimental solubility relationships for Cl-bearing silicic melts with their MI data, Cadoux *et al.* (2014) postulated that some Santorini silicic melts are saturated not only with an $H_2O$-rich vapour, but probably also with a hydrosaline liquid (brine). Our extended dataset now allows us to address this same question for the entire range of melt compositions at the volcano.

The solubility behaviour of $H_2O$–Cl-bearing silicate melts has been reviewed by Webster (2004). In a volatile-saturated system, exsolution of a vapour phase is favoured at low $Cl/H_2O$ melt ratios, whereas higher ratios favour exsolution of a Cl-rich hydrosaline liquid (brine). The critical $Cl/H_2O$ ratios have been determined experimentally at 200 MPa for melts of a wide range of compositions, including basaltic (critical $Cl/H_2O$ ratio 0·55), andesitic and latitic (0·35), and rhyolitic (topaz-bearing rhyolite and haplogranite) (0·05). The solubility data of Botcharnikov *et al.* (2004) constrain the critical ratio for rhyodacitic melt to be at least 0·13. The critical ratios increase with decreasing pressure. In Fig. 9 the

Cl/$H_2O$ ratios of our MIs are compared with these published values. The mafic melts, and most silicic melts, fall beneath the brine saturation field at 200 MPa. It should be noted that decreasing the pressure to <200 MPa would raise the limit of brine saturation, and so reinforce this conclusion. However, the rhyolitic melts of the Minoan eruption lie at the limit of brine saturation at 200 MPa. This supports the conclusion of Cadoux *et al.* (2015) that the Minoan eruption may have discharged a melt containing a $H_2O$–Cl-rich liquid phase, as well as a vapour phase. Melts of the present-day Kameni magmas appear not to be saturated in brine at ≤200 MPa.

## MAGMA STORAGE AND EXTRACTION

Based on (1) the isolated, leakage-free nature of the MIs, (2) the absence of evidence for syn-eruptive or post-eruptive loss of $H_2O$ or $CO_2$, and (3) the evidence for vapour saturation (with the exception of the least evolved MIs of M10 FS3), saturation pressures from MI $H_2O + CO_2$ contents can be recalculated as depths assuming a lithostatic stress field and a geophysically determined mean density of the upper crust (~2640 kg $m^{-3}$; Konstantinou, 2010) (Fig. 12a). The lithostatic assumption is justified because non-lithostatic stress components in the upper crust, as reflected in earthquake stress releases, are typically a few MPa (Oth, 2013), and magma excess pressures necessary for reservoir fracturing and dyke propagation to the surface do not exceed ~10 MPa (Gudmundsson, 2012). Both contributions are comparable in magnitude with the error on our pressure estimates (±10 MPa; ±0·4 km), and can be neglected.

All of our MIs record entrapment in the topmost 10 km or so of the crust (Fig. 12a). There are two possible explanations for this (Plank *et al.*, 2013). One is that Santorini melts become volatile saturated at depths of <10 km, so that ascent under undersaturated conditions from deeper levels leads to resorption of any existing crystals, and only crystals and MIs formed at <10 km are preserved. The other is that crystal growth occurs throughout the crust, but that deep-derived crystals remain long enough above ~10 km for volatiles and H isotopes in early formed MIs to re-equilibrate. Crystal growth and MI entrapment in the upper ~10 km is envisaged to be driven by a combination of volatile-saturated decompression and cooling as melts rise through progressively lower-pressure and cooler environments.

We interpret the observed range of MI entrapment depths for each eruption (Fig. 12a) in the following way. The deepest observed depth corresponds either to the onset of volatile-saturated crystal growth or to the last level of MI re-equilibration. This is, of course, a minimum estimate owing to possible sampling bias. The shallowest depth corresponds to that at which the ascending magma last paused prior to rapid final ascent and eruption (Fig. 12b).

### Plinian eruptions

Depths given by the four large silicic plinian eruptions (Lower Pumice 1, Lower Pumice 2, Cape Riva, Minoan) are all ≥4 km (≥100 MPa), and span a range of values. They include the best-estimate pre-eruptive depth of ~8 km (~200 MPa) for these same four eruptions based on phase equilibria experiments (Cadoux *et al.*, 2014) (Table 1), but extend to lower and higher values. The lower values are interpreted to be real, because of our rigorous MI textural selection criteria. If we include the MIs from Cadoux *et al.* (2014), as described above, then MIs from the two Lower Pumice eruptions of cycle 1 yield 4·8–8·9 km (125–230 MPa), Cape Riva 3·9–10·4 km (100–270 MPa), and the Minoan 4·2–12·3 km (100–320 MPa), all using the Papale *et al.* (2006) solubility law. Pressures or depths from MIs in Lower Pumice 2 (150–180 MPa; 5·8–6·9 km) are significantly lower than those calculated from Al-in-hornblende barometry (Gertisser *et al.*, 2009; Table 1), as also observed by Cadoux *et al.* (2014). Use of VolatileCalc in the Minoan case (the only truly rhyolitic MIs) yields depths up to 9·6 km (250 MPa), lower than Papale. MIs from a high-Ba microphenocryst-rich andesitic pumice from the Minoan (Druitt *et al.*, 2014) yield a depth range similar to that of MIs in the main, rhyodacitic pumice. A silicic MI from the Middle Pumice eruption gives 6·0 km (155 MPa), and two associated mafic MIs from inmixed, basalt-derived olivines in the same pumices give ~4–8 km (100–200 MPa), depending on the solubility law used. Only MIs of the Vourvoulos eruption, the smallest plinian event recognized by Druitt *et al.* (1999), yield depths of less than ~4 km. It should be recalled that pressures and depths based on $H_2O + CO_2$ solubility may be underestimated by up to 10–20% in the most Cl-rich of silicic MIs.

Our MIs from the four main plinian units therefore record MI entrapment over large pressure intervals ($\Delta P$, up to 220 MPa). This has also been reported from large silicic eruptions at other volcanoes. For example, the 760 ka, >600 $km^3$ Bishop Tuff eruption sampled melts trapped over a pressure interval of $\Delta P \approx 160$ MPa, the 26·5 ka, ~530 $km^3$ Oruanui eruption over $\Delta P \approx 100$ MPa, and the 160 ka, >60 $km^3$ Kos Plateau Tuff eruption over $\Delta P \approx 100$ MPa (Wallace *et al.*, 1995; Liu *et al.*, 2005; Bachmann *et al.*, 2009). There are two possible interpretations for this. Either (1) magmas were extracted simultaneously during eruption from a wide range of storage pressures, or (2) some of the magma was transferred from deep to shallow levels shortly prior to eruption, with some of the MIs retaining a memory of higher pressures.

### Constraints from the Minoan eruption

Constraints on these explanations are provided by the Minoan eruption, for which we have analysed the most MIs from a single unit, and for which we have an approximate dense-rock equivalent (DRE) volume estimate (30–80 $km^3$; Pyle, 1990; Sigurdsson *et al.*, 1990; Johnston *et al.*, 2014). It should be recalled that all but

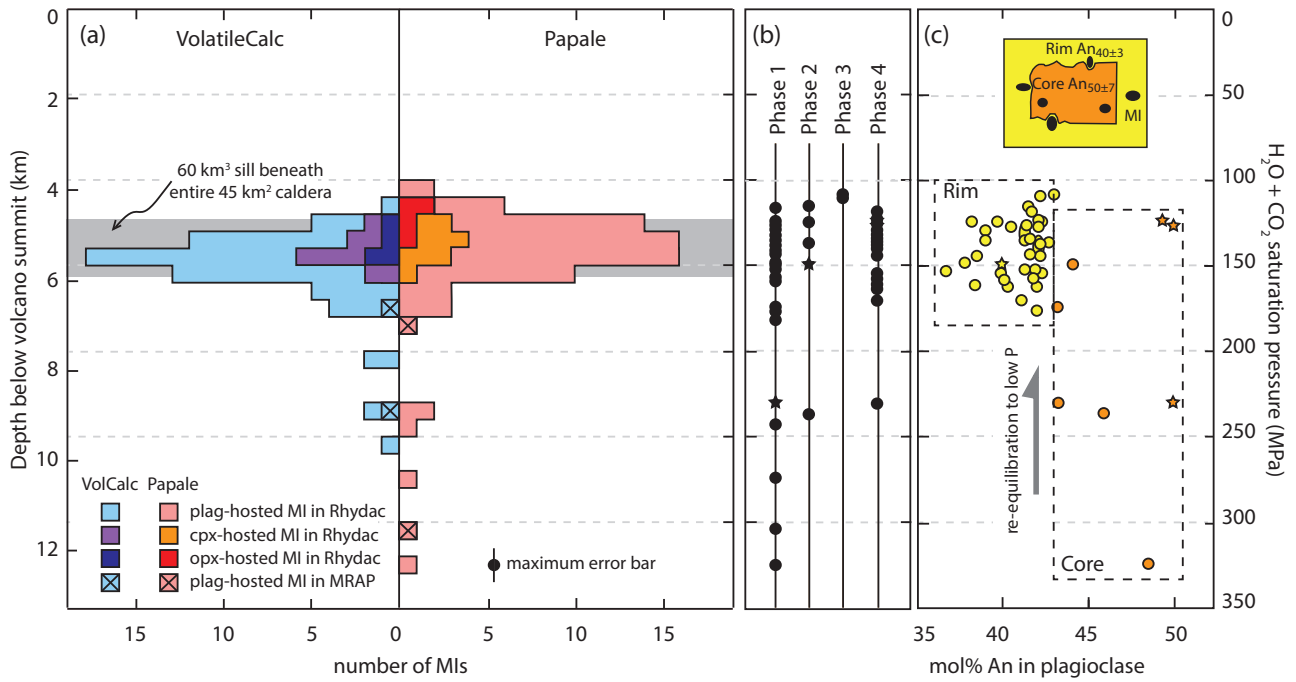


**Fig. 13.** (a) Histograms of $H_2O + CO_2$ saturation pressures calculated using melt inclusions from the Minoan eruption. All but two of the MI come from the main Minoan rhyodacitic pumice; the other two are from a minor andesitic component (MRAP, microphenocryst-rich andesitic pumice; Druitt, 2014). The pressures are recalculated using two solubility models relevant to silicic melts: VolatileCalc (Newman & Lowenstern, 2002) and the model of Papale *et al.* (2006). (b) Distribution of MI saturation pressures between the eruptive phases. (c) Plot of saturation pressure vs An content of the host plagioclase, distinguishing MIs in the cores of the plagioclase phenocrysts from those in the rims. The stars are data from Cadoux *et al.* (2014), which are comparable with those of this study.

two of our Minoan MIs come from the main (≫99%), rhyodacitic magmatic component of the eruption (Druitt, 2014). The MI-derived pressure–depth data are plotted in Fig. 13, from which we make the following observations. First, the majority of plagioclase-hosted MIs, and all pyroxene-hosted MIs, derive from an upper layer no more than 2 km thick (from 4 to 6 km depth), with a 'tail' of plagioclase-hosted MIs recording depths between 6 and 10–12 km. Two MIs from the volumetrically minor andesitic component also record depths beneath the main layer. Second, the entire range of depths is recorded in MIs from eruptive phase 1, as well as (to varying degrees) in those from subsequent phases (Fig. 13b).

If the whole depth interval records purely syn-eruptive extraction, then the Minoan reservoir must either have had the form of an upward-flaring funnel, with a wide top at 4–6 km and a narrow root extending to 10–12 km, or the magma must have been stored as a plexus of interconnected melt lenses within a mush body several kilometres thick (e.g. Cashman & Giordano, 2014). In either of these cases, the early erupted magma (phase 1) would be expected to have come from the shallowest levels, and the last-erupted magma (phase 4) from the deepest levels. However, the entire depth range is recorded in MIs from the first phase, which is not consistent with top-down extraction.

Cottrell *et al.* (1999) used phase equilibria constraints to argue for late-stage ascent of Minoan melt from deeper to shallower crustal levels. Plagioclase crystals in the magma have cores of $An_{50\pm7}$ mantled by rims of $An_{40\pm3}$ (Cottrell *et al.*, 1999; Druitt *et al.*, 2012). Cottrell *et al.* measured MI $H_2O$ contents of 3·5–6·2 wt % in the cores, and inferred (but did not measure) 2·5–3·0 wt % in the rims. Our new dataset now includes many MIs from plagioclase rims, and these contain 4·0–5·0 wt % $H_2O$ (Fig. 13c). They are contained within deep resorption embayments in the cores and surrounded by thin shells of rim plagioclase, visible only on high-resolution BSE images. MIs in the cores have higher contents of $H_2O$ (4·6–6·9 wt %; Fig. 13c). The data therefore support the hypothesis of Cottrell *et al*, but refine the source depths.

We infer that the plagioclase cores derive from at least 10–12 km depth, and were transported by ascending silicic melt to a shallow magma chamber (4–6 km) where they were overgrown by the rims. Some core MIs with lower $H_2O$ probably partly re-equilibrated upon arriving in the chamber. MIs in opx and cpx were either trapped by pyroxene growth in the chamber, or were carried from depth and re-equilibrated upon arrival.

Druitt *et al.* (2012) used Mg-in-plagioclase diffusion chronometry to show that this last event of melt (plus plagioclase cores) transfer from depth occurred within a few decades to a few months of the eruption. Whereas Cottrell *et al.* (1999) interpreted it as involving the entire Minoan magma volume, Druitt *et al.* (2012) argued that it may have involved only the most recent batch of a series of deeper inputs during prolonged assembly of the shallow chamber.

This interpretation may explain two other features of the Minoan eruption. First, the rhyodacitic magma is extremely homogeneous, both compositionally and thermally (Fe–Ti oxide temperatures), irrespective of eruptive phase, which implies a late-stage homogenization event (Druitt *et al.*, 2012; Druitt, 2014). Second, the full range of MI entrapment depths from 4 to 10–12 km is recorded by MIs of the first eruptive phase. Because Santorini melts are volatile-saturated at shallow crustal pressures, ascent of silicic melt from 10–12 km to 4–6 km might have resulted in vesiculation. A simple calculation based on the exsolution of 2 wt % $H_2O$ (from 6·5 to 4·5 wt %), a final storage pressure of 130 MPa and the ideal gas law suggests that the melt could have arrived in the shallow chamber with ~20 vol. % more bubbles than it started with. This bubbly melt might then have risen buoyantly as a plume to the top of the chamber, causing (1) mixing and homogenization of the chamber contents prior to eruption, and (2) extraction of both deep-derived and shallow-derived MIs during the first eruptive phase.

The MI data, combined with the compositional and thermal homogeneity of the Minoan rhyodacite, show that the magma was stored immediately prior to eruption in a single, sill-shaped chamber <2 km thick, the top of which was situated ~4 km beneath the volcano. Assuming that the chamber underlay the entire 45 $km^2$ caldera (Johnston *et al.*, 2014), then the DRE volume of the eruption of 30–80 $km^3$ gives caldera collapse heights from 0·7 to 1·8 km, suggesting that much, if not all, of the chamber was extracted during the eruption.

## Interplinian eruptions

### *The cycle 2 interplinian eruptions*

MI entrapment depths for the cycle 2 interplinian mafic magmas (excluding those of the volatile-undersaturated MIs of M10 FS3, for which total pressures cannot be calculated) range from 1 to 10 km (<50 to 250 MPa) (Fig. 12). This shows that, although these magmas saturated as deep as 10 km, they stalled at very high crustal levels (1–3 km) prior to final ascent and eruption.

Three silicic interplinian eruptions of cycle 2 give saturation depths of ~4 km, and pre-eruptive storage depths of 2–3 km (50–100 MPa), both much shallower than the corresponding depths for plinian eruptions of the same cycle [the Vourvoulos eruption, one of the smallest of the plinian eruptions identified by Druitt *et al.* (1999), plots with the interplinians]. The differences could be an artefact due to the extra lithostatic load exerted by intracaldera edifices. Intracaldera edifices grow progressively during interplinian periods, are highest prior to plinian eruptions, and are destroyed by caldera collapse prior to the onset of the subsequent interplinian. Associated height changes can reach ~750 m, from edifices up to 350 m above sea level (e.g. 67–54 ka Skaros edifice) to caldera floors 300–400 m below sea level (e.g. present-day caldera), corresponding to changes in lithostatic loading of ±9 MPa (Fig. 12a). Given that lithostatic pressure is measured from the top of the volcano, storage pressures during interplinian periods (deep caldera and small intracaldera edifices) might be expected to be slightly lower than those prior to plinian eruptions (high edifices partly or entirely filling calderas) for a given chamber depth below a fixed surface datum (e.g. present-day sea level). However, this ±9 MPa lithostatic effect does not seem to be able to account for the observed differences (Fig. 12a). We therefore conclude that the differences between pre-plinian and interplinian depths are real.

One possible explanation is that the cycle 2 interplinian silicic melts had inherently lower $H_2O$ contents than the plinian silicic melts, allowing them to ascend higher in the crust before reaching saturation. Another possibility relates to the existence of surface edifices. In addition to increasing vertical stresses in the shallow crust, pre-plinian edifices can increase horizontal compressive stresses, thereby inhibiting dyke ascent (Pinel & Jaupart, 2003). This effect might cause ascending silicic melts to pond deeper prior to plinian eruptions than during the interplinian periods that follow caldera collapse and consequent release of the edifice-generated horizontal stresses.

### *The (cycle 3) AD 726 Kameni eruption*

Melt inclusions from the AD 726 explosive eruption of Kameni Volcano imply a saturation depth of at least ~6 km and pre-eruptive storage depth of ~4 km (Fig. 12a), which is in good agreement with the storage depth estimation of Barton & Huijsmans (1986) using clinopyroxene–plagioclase equilibria for Kameni magmas in general (Table 1). The eruption was of much smaller magnitude than the interplinian eruptions of cycle 2 sampled in this study, because its fallout is not observed outside the caldera. The AD 726 magma was stored deeper than those of the cycle 2 interplinian silicic eruptions, near the top of the (presumably now largely crystallized) Minoan chamber. However, Kameni magma is not residual Minoan magma, because it is lower in incompatible trace elements and represents a new batch from depth following the Minoan eruption (Huijsmans *et al.*, 1988). One possibility is that the Minoan eruption, one of Santorini's largest, resulted in (or was triggered by) modifications of the stress field beneath the volcano that were large enough to cause a change in the ponding level of silicic magma during the subsequent and current interplinian period.

We note that the AD 726 storage depth (~4 km) is similar to depths of Mogi pressure sources calculated for surface uplift of the 2011–2012 unrest period: ~4 km [global positioning system (GPS) data; Newman *et al.*, 2012], 4·4 +1·1/–1·0 km [InSAR (interferometric synthetic aperture radar) data; Parks *et al.*, 2012], 3·3 km (GPS data; Papoutsis *et al.*, 2012), 6·5 km (InSAR data; Papoutsis *et al.*, 2012) and 3·5–3·8 km (joint GPS and InSAR data; Foumelis *et al.*, 2013). This reinforces published evidence that the uplift in 2011–2012 was due to shallow magmatic intrusion (Parks *et al.*, 2012, 2015; Rizzo *et al.*, 2015).

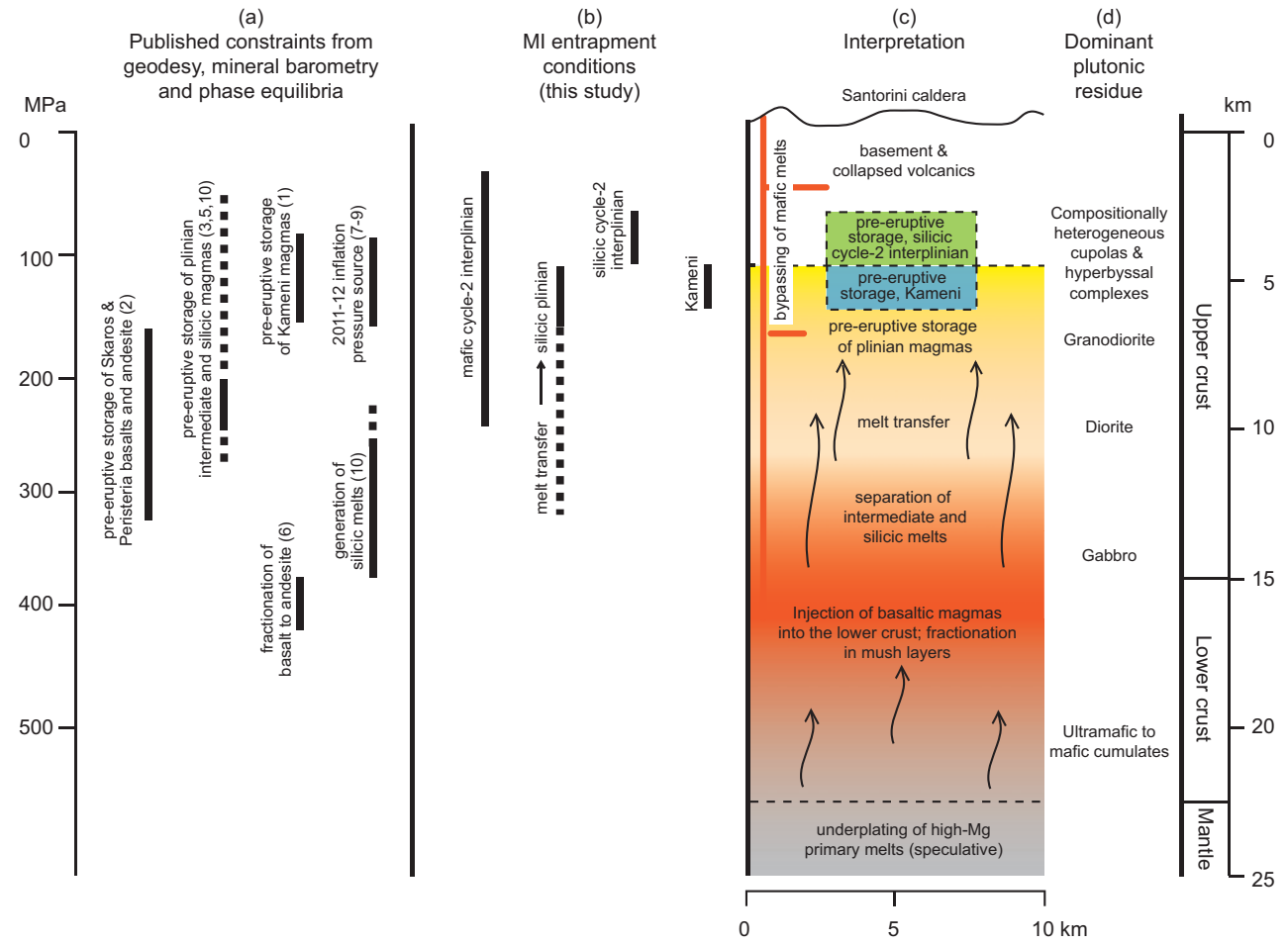


**Fig. 14.** Constraints on magma pressures–depths from (a) previously published studies (numbers are references in Table 1) and (b) the melt inclusion entrapment data from this study. The constraints are combined in the form of (c) a schematic model of the Santorini plumbing system. (d) Lithologies inferred to form the present-day plutonic complex beneath the caldera.

## PLUMBING SYSTEM ARCHITECTURE AT SANTORINI

Our results, combined with those of other recent studies, allow us to place quantitative constraints on the depths of magma storage and extraction beneath Santorini. They are presented in the form of a one-dimensional, time-integrated petrological image of the plumbing system (Fig. 14).

The present-day crustal column beneath the caldera is the product of more than half a million years of magmatism. Druitt *et al.* (1999) estimated that 300–600 $km^3$ of magma has passed through the crust beneath the caldera, implying that much of the 25 km thick crust has been replaced by variably solid to mushy plutonic residues. We envisage a crustal magmatic system similar to that postulated by Annen *et al.* (2006). The system is driven by repeated underplating and injection of the lower crust by basalt, which fractionates in ultramafic to gabbroic mush bodies to more evolved residual melts, accompanied by crustal assimilation. Gravitational compaction of crystal mush layers expels residual melts, which ascend by porous flow to higher structural levels. Percolating melts equilibrate chemically with progressively cooler host environments, leading to continued fractionation and production of more evolved compositions until the melts segregate into dykes and ascend too rapidly for equilibrium to be maintained (Solano *et al.*, 2012). These melts inject into the upper crust, where they either accumulate as eruptible lenses or crystallize as plutons (Annen, 2009; Gelman *et al.*, 2013; Menand *et al.*, 2015).

Primary mantle-derived melts at Santorini have up to 9–12 wt % MgO (Nichols, 1978), at least several wt % $H_2O$ (Andújar *et al.*, 2015; this study), and a range of trace element and isotopic signatures owing to varying degrees of contamination by subduction fluids and sediment-derived melts (Huijsmans *et al.*, 1988; Francalanci *et al.*, 2005; Bailey *et al.*, 2009; Vaggelli *et al.*, 2009). Fractionation of these primary melts generates residual melts ranging from basaltic through intermediate to silicic. Three lines of evidence place constraints on the levels at which residual melts separate from their parent mushes. First, typical andesitic melts can be explained as residual melts produced by fractionation of basalt with ~50 wt % $SiO_2$ and 4–6 wt % $H_2O$ near the base of the upper crust (~15 km;

~400 MPa) (Andújar *et al.*, 2015). Second, silicic melts can be explained by fractionation of andesite in the 8–15 km depth range (200–400 MPa; Andujar *et al.*, in preparation). Third, melt inclusions from the cores of plagioclase crystals in Minoan pumices record ascent of silicic melt batches from depths as great as 10–12 km (present study). These observations suggest that intermediate to silicic melts separate from their parent mushes in the depth interval from 8 to ≥15 km, then rise rapidly through the upper crust. Nodules of gabbro and diorite brought to the surface by erupting magmas may be samples of cumulates from which evolved interstitial melts have been removed (Druitt *et al.*, 1999). Most residual melts travel through the upper <10 km of the crust volatile-saturated (Fig. 12), resulting in crystal growth, MI entrapment, vesiculation and outgassing.

During the repose periods that precede plinian eruptions basalt accumulates at depth, generating large volumes of evolved melts by fractional crystallization, crustal assimilation, and defrosting of extant, mushy plutons. Successive melt batches then ascend, via a series of high-flux transfer events, into the upper crust on geologically short timescales (Druitt *et al.*, 2012; Fabbro *et al.*, 2013), where they amalgamate to form sill-shaped reservoirs of crystal-poor magma in the 4–8 km depth range, perhaps under the influence of horizontal stresses induced by intracaldera edifices. The origin of these melt transfer events is not understood, but they may result from high, transient mantle input rates (Fabbro *et al.*, 2013), tectonic forcings (Feuillet, 2013), or spontaneous, gravitationally driven reorganizations of mush layers (Christopher *et al.*, 2015). The magma chamber of the 30–80 $km^3$ Minoan eruption was a single lens of well-stirred melt, between 0·7 and 2 km in thickness (Fig. 13), that had a late-stage growth spurt within a decade of its eruption (Druitt *et al.*, 2012). The >10 $km^3$ magma reservoir of the 22 ka Cape Riva plinian eruption was situated in a similar depth range (Fig. 12), and was assembled in less than ~3000 years (Fabbro *et al.*, 2013). Caldera collapse during plinian eruptions probably empties most of these magma layers, any residue then crystallizing following eruption-induced decompression.

During interplinian periods of cycle 2, evolved melts accumulated pre-eruptively in small, superficial (1–3 km deep) reservoirs above the main plinian storage levels, perhaps in compositionally heterogeneous cupolas and hyperbyssal complexes. The AD 726 eruption of Kameni Volcano was fed from a small body of dacitic magma situated near the top of the largely crystallized remains of the Minoan magma chamber.

## CONCLUSIONS

We have analysed the $H_2O$ contents of 138 plagioclase-, olivine- and pyroxene-hosted melt inclusions (MIs), along with $CO_2$, S, Cl, F and δD in various subsets, from eruptions of the last 200 kyr at Santorini caldera. The aim was to constrain magma storage/extraction depths associated with plinian eruptions, as well as those associated with smaller eruptions that characterize interplinian periods. The sampling focused mainly on the products of explosive cycle 2. The main conclusions are as follows.

1. Mafic MIs contain 1–4 wt % $H_2O$ and up to 1200 ppm $CO_2$; silicic MIs contain 2–7 wt % $H_2O$ and up to 150 ppm $CO_2$. The high Cl contents (<6000 ppm) and low to moderate S contents (<1500 ppm) of the MIs relative to arc magmas elsewhere are in agreement with the findings of previous studies.
2. The MIs selected for analysis were isolated in olivine, plagioclase or pyroxene phenocrysts, with no textural evidence for leakage. A subset of 27 MIs in olivine and plagioclase has δD values ranging from –37 to –104‰, encompassing mantle to slab values, with no evidence for $H_2O$ loss from olivine-hosted MIs by hydrogen diffusion. There is no systematic difference in $CO_2$ contents between bubble-bearing MIs and bubble-free MIs within given units, suggesting little sequestration of $CO_2$ into bubbles. Raman analysis of selected MIs also revealed no detectable $CO_2$ in bubbles.
3. Santorini parental basalts contain 2–4 wt % $H_2O$, ≥1200 ppm $CO_2$, 1200 ppm S, 500 ppm Cl and 100 ppm F. Most MIs, from mafic to silicic, were saturated with a free COHSCl vapour phase at upper crustal pressures, as shown by the compatible behaviours of $H_2O$, S and Cl in melt inclusions suites. However, some basaltic MIs have lower $H_2O$ contents (1–2 wt %), and may have been volatile-undersaturated when trapped. The Minoan magma probably contained an $H_2O$–Cl-rich hypersaline liquid phase.
4. The leak-free nature of the MIs and the evidence for volatile saturation allow calculation of $H_2O + CO_2$ saturation pressures using suitably calibrated solubility models, and conversion to depths using a geophysically determined mean density for the upper crust. Saturation pressures of some particularly Cl-rich MIs may be underestimated by 10–20%. Most MIs record entrapment at depths of <10 km, and so provide no information on processes at greater depths.
5. Melt inclusions from plinian eruptions record melt extraction from >100 MPa (>4 km), and over depth intervals of several kilometres. A large dataset of MIs from the rhyodacitic magma of the Minoan eruption shows that MIs trapped in cpx, opx, and the $An_{40\pm3}$ rims of plagioclases record pre-eruptive storage within an upper crustal magma layer ≤2 km in thickness, from 100 to 160 MPa (4–6 km depth). MIs in the $An_{50\pm7}$ plagioclase cores, however, record storage at higher pressures, up to 320 MPa (10–12 km). The large depth range recorded by MIs in the Minoan eruption is attributed to late-stage transfer of silicic melt (+ antecrystic plagioclase cores) from the middle crust to a shallow magma chamber, from which the magma was finally erupted. This late-stage replenishment event has been previously constrained by diffusion chronometry as having taken

place less than about ~10 years prior to the eruption. The plagioclase cores were carried from depth in the ascending melt, then overgrown by the rims in the shallow chamber.

6. The Minoan silicic melt may have vesiculated while decompressing from 320 to 100–160 MPa. Injection into the shallow chamber as a buoyant, bubbly plume may have caused mixing and homogenization, explaining (a) the compositional and thermal homogeneity of the Minoan magma, and (b) the wide range of pressures recorded by MIs in plagioclases of the first eruptive phase.
7. Silicic magmas of cycle 2 interplinian periods were stored pre-eruptively in reservoirs situated above the pre-plinian storage levels, possibly in cupolas and hyperbyssal complexes.
8. The depth of the small magma body that fed the AD 726 eruption of Kameni Volcano (~4 km) was similar to those estimated for the pressure source during the 2011–2012 unrest period, lending support to a magmatic origin for the unrest. It lay near the top of the largely crystallized remains of the Minoan magma chamber.
9. Mantle-derived basalt injects into the lower crust below Santorini, where it fractionates in bodies of hot crystal mush. Residual melts of intermediate to silicic composition separate from their parent mushes in the 8 to >15 km depth interval, then ascend through the upper crust, where they either crystallize or accumulate in reservoirs of eruptible, crystal-poor magma. Most residual melts travel through the upper ~10 km of the crust volatile-saturated, leading to crystal growth, MI entrapment, vesiculation and outgassing.

## ACKNOWLEDGEMENTS

We thank Jean-Luc Devidal and Jean-Marc Hénot for their expertise in electron microprobe analysis and electron microscope imagery, respectively. Estelle Koga gave us valuable advice on sample preparation for SIMS analysis. Pierre Condamine and Didier Laporte advised us during preparation of the andesitic $CO_2$ standards. The paper benefited from very helpful reviews by Kathy Cashman, Ralf Gertisser and Nicole Métrich.

## FUNDING

This research was financed by the French Government Laboratory of Excellence initiative n°ANR-10-LABX-0006, the Région Auvergne and the European Regional Development Fund. This is Laboratory of Excellence ClerVolc contribution number 197.

## SUPPLEMENTARY DATA

Supplementary data for this paper are available at *Journal of Petrology* online.

## REFERENCES

Anderson, A. L. & Brown, G. G. (1993). $CO_2$ contents and formation pressures of some Kilauean melt inclusions. *American Mineralogist* **78**, 794–803.

Anderson, A. T., Jr, Newman, S., Williams, S. N., Druitt, T. H., Skirius, C. & Stolper, E. (1989). $H_2O$, $CO_2$, Cl, and gas in plinian and ash-flow Bishop rhyolite. *Geology* **17**, 221–225.

Anderson, J. L. & Smith, D. (1995). The effects of temperature and $fO_2$ on the Al-in-hornblende barometer. *American Mineralogist* **80**, 549–559.

Andújar, J., Scaillet, B., Pichavant, M. & Druitt, T. H. (2015). Differentiation conditions of a basaltic magma from Santorini and its bearing on basalt–andesite to andesite magma production in arc settings. *Journal of Petrology* **56**, 765–794.

Annen, C. (2009). From plutons to magma chambers: Thermal constraints on the accumulation of eruptible silicic magma in the upper crust. *Earth and Planetary Science Letters* **284**, 409–416.

Annen, C., Blundy, J. D. & Sparks, R.S. J. (2006). The genesis of intermediate and silicic magmas in deep crustal hot zones. *Journal of Petrology* **47**, 505–539.

Arienzo, I., Moretti, R., Civetta, L., Orsi, G. & Papale, P. (2010). The feeding system of Agnano–Monte Spina eruption (Campi Flegrei, Italy): Dragging the past into present activity and future scenarios. *Chemical Geology* **270**, 135–147.

Bachmann, O. & Bergantz, G. (2008). The magma reservoirs that feed supereruptions. *Elements* **4**, 17–21.

Bachmann, O., Wallace, P. J. & Bourquin, J. (2009). The melt inclusion record from the rhyolitic Kos Plateau Tuff (Aegean Arc). *Contributions to Mineralogy and Petrology* **159**, 187–202.

Bailey, J. C., Jensen, E. S., Hansen, A., Kann, A. D. J. & Kann, K. (2009). Formation of heterogeneous magmatic series beneath North Santorini, South Aegean island arc. *Lithos* **110**, 20–36.

Barton, M. & Huijsmans, J. P. P. (1986). Post-caldera dacites from the Santorini volcanic complex, Aegean Sea, Greece: an example of the eruption of lavas of near-constant composition over a 2,200 year period. *Contributions to Mineralogy and Petrology* **94**, 472–495.

Barton, M., Salters, V. J. M. & Huijsmans, J. P.P. (1983). Sr isotope and trace element evidence for the role of continental crust in calc-alkaline volcanism on Santorini and Milos, Aegean Sea, Greece. *Earth and Planetary Science Letters* **63**, 273–291.

Blundy, J., Cashman, K. V. & Berlo, K. (2008). Evolving magma storage conditions beneath Mount St. Helens inferred from chemical variations in melt inclusions from the 1980–1986 and current (2004–2006) eruptions. In: Sherrod, D.R., Scott, W.E. & Stauffer, P.H. (eds) *US Geological Survey*, A Volcano Rekindled: The Renewed Eruption of Mount St. Helens, 2004-2006. **1750**, 755–790.

Botcharnikov, R. E., Behrens, H., Holtz, F., Koepke, J. & Sato, H. (2004). Sulfur and chlorine solubility in Mt. Unzen rhyodacitic melt at 850°C and 200 MPa. *Chemical Geology* **213**, 207–225.

Botcharnikov, R. E., Holtz, F. & Behrens, H. (2007). The effect of $CO_2$ on the solubility of $H_2O$–Cl fluids in andesitic melt. *European Journal of Mineralogy* **19**, 671–680.

Bucholz, C. E., Gaetani, G. A., Behn, M. D. & Shimizu, N. (2013). Post-entrapment modification of volatiles and oxygen fugacity in olivine-hosted melt inclusions. *Earth and Planetary Science Letters* **374**, 145–155.

Cadoux, A., Scaillet, B., Druitt, T. H. & Deloule, E. (2014). Magma storage conditions of large Plinian eruptions of

Santorini Volcano (Greece). *Journal of Petrology* **55**, 1129–1171.

Cadoux, A., Scaillet, B., Bekki, S., Oppenheimer, C. & Druitt, T. H. (2015). Stratospheric ozone destruction by the Bronze-Age Minoan eruption (Santorini Volcano, Greece). *Scientific Reports* **5**, 12243.

Cashman, K. V. & Giordano, G. (2014). Calderas and magma reservoirs. *Journal of Volcanology and Geothermal Research* **288**, 28–45.

Cashman, K. V. & Sparks, R. S. J. (2013). How volcanoes work: A 25 year perspective. *Geological Society of America Bulletin* **125**, 664–690.

Chen, Y., Provost, A., Schiano, P. & Cluzel, N. (2011). The rate of water loss from olivine-hosted melt inclusions. *Contributions to Mineralogy and Petrology* **162**, 625–636.

Chen, Y., Provost, A., Schiano, P. & Cluzel, N. (2013). Magma ascent rate and initial water concentration inferred from diffusive water loss from olivine-hosted melt inclusions. *Contributions to Mineralogy and Petrology* **165**, 525–541.

Chesner, C. A. & Luhr, J. F. (2010). A melt inclusion study of the Toba Tuffs, Sumatra, Indonesia. *Journal of Volcanology and Geothermal Research* **197**, 259–278.

Christopher, T. E., Blundy, J., Cashman, K., Cole, P., Edmonds, M., Smith, P. J., Sparks, R. S. J. & Stinton, A. (2015). Crustal-scale degassing due to magma system destabilization and magma–gas decoupling at Soufrière Hills Volcano, Montserrat. *Geochemistry, Geophysics, Geosystems* **16**, 1–15.

Colucci, S., de' Michieli Vitturi, M., Neri, A. & Palladino, D. M. (2014). An integrated model of magma chamber, conduit and column for the analysis of sustained explosive eruptions. *Earth and Planetary Science Letters* **404**, 98–110.

Cottrell, E., Gardner, J. E. & Rutherford, M. J. (1999). Petrologic and experimental evidence for the movement and heating of the pre-eruptive Minoan rhyodacite (Santorini, Greece). *Contributions to Mineralogy and Petrology* **135**, 315–331.

Danyushevsky, L. V., McNeill, A. W. & Sobolev, A. V. (2002). Experimental and petrological studies of melt inclusions in phenocrysts from mantle-derived magmas: an overview of techniques, advantages and complications. *Chemical Geology* **183**, 5–24.

Davidson, J., Turner, S., Handley, H., Macpherson, C. & Dosseto, A. (2007). Amphibole 'sponge' in arc crust? *Geology* **35**, 787–790.

Dimitriadis, I., Karagianni, E., Panagiotopoulos, D., et al. (2009). Seismicity and active tectonics at Coloumbo Reef (Aegean Sea, Greece): monitoring an active volcano at Santorini Volcanic Center using a temporary seismic network. *Tectonophysics* **465**, 136–149.

Dixon, J. E. (1997). Degassing of alkalic basalts. *American Mineralogist* **82**, 368–378.

Dixon, J. E. & Pan, V. (1995). Determination of the molar absorptivity of dissolved carbonate in basanitic glass. *American Mineralogist* **80**, 1339–1342.

Dixon, J. E., Stolper, E. M. & Holloway, J. R. (1995). An experimental study of water and carbon dioxide solubilities in mid-ocean ridge basaltic liquids. Part I. Calibration and solubility models. *Journal of Petrology* **36**, 1607–1631.

Druitt, T. H. (2014). New insights into the initiation and venting of the Bronze-Age eruption of Santorini (Greece), from component analysis. *Bulletin of Volcanology* **76**, 794.

Druitt, T. H. & Francaviglia, V. (1992). Caldera formation on Santorini and the physiography of the islands in the late Bronze Age. *Bulletin of Volcanology* **54**, 484–493.

Druitt, T. H., Edwards, L., Mellors, R. M., Pyle, D. M., Sparks, R. S. J., Lanphere, M., Davies, M. & Barriero, B. (1999). *Santorini Volcano. Geological Society of London, Memoirs* **19**, 165 pp.

Druitt, T. H., Costa, F., Deloule, E., Dungan, M. & Scaillet, B. (2012). Decadal to monthly timescales of magma transfer and reservoir growth at a caldera volcano. *Nature* **482**, 77–80.

Fabbro, G., Druitt, T. H. & Scaillet, S. (2013). Evolution of the crustal magma plumbing system during the build-up to the 22-ka caldera-forming eruption of Santorini (Greece). *Bulletin of Volcanology* **75**, 767.

Faure, F. & Schiano, P. (2005). Experimental investigation of equilibration conditions during forsterite growth and melt inclusion formation. *Earth and Planetary Science Letters* **236**, 882–898.

Feuillet, N. (2013). The 2011–2012 unrest at Santorini rift: stress interaction between active faulting and volcanism. *Geophysical Research Letters* **40**, 3532–3537.

Fine, G. & Stolper, E. (1986). Carbon dioxide in basaltic glasses: concentration and speciation. *Earth and Planetary Science Letters* **76**, 263–278.

Foumelis, M., Trasatti, E., Papageorgiou, E., Stramondo, S. & Parcharidis, I. (2013). Monitoring Santorini volcano (Greece) breathing from space. *Geophysical Journal International* **193**, 161–170.

Francalanci, L., Vougioukalakis, G. E., Perini, G. & Manetti, P. (2005). A west–east traverse along the magmatism of the south Aegean volcanic arc in the light of volcanological, chemical and isotope data. In: Fytikas, M. & Vougioukalakis, G. E. (eds) *The South Aegean Active Volcanic Arc: Present Knowledge and Future Perspectives. Developments in Volcanology*. Amsterdam: Elsevier, pp. 65–111.

Gaetani, G. A., O'Leary, J. A., Shimizu, N., Bucholz, C. E. & Newville, M. (2012). Rapid reequilibration of $H_2O$ and oxygen fugacity in olivine-hosted melt inclusions. *Geology* **40**, 915–918.

Gardner, J. E., Thomas, R. M. E., Jaupart, C. & Tait, S. R. (1996). Fragmentation of magma during Plinian volcanic eruptions. *Bulletin of Volcanology* **58**, 144–162.

Gelman, S. E., Gutierrez, F. J. & Bachmann, O. (2013). On the longevity of large upper crustal silicic magma reservoirs. *Geology* **41**, 759–762.

Gertisser, R., Preece, K. & Keller, J. (2009). The Plinian Lower Pumice 2 eruption, Santorini, Greece: magma evolution and volatile behaviour. *Journal of Volcanology and Geothermal Research* **186**, 387–406.

Gudmundsson, A. (2012). Magma chambers: Formation, local stresses, excess pressures, and compartments. *Journal of Volcanology and Geothermal Research* **237–238**, 19–41.

Hartley, M. E., Maclennan, J., Edmonds, M. E. & Thordarson, T. (2014). Reconstructing the deep $CO_2$ degassing behaviour of large basaltic fissure eruptions. *Earth and Planetary Science Letters* **393**, 120–131.

Hauri, E. (2002). SIMS analysis of volatiles in silicate glasses, 2: isotopes and abundances in Hawaiian melt inclusions. *Chemical Geology* **183**, 115–141.

Huijsmans, J. P. P. & Barton, M. (1989). Polybaric geochemical evolution of two shield volcanoes from Santorini, Aegean Sea, Greece: evidence for zoned magma chambers from cyclic compositional variations. *Journal of Petrology* **30**, 583–625.

Huijsmans, J. P. P., Barton, M. & Salters, V. J. M. (1988). Geochemistry and evolution of the calc-alkaline volcanic complex of Santorini, Aegean Sea, Greece. *Journal of Volcanology and Geothermal Research* **34**, 283–306.

Humphreys, M. C. S., Menand, T., Blundy, J. D. & Klimm, K. (2008). Magma ascent rates in explosive eruptions: Constraints from $H_2O$ diffusion in melt inclusions. *Earth and Planetary Science Letters* **270**, 25–40.

Johnson, M. E. & Rutherford, M. J. (1989). Experimental calibration of the aluminum-in-hornblende geobarometer with application to Long Valley caldera (California). *Geology* **17**, 837–841.

Johnston, E. N., Sparks, R. S. J., Phillips, J. C. & Carey, S. (2014). Revised estimates for the volume of the Late Bronze Age Minoan eruption, Santorini, Greece. *Journal of the Geological Society, London* **171**, 583–590.

King, P. L., Vennemann, T. W., Holloway, J. R., Hervig, R. L., Lowenstern, J. B. & Forneris, J. F. (2002). Analytical techniques for volatiles: A case study using intermediate (andesitic) glasses. *American Mineralogist* **87**, 1077–1089.

Konstantinou, K. I. (2010). Crustal rheology of the Santorini–Amorgos zone: Implications for the nucleation depth and rupture extent of the 9 July 1956 Amorgos earthquake, southern Aegean. *Journal of Geodynamics* **50**, 400–409.

Lange, R. A. & Carmichael, I. S. E. (1987). Densities of $Na_2O$–$K_2O$–MgO–MgO–FeO–$Fe_2O_3$–$Al_2O_3$–$TiO_2$–$SiO_2$ liquids: New measurements and derived partial molar properties. *Geochimica et Cosmochimica Acta* **51**, 2931–2946.

Lange, R. A., Frey, H. M. & Hector, J. (2009). A thermodynamic model for the plagioclase–liquid hygrometer/thermometer. *American Mineralogist* **94**, 494–506.

Lesne, P., Scaillet, B. & Pichavant, M. (2014). The solubility of sulfur in hydrous basaltic melts. *Chemical Geology* **418**, 104–116.

Le Voyer, M., Asimow, P. D., Mosenfelder, J. L., Guan, Y., Wallace, P. J., Schiano, P. & Eiler, J. M. (2014). Zonation of $H_2O$ and F concentrations around melt inclusions in olivines. *Journal of Petrology* **55**, 685–707.

Liu, Y., Anderson, A. T., Wilson, C. J. N., Davis, A. M. & Steele, I. M. (2005). Mixing and differentiation in the Oruanui rhyolitic magma, Taupo, New Zealand: evidence from volatiles and trace elements in melt inclusions. *Contributions to Mineralogy and Petrology* **151**, 71–87.

Liu, Y., Anderson, A. T. & Wilson, C. J. N. (2007). Melt pockets in phenocrysts and decompression rates of silicic magmas before fragmentation. *Journal of Geophysical Research* **112**, B06204.

Lloyd, A. S., Plank, T., Ruprecht, P., Hauri, E. H. & Rose, W. (2013). Volatile loss from melt inclusions in pyroclasts of differing sizes. *Contributions to Mineralogy and Petrology* **165**, 129–153.

Lu, F., Anderson, A. T. & Davis, A. M. (1995). Diffusional gradients at the crystal/melt interface and their effect on the composition of melt inclusions. *Journal of Geology* **103**, 591–597.

Mann, A. C. (1983). Trace element geochemistry of high alumina basalt–andesite–dacite–rhyodacite lavas of the Main Volcanic Series of Santorini Volcano, Greece. *Contributions to Mineralogy and Petrology* **395**, 43–57.

Marianelli, P., Métrich, N. & Sbrana, A. (1999). Shallow and deep reservoirs involved in magma supply of the 1944 eruption of Vesuvius. *Bulletin of Volcanology* **61**, 48–63.

Menand, T., Annen, C. & de Saint Blanquat, M. D. (2015). Rates of magma transfer in the crust: Insights into magma reservoir recharge and pluton growth. *Geology* **43**, 1–5.

Métrich, N. & Deloule, E. (2014). Water content, $\delta D$ *and* $\delta^{11}B$ tracking in the Vanuatu arc magmas (Aoba Island): Insights from olivine-hosted melt inclusions. *Lithos* **206–207**, 400–408.

Métrich, N., Berry, A. J., O'Neill, H. S. C. & Susini, J. (2008). The oxidation state of sulfur in synthetic and natural glasses determined by X-ray absorption spectroscopy. *Geochimica et Cosmochimica Acta* **73**, 2382–2399.

Michaud, V., Clocchiatti, R. & Sbrana, S. (2000). The Minoan and post-Minoan eruptions, Santorini (Greece), in the light of melt inclusions: chlorine and sulphur behavior. *Journal of Volcanology and Geothermal Research* **99**, 195–214.

Moore, G. (2008). Interpreting $H_2O$ and $CO_2$ contents in melt inclusions: Constraints from solubility experiments and modelling. In: Putirka, K. D. & Tepley, F. J., III (eds) *Minerals, Inclusions and Volcanic Processes. Mineralogical Society of America and Geochemical Society, Reviews of Mineralogy and Geochemistry* **69**, 333–361.

Moretti, R. & Ottonello, G. (2005). Solubility and speciation of sulfur in silicate melts: The conjugated Toop–Samis–Flood–Grjotheim (CTSFG) model. *Geochimica et Cosmochimica Acta* **69**, 801–823.

Moune, S., Sigmarsson, O., Thordarson, T. & Gauthier, P. J. (2007). Recent volatile evolution in the magmatic system of Hekla volcano, Iceland. *Earth and Planetary Science Letters* **255**, 373–389.

Muir, D. D., Blundy, J. D., Hutchinson, M. C. & Rust, A. C. (2014). Petrological imaging of an active pluton beneath Cerro Uturuncu, Bolivia. *Contributions to Mineralogy and Petrology* **167**, 980.

Neave, D. A., Maclennan, J., Edmonds, M. & Thordarson, T. (2014). Melt mixing causes negative correlation of trace element enrichment and $CO_2$ content prior to an Icelandic eruption. *Earth and Planetary Science Letters* **400**, 272–283.

Newman, A. V., Stiros, S., Feng, L., et al. (2012). Recent geodetic unrest at Santorini Caldera, Greece. *Geophysical Research Letters* **39**(**L06309**).

Newman, S. & Lowenstern, J. B. (2002). VOLATILECALC: a silicate melt–$H_2O$–$CO_2$ solution model written in Visual Basic Excel. *Computers and Geosciences* **28**, 597–604.

Nichols, I. A. (1978). Primary basaltic magmas for the pre-caldera volcanic rocks of Santorini. In: Doumas, C. (ed.) *Thera and the Aegean World II, 1*. London: Thera Foundation, pp. 109–120.

Nomikou, P., Carey, S., Papanikolaou, D., Croff Bell, K., Sakellariou, D., Alexandri, M. & Bejelou, K. (2012). Submarine volcanoes of the Kolumbo volcanic zone NE of Santorini Caldera, Greece. *Global and Planetary Change* **90–91**, 135–151.

Oth, A. (2013). On the characteristics of earthquake stress release variations in Japan. *Earth and Planetary Science Letters* **377–378**, 132–141.

Papale, P. (1999). Modeling of the solubility of a two-component $H_2O + CO_2$ fluid in silicate liquids. *American Mineralogist* **84**, 477–492.

Papale, P., Moretti, R. & Barbato, D. (2006). The compositional dependence of the saturation surface of $H_2O + CO_2$ fluids in silicate melts. *Chemical Geology* **229**, 78–95.

Papoutsis, I., Papanikolaou, X., Floyd, M., Ji, K. H., Kontoes, C., Paradissis, D. & Zacharis, V. (2012). Mapping inflation at Santorini volcano, Greece, using GPS and InSAR. *Geophysical Research Letters* **40**, 267–272.

Parks, M. M., Biggs, J., England, P., et al. (2012). Evolution of Santorini Volcano dominated by episodic and rapid fluxes of melt from depth. *Nature Geoscience* **5**, 749–754.

Parks, M. M., Moore, J. D. P., Papanikolaou, X., Biggs, J., Mather, T. A., Pyle, D. M., Raptakis, C., Paradissis, D., Hooper, A., Parsons, B. & Nomikou, P. (2015). From quiescence to unrest: 20 years of satellite geodetic measurements at Santorini volcano, Greece. *Journal of Geophysical Research* **120**, 1309–1328.

Pinel, V. & Jaupart, C. (2003). Magma chamber behavior beneath a volcanic edifice. *Journal of Geophysical Research* **108**, 1–17.

Pioli, L., Erlund, E., Johnson, E., Cashman, K., Wallace, P., Rosi, M. & Delgado Granados, H. (2008). Explosive dynamics of violent Strombolian eruptions: The eruption of Parícutin

Volcano 1943–1952 (Mexico). *Earth and Planetary Science Letters* **271**, 359–368.

Plank, T., Kelley, K. A., Zimmer, M. M., Hauri, E. H. & Wallace, P. J. (2013). Why do mafic arc magmas contain ~4 wt % water on average? *Earth and Planetary Science Letters* **364**, 168–179.

Putirka, K. D. (2008). Thermometers and barometers for volcanic systems. In: Putirka, K. D. & Tepley, F. J. III (eds) *Minerals, Inclusions and Volcanic Processes. Mineralogical Society of America and Geochemical Society, Reviews of Mineralogy and Geochemistry* **69**, 61–120.

Pyle, D. M. (1990). New estimates for the volume of the Minoan eruption. In: Hardy, D. A. (ed.) *Thera and the Aegean World III*, **vol 2**. Thera Foundation, London, pp 113–121.

Pyle, D. M. & Elliott, J. R. (2006). Quantitative morphology, recent evolution, and future activity of the Kameni Islands volcano, Santorini, Greece. *Geosphere* **2**, 253–268.

Rizzo, A. L., Barberi, F., Carapezza, M. L., Di Piazza, A., Francalanci, L., Sortino, F. & D'Alessandro, W. (2015). New mafic magma refilling a quiescent volcano: Evidence from He–Ne–Ar isotopes during the 2011–2012 unrest at Santorini, Greece. *Geochemistry,* Geophysics*, Geosystems* **16**, 798–814.

Rust, A. C. & Cashman, K. V. (2011). Permeability controls on expansion and size distributions of pyroclasts. *Journal of Geophysical Research* **116**, B11202.

Sachpazi, M., Hirn, A., Nercessian, A., Avedik, F., McBride, J., Loucoyannakis, M. & Nicolich, R. (1997). A first coincident normal-incidence and wide-angle approach to studying the extending Aegean crust. *Tectonophysics* **270**, 301–312.

Scaillet, B. & Evans, B. W. (1999). The 15 June 1991 eruption of Mount Pinatubo. I. Phase equilibria and pre-eruption P–T–fO2–fH2O conditions of the dacite magma. *Journal of Petrology* **40**, 381–411.

Scaillet, B. & Pichavant, M. (2005). A model of sulphur solubility for hydrous mafic melts: application to the determination of magmatic fluid compositions of Italian volcanoes. *Annals of Geophysics* **48**, 671–698.

Scaillet, B., Luhr, J. F. & Carroll, M. C. (2003). Petrological and volcanological constraints on volcanic sulfur emissions to the atmosphere. In: Robock, A. & Oppenheimer, C. (eds) *Volcanism and the Earth's Atmosphere. Geophysical Monograph, American Geophysical Union* **139**, 11–40.

Shaw, A. M., Hauri, E. H., Fischer, T. P., Hilton, D. R. & Kelley, K. A. (2008). Hydrogen isotopes in Mariana arc melt inclusions: Implications for subduction dehydration and the deep-Earth water cycle. *Earth and Planetary Science Letters* **275**, 138–145.

Sigurdsson, H., Carey, S. & Devine, J. D. (1990). Assessment of the mass, dynamics and the environmental effects of the Minoan eruption of Santorini Volcano. In: Hardy, D. A. (ed.) *Thera and the Aegean World III, 2*. London: Thera Foundation, pp. 100–112.

Smith, D. J. (2014). Clinopyroxene precursors to amphibole sponge in arc crust. *Nature Communications* **5**, 1–6.

Solano, J. M. S., Jackson, M. D., Sparks, R. S. J., Blundy, J. D. & Annen, C. (2012). Melt segregation in deep crustal hot zones: a mechanism for chemical differentiation, crustal assimilation and the formation of evolved magmas. *Journal of Petrology* **53**, 1999–2026.

Stelling, J., Botcharnikov, R. E., Beermann, O. & Nowak, M. (2008). Solubility of $H_2O$- and chlorine-bearing fluids in basaltic melt of Mount Etna at $T = 1050$–$1250^{\circ}C$ and $P = 200$ MPa. *Chemical Geology* **256**, 102–110.

Thomas, R. & Sparks R. S. J. (1992). Cooling of tephra during fallout from eruption columns. *Bulletin of Volcanology* **54**, 542–553.

Tirel, C., Gueydan, F., Tiberi, C. & Brun, J.-P. (2004). Aegean crustal thickness inferred from gravity inversion. Geodynamical implications. *Earth and Planetary Science Letters* **228**, 267–280.

Toplis, M. J. (2005). The thermodynamics of iron and magnesium partitioning between olivine and liquid: criteria for assessing and predicting equilibrium in natural and experimental systems. *Contributions to Mineralogy and Petrology* **149**, 22–39.

Vaggelli, M., Pellegrini, M., Vougioukalakis, G., Innocenti, S. & Francalanci, I. (2009). Highly Sr radiogenic tholeiitic magmas in the latest inter-Plinian activity of Santorini volcano, Greece. *Journal of Geophyical Research* **114**, 1–21.

Vespa, M., Keller, J. & Gertisser, R. (2006). Inter-Plinian explosive activity of Santorini volcano (Greece) during the past 150,000 years. *Journal of Volcanology and Geothermal Research* **153**, 262–286.

Villemant, B., Mouatt, J. & Michel, A. (2008). Andesitic magma degassing investigated through $H_2O$ vapour–melt partitioning of halogens at Soufrière Hills Volcano, Montserrat (Lesser Antilles). *Earth and Planetary Science Letters* **269**, 212–229.

Wallace, P. J. (2005). Volatiles in subduction zone magmas: concentrations and fluxes based on melt inclusion and volcanic gas data. *Journal of Volcanology and Geothermal Research* **140**, 217–240.

Wallace, P. J., Anderson, A. T. & Davis, A. M. (1995). Quantification of pre-eruptive exsolved gas contents in silicic magmas. *Nature* **377**, 612–616.

Webster, J. D. (1990). Partitioning of F between $H_2O$ and $CO_2$ fluids and topaz rhyolite melt; Implications for mineralizing magmatic–hydrothermal fluids in F-rich granitic systems. *Contributions to Mineralogy and Petrology* **104**, 424–438.

Webster, J. D. (2004). The exsolution of magmatic hydrosaline chloride liquids. *Chemical Geology* **210**, 33–48.

Webster, J. D., Kinzler, R. J. & Mathez, E. A. (1999). Chloride and water solubility in basalt and andesite melts and implications for magmatic degassing. *Geochimica et Cosmochimica Acta* **63**, 729–738.

Witham, F., Blundy, J., Kohn, S. C., Lesne, P., Dixon, J., Churakov, S. V. & Botcharnikov, R. (2012). SolEx: A model for mixed COHSCl–volatile solubilities and exsolved gas compositions in basalt. *Computers and Geosciences* **45**, 87–97.

Wright, H. M., Bacon, C. R., Vazquez, J. A. & Sisson, T. W. (2012). Sixty thousand years of magmatic volatile history before the caldera-forming eruption of Mount Mazama, Crater Lake, Oregon. *Contributions to Mineralogy and Petrology* **164**, 1027–1052.

Zellmer, G., Turner, S. & Hawkesworth, C. (2000). Timescales of destructive plate margin magmatism: new insights from Santorini, Aegean volcanic arc. *Earth and Planetary Science Letters* **174**, 265–281.

## APPENDIX A: $H_2O$ AND $CO_2$ GLASS STANDARDS USED IN SIMS ANALYSIS

| Basaltic standard | $H_2O$ (wt %) | $CO_2$ (ppm) | Andesitic standard | $CO_2$ (ppm) | Dacitic standard | $H_2O$ (wt %) | Rhyolitic standard | $H_2O$ (wt %) | $CO_2$ (ppm) |
|---|---|---|---|---|---|---|---|---|---|
| M34 | 5·70 ± 0·13 | 375 ± 30 | MP18.1 | 2618 ± 302 | Dac 0 | 0 | Rhy 0 | 0 | |
| M35 | 4·20 ± 0·12 | 1019 ± 81 | MP20.1 | 2639 ± 106 | Dac 212 | 2·12 | Rhy 242 | 2·42 | |
| M40 | 3·07 ± 0·12 | 2183 ± 178 | MP20.3 | 4288 ± 58 | Dac 445 | 4·45 | Rhy 424 | 4·24 | |
| M43 | 2·62 ± 0·11 | 3172 ± 265 | MP23.2 | 3639 ± 226 | Dac 636 | 6·36 | Rhy 638 | 6·38 | |
| M48 | 0·77 ± 0·11 | 176 ± 15 | MP23.3 | 4225 ± 120 | | | BT2 628-5 | 6·57 ± 0·18 | 14 ± 3 |
| M49 | 1·25 ± 0·10 | 140 | MP24.1 | 3948 ± 182 | | | BT2 628-6 | 5·69 ± 0·06 | 411 ± 22 |
| M50 | 2·43 ± 0·10 | 35 | | | | | BT2 628-7 | 4·98 ± 0·11 | 676 ± 44 |
| M66 | 0·66 ± 0·10 | 3856 | | | | | | | |
| M1 roman | 3·50 ± 0·10 | | | | | | | | |
| M2 roman | 4·93 ± 0·10 | | | | | | | | |
| M3 roman | 4·77 ± 0·10 | | | | | | | | |
| M5 roman | 5·05 ± 0·10 | | | | | | | | |
| N72 | 0 | 0 | | | | | | | |

M34, M35, M40, M43, M48–M50, M66, M1, M2, M3, M5 and N72 are international basaltic glass standards. MP 18.1, 20.1, 20.3, 23.2, 23.3 and 24.1 are doped andesitic glasses fabricated by the authors at Clermont-Ferrand (see Appendix B). Dac 0, 212, 445 and 636 are doped dacitic glasses fabricated from Pinatubo pumice; $H_2O$ determined by Karl Fischer titration (Scaillet & Evans, 1999). Rhy 0, 242, 424 and 638 are doped rhyolitic glasses fabricated from Pinatubo pumice; $H_2O$ determined by Karl Fischer titration (Scaillet & Evans, 1999). BT2 628-5, 628-6 and 628-7 are doped rhyolitic glasses fabricated from Bishop Tuff pumice; $H_2O$ and $CO_2$ determined by Fourier transform infrared spectrometry (Cadoux *et al.*, 2014).

## APPENDIX B: PREPARATION OF THE ANDESITIC STANDARDS 'MP' FOR $CO_2$

The andesitic $CO_2$ standards 'MP' (Table B1) were synthesized for this study using pumice from the Middle Pumice eruption. Clasts were crushed, and the powder was heated in a vertical furnace at 1400°C in air for 2 h in a Pt crucible. The resulting dark glass was then crushed to a fine powder, which was mixed with appropriate proportions of $CaCO_3$ powder; 50 mg of the mixture was then arc-welded into 4 mm diameter $Au_{80}Pd_{20}$ capsules. Each capsule was submerged in acetone for at least 15 min, and was weighed before and after to check for possible leaks.

The syntheses were performed in a 3/4 inch piston-cylinder apparatus at the Laboratoire Magmas et Volcans (Clermont-Ferrand). The piston-cylinder furnace comprised two Pyrex tubes (inside and outside the graphite furnace), MgO spacers, and a graphite furnace. To reduce H and C diffusion inside the capsule, finely powdered $Fe_2O_3$ was packed between the capsule and the internal Pyrex tube. Temperatures were measured using $W_5Re_{95}$ thermocouples and controlled to ±2°C. All experiments were carried out at 1·0 GPa, 1300°C and $CO_2$-undersaturated conditions to ensure the production of bubble-free glasses. For each experiment, the assembly was first pressurized to 300 MPa, then heated to 650°C, and left at 650°C for several minutes, before ramping simultaneously to the final pressure–temperature conditions. Each experiment lasted 3 h, and the samples were quenched approximately isobarically to below the glass transition temperature in about 8 s. The absence of crystals, bubbles or oxides in the resulting glasses was checked optically and on BSE images; chemical homogeneity of the glasses was checked by electron microprobe analysis (Table B1).

**Table B1:** Composition of MP glass standards

| | Mean ($n = 60$) | 1σ |
|---|---|---|
| $SiO_2$ | 62·83 | 0·34 |
| $TiO_2$ | 0·99 | 0·06 |
| $Al_2O_3$ | 15·91 | 0·22 |
| FeO | 5·80 | 0·18 |
| MnO | 0·17 | 0·03 |
| MgO | 1·97 | 0·08 |
| CaO | 4·53 | 0·20 |
| $Na_2O$ | 4·29 | 0·16 |
| $K_2O$ | 2·27 | 0·11 |
| $P_2O_5$ | 0·25 | 0·10 |
| Total | 99·02 | 0·47 |

The $CO_2$ concentrations of experimental glasses were measured by micro-Fourier transform infrared spectrometry at the Laboratoire Magmas et Volcans in Clermont-Ferrand. Spectra were collected using a Vertex 70 Bruker spectrometer with a KBr beam splitter, MCT-A detector coupled to a Hyperion microscope equipped with 15 × objective and condenser. Spectra were measured through a $CaF_2$ plate. They were integrated between 700 and 7500 $cm^{-1}$ with a resolution of 4 $cm^{-1}$ and up to 300 scans. The entire system was continuously purged with dry air.

Glass fragments were doubly polished to a 0·25 μm corundum disk finish with thicknesses ranging from 80 to 150 μm. The samples were cleaned in acetone and ethanol, and no residues on sample surfaces were observed. A 100 μm diameter area was examined using a microscope to avoid any bubbles and surface imperfections. Dissolved $CO_2$ was measured from the intensities of the absorption bands at 1515 and 2350 $cm^{-1}$. These bands correspond respectively to antisymmetric

stretching vibration of distorted carbonate groups and molecular $CO_2$ (e.g. Fine & Stolper, 1986; Dixon *et al.*, 1995). The concentrations of total $CO_2$ were obtained by adding the concentrations of each carbon species. These were determined, for each band, using the Beer–Lambert law (e.g. Fine & Stolper, 1986). For baseline corrections, we subtracted the spectrum of a $CO_2$-free sample of the same glass. Sample thicknesses were measured using a micrometer and compared with measurements obtained by optical microscope in reflected light mode. Densities of the glasses were calculated using the model of Lange & Carmichael (1987). The molar absorptivity coefficient for the 1515 $cm^{-1}$ band, which depends strongly on glass composition, was estimated as 261 l $mol^{-1}$ $cm^{-1}$ using the Na/(Na + Ca) value following Dixon & Pan (1995). This method is more applicable to basaltic compositions, but the obtained value is in agreement with that used by King *et al.* (2002) for andesitic compositions. For the 2350 $cm^{-1}$ band, we used a coefficient value of 945 l $mol^{-1}$ $cm^{-1}$ determined for Na–Al–Si–O glasses (Fine & Stolper, 1986) and used for andesitic compositions (King *et al.*, 2002).